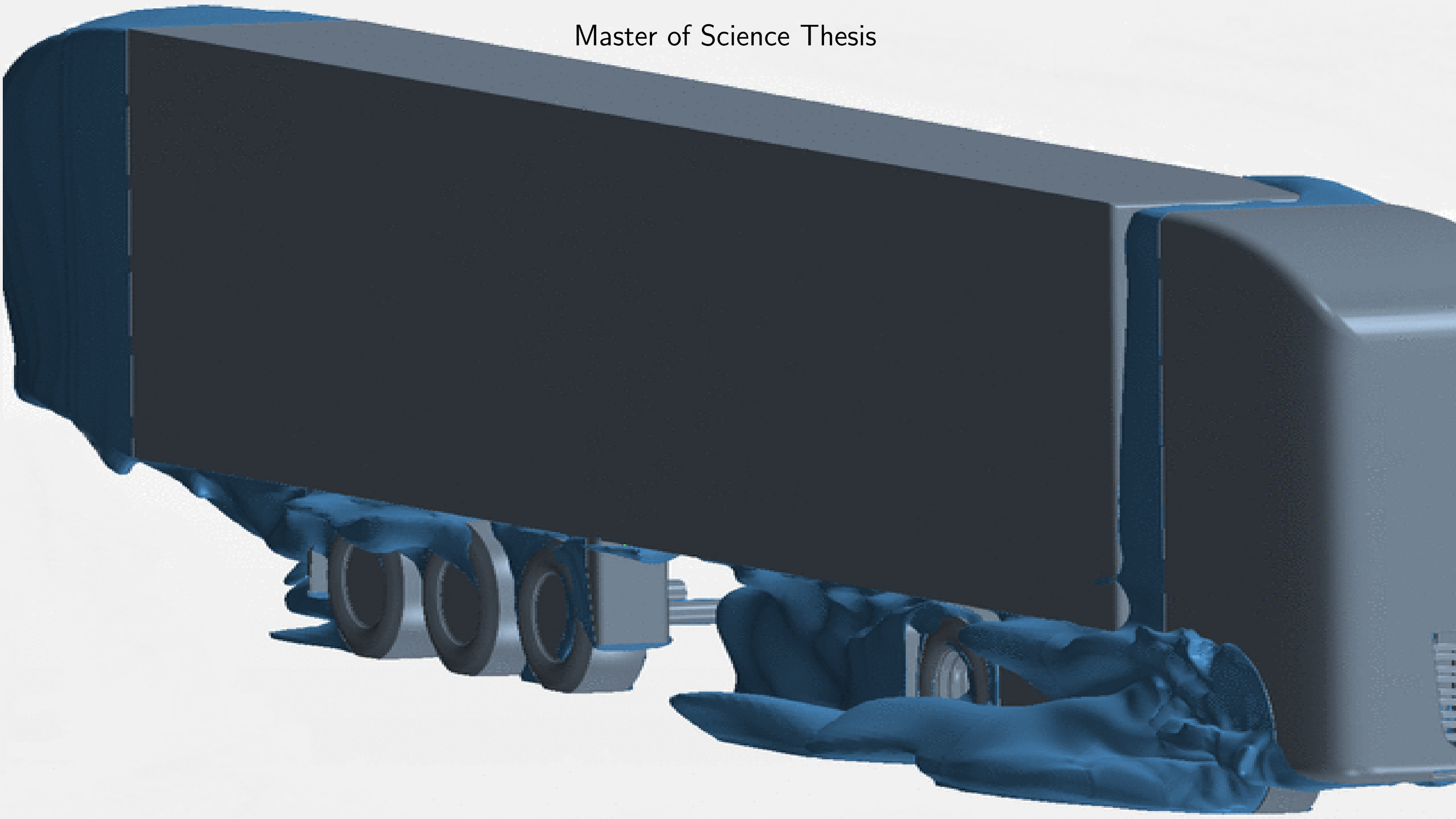

Master of Science Thesis

Truck wheelhouse aerodynamics

Numerical investigations into the phenomena in heavy truck wheelhouses

TS Scheeve

November 19, 2013

Faculty of Aerospace Engineering

Delft University of Technology

Truck wheelhouse aerodynamics

Numerical investigations into the phenomena in heavy truck wheelhouses

Master of Science Thesis

For obtaining the degree of Master of Science in Aerospace Engineering
at Delft University of Technology

TS Scheeve

November 19, 2013

Faculty of Aerospace Engineering · Delft University of Technology

Delft University of Technology

Copyright © Aerospace Engineering, Delft University of Technology
All rights reserved.

DELFT UNIVERSITY OF TECHNOLOGY
DEPARTMENT OF AERODYNAMICS

The undersigned hereby certify that they have read and recommend to the Faculty of Aerospace Engineering for acceptance the thesis entitled **"Truck wheelhouse aerodynamics"** by **TS Scheeve** in fulfillment of the requirements for the degree of **Master of Science**.

Dated: November 19, 2013

Chairman:

Prof. Dr. ir. L.L.M. Veldhuis

Supervisors:

Dr. D. Rentema (DAF Trucks N.V.)

Dr. S.J. Hulshoff

Reader:

Dr. ir. A.H. van Zuijlen

Acknowledgments

I would like to thank family, friends and colleagues at DAF Trucks N.V. and Delft University of Technology for their support and encouragement.

Special thanks goes out to DAF Trucks N.V. for making this thesis possible and the Technical Analysis department for being a good workplace. Colleagues in other departments are thanked as well, especially the fellow interns, you were very kind. In particular thanks to Date Rentema and Theo Volkers from DAF Trucks, for their discussions and involvement on the aerodynamic side of this thesis. Furthermore, a particular thanks to Date Rentema for his support, comments and guidance throughout the thesis.

For his knowledge, guidance and advice on the thesis a thanks to Dr. Steven Hulshoff. His comments on the thesis were of great help to me.

Final thanks goes to Dr. Michael Deschamps from CD-adapco for his help and support with the STAR-CCM+ software.

Summary

The continuous increase in fuel prices and stricter regulations on emissions have pushed the attention of truck designers into new areas to provide more fuel efficient solutions. The flow in the front wheelhouse is a relatively unexplored area, compared to studies on the shapes of the cabin, roof and trailer. However, it is known that the underhood is responsible for almost half of the total aerodynamic drag, with the front wheelhouse being one of the contributors. As a step towards improving the flow in the underhood, this thesis, performed at DAF Trucks N.V., focussed on the identification of aerodynamic phenomena in the front wheelhouses of heavy trucks using CFD simulations.

To validate model settings, a study on a simplified wheelhouse model with available experimental data was performed. It was found that steady state RANS simulations were able to predict the mean behaviour of the flow and drag coefficient reasonably well. Furthermore, the structure of the flow and position of vortex cores agreed with the observations in the literature. A mesh sensitivity study resulted in reliable mesh settings that served as guidelines for the baseline truck model.

The results of the baseline truck model showed flow structures with a large influence on the width of the wheel wake. The flow in the underhood was under a large yaw angle, which induced a large separation region on the front wheel. Observations of the massflow distribution showed that almost 30% of the flow that entered the underhood left through the front wheelhouse. Furthermore, only 35% of the flow through the underhood reached the rear tyres of the tractor. The dominating phenomena were in agreement with observations on the simplified models.

The computations of the variants demonstrated that the structure of the flow was sensitive to local changes in geometry. These changes could result in significant changed flow conditions downstream, most noticeably on the trailer wheels. This influenced the drag of the total vehicle significantly. It was found that an increased total pressure in the wheel wake resulted in an increased drag on the trailer wheels. Furthermore, minimizing the total pressure in the front wheelhouse was found to decrease drag locally. The opposite for both these observations was also valid.

The analysis of the flow fields resulted in an understanding of the flow in the wheelhouse and its sensitivity to changes in geometry. With more extensive simulations it might be possible to change the conditions in the wheelhouse, reducing total drag.

Table of Contents

Acknowledgments **v**

Summary **vii**

List of Figures **xiii**

List of Tables **xix**

Nomenclature **xxi**

1 Introduction **1**

1.1 Model assumptions 2

2 Literature overview **3**

2.1 Isolated wheels 3

2.1.1 Overview of previous studies 4

2.1.2 Physics 6

2.1.3 Vortex structures 7

2.1.4 Wake structure 9

2.1.5 Non-idealized tyre models 10

2.2 Shrouded wheels 12

2.2.1 Overview of previous studies 13

2.2.2 Physics 16
2.2.3 Parametric Studies 18
2.3 Summary and Conclusions 19
2.3.1 Summary 20
2.3.2 Conclusions 21

3 Validation 23

3.1 Model description 23
3.2 Mesh settings 24
3.2.1 Types of meshes 25
3.2.2 Wall modelling 25
3.2.3 Mesh refinements 26
3.3 Mesh sensitivity study 27
3.3.1 Approach 28
3.3.2 Results 28
3.3.3 Mesh restructuring 30
3.3.4 Summary of mesh settings 31
3.4 Turbulence models 31
3.4.1 Description of turbulence models 31
3.4.2 Results 32
3.4.3 Trade off 39
3.5 Transient solvers 40
3.6 Summary 42

4 Baseline truck model 43

4.1 Geometry 43
4.2 Mesh settings 45
4.3 Model settings 47

4.4 Modifications 48

5 Results 51

5.1 Statistical analysis 51

5.2 Baseline truck model results 53

5.2.1 Flow fields 53

5.2.2 Comparison with validation model 55

5.2.3 Effects of geometry on wake formation 57

5.3 Results of the modifications 58

5.4 Analysis of modifications 59

5.4.1 Drag buildup 60

5.4.2 Massflow distribution 63

5.4.3 Closed wheelhouse, rotating wheels 64

5.4.4 Wheelhouse side cover 66

5.4.5 Underhood cap 68

5.4.6 Wheel spoiler, 45° angle 69

5.4.7 Clearance gap 71

5.5 Comparison with literature 73

5.5.1 Wheel spoilers 73

5.5.2 Underhood cap 74

5.5.3 Wheelhouse venting 75

5.6 Summary 77

6 Conclusions 79

7 Recommendations 81

Bibliography 83

A Results of massflow monitors 87

B Supplemantary figures **89**

List of Figures

2.1 Pressure coefficient distribution in centreplane of an isolated tyre (Fackrell, 1974) 6

2.2 Sign convention isolated wheel, introduced by (Fackrell, 1974) 6

2.3 Sketch of dominant vortex structures behind a stationary wheel (Wäschle, 2007) 8

2.4 Sketch of dominant vortex structures behind a rotating wheel (Wäschle, 2007) . 8

2.5 Wake structure of isolated and rotating wheel at different locations in the wake (Wäschle et al., 2004) 10

2.6 Change in velocity magnitude as a result of adding grooves to an isolated rotating wheel (Axerio-Cilies, 2012) 11

2.7 Common F1 front wheel assembly and suggested flow pattern through the hub (Sprot et al., 2011) 12

2.8 Geometry of the tyre profile under high and low deformations (Sprot et al., 2012) 12

2.9 Close-up of the tyre profile under high and low deformations (Sprot et al., 2012) 12

2.10 Flow field visualization obtained with tufts and hot wire (Oswald and Browne, 1981) 13

2.11 Wheelhouse models used in the studies of 2.11(a) (Axon, 1999), 2.11(b) (Skea et al., 2000), 2.11(c) (Régert and Lajos, 2007) and 2.11(d) (Krajnović et al., 2011). Although models 2.11(b)-2.11(d) are all derived from (Fabijanic, 1996), the geometry was altered to the experimentalists' needs 14

2.12 Vortex cores and time-averaged streamlines (Krajnović et al., 2011). The freestream flow direction in (a) is from left to right, (b) from right to left 16

2.13 Vortex skeleton of flow in a wheelhouse (Régert and Lajos, 2007) 17

2.14 Pressure coefficient distribution of a wheel in a wheelhouse (Axon, 1999) 18

2.15 Illustration of chamfer fill in a wheelhouse (Mavuri and Watkins, 2011) 19

3.1 CAD drawings of model used in validation study (Axon, 1999) 24

3.2 Behaviour of the boundary layer in the vicinity of the wall (White, 2006) 25

3.3 Difference in prism layer, in the centreline of the wheel, between $y^+ = 30$ (Figure 3.3(a)) and $y^+ = 1$ (Figure 3.3(b)). 26

3.4 Positioning of refinement volumes 27

3.5 Close up of refinement volumes surrounding the contact patch of the wheel . . . 27

3.6 Drag coefficient per iteration, for mesh M_8 29

3.7 Drag coefficient as a result of mesh refinement 29

3.8 Behaviour of the flow as a result of mesh refinement 29

3.9 Refinement volumes near the contact patch of the validation model 30

3.10 Refinement volumes near the contact patch of the restructured mesh 30

3.11 Positioning of baseline refinement volumes in the wake 30

3.12 Positioning of the restructured refinement volumes in the wake 30

3.13 Drag coefficients for difference turbulence model settings, compared to experimental data (Axon, 1999) 33

3.14 Experimental pressure coefficient distribution on the inner surface of the wheelhouse (Axon, 1999) 34

3.15 Computed pressure coefficient distribution on the inner surface of the wheelhouse, $k - \omega$ SST_{30}, mesh OPT. Note, black lines correspond to the boundaries seen in Figure 3.14 35

3.16 Measurement planes of the pressure coefficient distribution in the centreline of the wheel 35

3.17 Illustration of flow separation on front wheel and stagnating on the top surface of the wheelhouse 35

3.18 Pressure coefficient distribution on front surface of wheelhouse 36

3.19 Pressure coefficient distribution on top surface of wheelhouse 37

3.20 Pressure coefficient distribution on back surface of wheelhouse 38

3.21 Sketch of position of most dominant vortices (Régert and Lajos, 2007) 38

3.22 Isosurfaces of QD$/U_\infty = $ 50000, SST_{30} OPT 39

3.23 Isosurfaces of $p_{tot} = 0$, SST_{30} OPT 39

3.24 Comparison of drag coefficient of steady and unsteady simulations 41

4.1 Baseline truck model geometry, with x- and z-axis plotted 44
4.2 Bulge radius 44
4.3 Mesh near the contact patch 44
4.4 Distribution of refinement volumes on baseline truck model 46
4.5 View of mesh around the baseline truck model 46
4.6 Close up view of mesh around the baseline truck model 46
4.7 Boundary conditions of the walls surrounding the truck model 47
4.8 Overview of modifications 49

5.1 Drag coefficient of baseline model 52
5.2 Autocorrelation function of the baseline truck model 52
5.3 Close-up of the first valley of the autocorrelation of the baseline model 52
5.4 Location of planes used in the analysis of the flow fields 53
5.5 Baseline: velocity magnitude, Z/D = 0.2 54
5.6 Baseline: velocity magnitude, Z/D = 0.5 54
5.7 Baseline: total pressure coefficient, Z/D = 0.2 54
5.8 Baseline: total pressure coefficient, Z/D = 0.5 54
5.9 Baseline: total pressure coefficient, Z/D = 0.8 54
5.10 Truck baseline: velocity vectors, plotted on $C_{p,t}$ field, centreline of the wheel . . 55
5.11 Validation model: velocity vectors, plotted on $C_{p,t}$ field, centreline of the wheel . 55
5.12 Truck baseline: velocity vectors, plotted on $C_{p,t}$ field, Z/D = 0 56
5.13 Validation model: velocity vectors, plotted on $C_{p,t}$ field, Z/D = 0 56
5.14 Baseline model: distribution of $C_{p,t}$ near the mudguard, plotted with velocity magnitude vectors in normal plane 56
5.15 Validation model: distribution of $C_{p,t}$ behind the wheel, plotted with velocity magnitude vectors in normal plane 56

5.16 Baseline model: isosurfaces of $p_{tot} = 0$ . . . 57

5.17 Baseline model: isosurfaces of QD/U_∞ = 50000 . . . 57

5.18 Baseline model, distribution of $C_{p,t}$, Z/D = 0.5 for two different iterations . . . 58

5.19 Drag coefficients of modifications, compared to baseline . . . 59

5.20 Buildup of drag of the truck model (pressure drag only) . . . 60

5.21 Difference in drag buildup, compared to baseline . . . 61

5.22 Difference in drag buildup, close-up of wheel region, compared to baseline . . . 62

5.23 Drag buildup of wheel, enclosed by the wheelhouse . . . 62

5.24 Location of planes in underhood that measure massflow in x-direction . . . 63

5.25 Location of planes in wheelhouse that measure massflow in y-direction . . . 63

5.26 Distribution of massflow through the underhood . . . 64

5.27 Difference in massflow distribution, compared to the baseline . . . 64

5.28 $C_{p,t,wcr}$ - $C_{p,t,b}$, Z/D = .2 . . . 65

5.29 $V_{mag,wcr}$ - $V_{mag,b}$, Z/D = .2 . . . 65

5.30 $C_{p,t,wcr}$ - $C_{p,t,b}$, Z/D = .5 . . . 65

5.31 $V_{mag,wcr}$ - $V_{mag,b}$, Z/D = .5 . . . 65

5.32 $C_{p,t,wcr}$ - $C_{p,t,b}$, Z/D = .5 . . . 66

5.33 Wheelhouse closed rotating: isosurfaces of $p_{tot} = 0$ . . . 66

5.34 $C_{p,t,scw}$ - $C_{p,t,b}$, Z/D = .2 . . . 67

5.35 $C_{p,t,scw}$ - $C_{p,t,b}$, Z/D = .5 . . . 67

5.36 $C_{p,t,scw}$ - $C_{p,t,b}$, Z/D = .5 . . . 67

5.37 Side cover: isosurfaces of $p_{tot} = 0$ . . . 68

5.38 $C_{p,t,uhc}$ - $C_{p,t,b}$, Z/D = .2 . . . 68

5.39 $C_{p,t,uhc}$ - $C_{p,t,b}$, Z/D = .5 . . . 68

5.40 $C_{p,t,uhc}$ - $C_{p,t,b}$, Z/D = .5 . . . 69

5.41 Underhood cap: isosurfaces of $p_{tot} = 0$ 69

5.42 $C_{p,t,w45}$ - $C_{p,t,b}$, Z/D = .2 70

5.43 $C_{p,t,w45}$ - $C_{p,t,b}$, Z/D = .5 70

5.44 $C_{p,t,w45}$ - $C_{p,t,b}$, Z/D = .5 70

5.45 $45°$ spoiler: isosurfaces of $p_{tot} = 0$ 71

5.46 $C_{p,t,6cm}$ - $C_{p,t,b}$, Z/D = .2 71

5.47 $C_{p,t,6cm}$ - $C_{p,t,b}$, Z/D = .5 71

5.48 $C_{p,t,6cm}$ - $C_{p,t,b}$, Z/D = .85 72

5.49 Clearance gap: isosurfaces of $p_{tot} = 0$ 72

5.50 Wheel spoiler in front of wheel (Dimitriou and Klussmann, 2006) 73

5.51 Normalised velocity magnitude for the underhood cap variant, from (Söderblom et al., 2009) 74

5.52 Normalised velocity magnitude for the underhood cap variant, simulation result . 74

5.53 Normalised velocity magnitude for the wheelhouse ventilation variant, from (Söderblom et al., 2009) 75

5.54 Normalised velocity magnitude for the wheelhouse ventilation variant, simulation result 75

5.55 Wheelhouse ventilation: isosurfaces of $p_{tot} = 0$ 76

B.1 Isosurface of QD/U_∞ = 50000, $k - \omega$ SST_1 turbulence model 89

B.2 Isosurface of $p_{tot} = 0$, $k - \omega$ SST_1 turbulence model 89

B.3 Isosurface of QD/U_∞ = 50000, $k - \omega$ SST_1 turbulence model, restructured . . . 90

B.4 Isosurface of $p_{tot} = 0$, $k - \omega$ SST_1 turbulence model, restructured 90

B.5 Isosurface of QD/U_∞ = 50000, $k - \omega$ SST_{30} turbulence model 90

B.6 Isosurface of $p_{tot} = 0$, $k - \omega$ SST_{30} turbulence model 90

B.7 Isosurface of QD/U_∞ = 50000, $k - \omega$ turbulence model 90

B.8 Isosurface of $p_{tot} = 0$, $k - \omega$ turbulence model 90

B.9 Isosurface of QD/U_∞ = 50000, $k - \omega$ turbulence model, restructured 91

B.10 Isosurface of $p_{tot} = 0$, $k - \omega$ turbulence model, restructured 91

B.11 Isosurface of QD/U_∞ = 50000, $k - \epsilon$ turbulence model 91

B.12 Isosurface of $p_{tot} = 0$, $k - \epsilon$ turbulence model 91

B.13 Isosurface of QD/U_∞ = 50000, $k - \epsilon$ turbulence model, restructured 91

B.14 Isosurface of $p_{tot} = 0$, $k - \epsilon$ turbulence model, restructured 91

B.15 Pressure coefficient distribution, $k - \omega$, mesh M8 92

B.16 Pressure coefficient distribution, $k - \omega$, mesh OPT 92

B.17 Pressure coefficient distribution, $k - \omega$, mesh M8 92

B.18 Pressure coefficient distribution, $k - \epsilon$, mesh OPT 93

B.19 Pressure coefficient distribution, $k - \omega$ SST_30, mesh M8 93

B.20 Pressure coefficient distribution, $k - \omega$ SST_1, mesh OPT 93

B.21 Pressure coefficient distribution, $k - \omega$ SST_1, mesh M8 94

B.22 $V_{mag,scw}$ - $V_{mag,b}$, Z/D = .2 95

B.23 $V_{mag,scw}$ - $V_{mag,b}$, Z/D = .5 95

B.24 $V_{mag,ts}$ - $V_{mag,b}$, Z/D = .2 95

B.25 $V_{mag,ts}$ - $V_{mag,b}$, Z/D = .5 95

B.26 $V_{mag,w45}$ - $V_{mag,b}$, Z/D = .2 95

B.27 $V_{mag,w45}$ - $V_{mag,b}$, Z/D = .5 95

B.28 $V_{mag,6cm}$ - $V_{mag,b}$, Z/D = .2 96

B.29 $V_{mag,6cm}$ - $V_{mag,b}$, Z/D = .5 96

List of Tables

2.1 Overview of research into isolated wheels 20

2.2 Overview of research into shrouded wheels 20

3.1 Overview of refinement volumes 27

3.2 Overview of simulations performed to investigate the turbulence settings 32

3.3 Turbulence model trade off table 40

4.1 Overview of refinement volumes 45

5.1 Drag coefficient of modifications 59

5.2 Definition of the indices in Figure 5.26 and 5.27 63

5.3 Massflow through underhood, as percentage of massflow at the beginning of the underhood 64

A.1 Massflows (%) through the massflow planes defined in Figures 5.24 and 5.25 . . 88

A.2 Massflows (kg/s) through the massflow planes defined in Figures 5.24 and 5.25 . 88

Nomenclature

θ	Angular position on the surface of the wheel	deg
C_D	Drag Coefficient	-
C_L	Lift Coefficient	-
C_p	Pressure Coefficient	-
$C_{p,tot}$	Total Pressure Coefficient	-
D	(Wheel) Diameter	m
R	(Wheel) Radius	m
u^+	Dimensionless velocity	-
U_∞	Freestream velocity	ms^{-1}
y^+	Dimensionless wall distance	-
Q	Q-criterion for vortex identification (Jeong and Hussain, 1995)	-
QD/U_∞	Dimensionless Q	-
X/R	Dimensionless horizontal distance	-
Z/D	Dimensionless vertical distance	-
MRF	Multiple Reference Frame	
OPT	Restructured mesh	
SST_1	$k-\omega$ SST turbulence model, $y^+ \approx 1$	
SST_{30}	$k-\omega$ SST turbulence model, $y^+ > 30$	

Chapter 1

Introduction

Increasing fuel prices and emission regulations, amongst which CO_2, fuel the need for more efficient heavy truck designs. Estimates at DAF Trucks and Scania show that on a long haul route, with moderate hills, 30-35% of the fuel consumption is related to overcoming aerodynamic drag (Lögdberg, 2006). Since it is claimed that the underhood of a truck can contribute up to half of the total aerodynamic drag (Söderblom et al., 2012), investigating this area is a first step towards improving the fuel efficiency of trucks. Where most of the efforts into aerodynamic optimization of trucks focusses on the upper half (i.e. roof spoilers and cabin shapes), little effort was put into the underhood.

The aim of this thesis, performed at DAF Trucks N.V., is to construct a model that is able to visualise the flow phenomena in the wheelhouse area and check whether they are in agreement with the literature. For these applications CFD simulations are best suited since they give a fast and detailed insight into the flow field. To gain an understanding of the flow sensitivity to changes in geometry different variants will be simulated. Analysis of these variants should reveal the dominant flow structures and their effect on drag coefficient, after which an approach for the design of wheelhouses can be presented.

This thesis will begin with a discussion of the limitations and assumptions made. A literature review of the studies on both the aerodynamics of wheelhouses and isolated wheels is presented in Chapter 2. Chapter 3 presents a validation study to obtain reliable model settings. Chapter 4 presents the baseline truck model and the different variants that will be simulated. The results of the baseline truck model and variants are presented, analysed and discussed in Chapter 5. Finally, the conclusions and recommendations can be found in Chapter 6 and Chapter 7, respectively.

1.1 Model assumptions

For a fast turnaround time a simplified model was required, which placed limitations on the complexity. This section briefly discusses the main limitations.

The turbulence in this thesis was modelled using steady state RANS. If resources allowed, turbulence modelling was preferably done with LES. It was seen, however, that the requirements for LES modelling were beyond the capabilities in this thesis: it was seen that LES simulations for a 40 million cell model took 60 days on 192 processors (Axerio-Cilies, 2012). The computational power in this thesis was limited to 80 processors. This shows that LES modelling for the current project is beyond the capabilities. Furthermore, it was seen that unsteady RANS simulations significantly increased the computational time and only is suited when the unsteadiness is deterministic (Iaccarino et al., 2003). For these reasons it was chosen to use a steady state RANS model.

Wheel rotation can be modelled in several ways: rotating wall, Multiple Reference Frame (MRF) or a Sliding Mesh. It was concluded in the literature, based on flow fields only, that the sliding mesh approach showed the best agreement with experimental data, with an increase in computation time in the order of 15-20% (Söderblom et al., 2012). It was also shown in the report that the flow field is very sensitive to the choice of MRF region and that domain should therefore be considered. It was shown that in most studies wheel rotation is modelled with a specification of velocity on the wall, resulting in an adequate approximation of wheel rotation (McManus and Zhang, 2006). Following the literature, it was chosen to model the wheel rotation with a specification of velocity on the wall.

In order to achieve a fast turnaround time, a half model approach is used. Adding a symmetry plane through the centreline saves half of the cells and reduces computation time. Due to the geometrical symmetry of the model and the symmetry of the steady state RANS, this is a valid approach. In the literature it was seen that using a half model in a steady state flow field resulted in an error of 1% (Ahmad et al., 2009).

In STAR-CCM+ v7.06 three types of cells can be used to generate a volume mesh: polyhedral, tetrahedral and hexahedral cells. Tetrahedral and polyhedral meshes are best advised for rotating flows, or for flows where the main direction(s) cannot be aligned with an orthogonal set of faces. A comparison of polyhedral and tetrahedral cells yields that the polyhedral cells, for the same accuracy, require less cells and computation time. On the other hand, polyhedral cells are computationally more expensive. It is generally advised, unless resources are limited, to favour polyhedral cells over tetrahedral cells (CD-adapco, 2013; Peric and Ferguson, 2005).

It is known that hexahedral cells perform well if the flow direction is normal to the faces of the mesh; this is best suited for the modelling of freestream flow, where the faces of the cells can be aligned with the main direction of the flow. Since the polyhedral cells have more neighbours, they require more storage and are therefore more expensive than hexahedral cells (CD-adapco, 2013). Considering that the domain for the validation model (and full-scale truck model) is rectangular, the main direction of the flow is known and computing power is limited, the volume was meshed using hexahedral cells.

Chapter 2

Literature overview

In this chapter the results of the literature study will be presented. The goal of the literature study was to gain more knowledge on the phenomena of flow in the wheelhouse and the simulation methods. The literature study was conducted in two stages, a study on isolated wheels, presented in Section 2.1, followed by a study on shrouded wheels, presented in Section 2.2. A summary of the experiments and simulations is presented in Section 2.3.

2.1 Isolated wheels

Before it is attempted to study the aerodynamics of shrouded wheels, a more fundamental approach is to start with the aerodynamics of isolated wheels. Studying the flow patterns near an isolated wheel will give insight into the dominant structures in the complex flow, which might yield a better understanding of the behaviour of a wheel in the wheelhouse. Furthermore, it will give an insight into the most common settings used with CFD. The majority of the studies presented in this section are performed on idealized, non-deformable wheels.

This section starts with an overview of the experiments that have been performed up to this date, in Section 2.1.1, after which the physics and flow mechanisms around the isolated wheels (rotating and stationary) are presented in Section 2.1.2. Subsequently the dominant flow structures are discussed in Section 2.1.3 and the behaviour of the flow in the wake in Section 2.1.4. Finally, studies focussing on non-idealized tyre models are presented in Section 2.1.5.

2.1.1 Overview of previous studies

This section will present an overview of the experiments and simulations that are performed up to this date. Understanding the research of other experimentalists on isolated wheels is the first step in understanding the flow in the wheelhouse. The literature review will unveil the pitfalls and conclusions of other researchers, and serves as guidelines for future work.

The first experiments into the aerodynamics of isolated wheels focussed on effects of yaw, geometry and the ground clearance on lift and drag (Morelli, 1969). The experiments were performed on a 1960's racing wheel in a wind tunnel with a stationary floor. Since wheel rotation cannot be modelled correctly without a moving floor, it was proposed to raise the wheel off the floor (and eliminate the contact between the floor and the tyre) (Morelli, 1969). One of the observations was that an isolated rotating wheel produces downforce, which is in contrast with the expectations that a rotating wheel would produce lift.

(Stapleford and Carr, 1970) performed experiments to explore a set of design parameters, such as wheel ground clearance, wheel width-to-diameter ratio and the effect of a moving ground. The initial experiments were performed with rotating wheels and a static floor. The same problem with wheel rotation as (Morelli, 1969) was encountered. To correctly replicate the contact patch it was proposed to suspend the wheel off the floor and filling the clearance gap with strips of paper. One of the observations was that a rotating tyre with a clearance gap produces downforce, but produced lift as soon as the gap was sealed: the clearance gap accelerated flow under the wheel, creating a strong suction. This was the reason (Morelli, 1969) measured downforce on the rotating tyre (Axon, 1999). It was found that both lift and drag on the tyres increased with decreasing ground clearance. A small study with moving floor was also performed, but since the clearance gap remained the results did not change significantly compared to the static case. The most representable case, with an actual contact patch, could not be applied due to the limitations of the measurement system.

A breakthrough for the knowledge of isolated rotating wheels came when researchers were able to correctly recreate the contact patch and the rotation of the wheel in their experiments, resulting in more reliable results. The experiments of (Fackrell, 1974) contained a representative representation of contact patch and wheel rotation, and therefore is considered to be the beginning for the work on aerodynamics of isolated wheels. Lift- and drag coefficients in previous experiments were obtained (e. g. (Morelli, 1969; Stapleford and Carr, 1970)) with a force balance. As demonstrated in the experiments by (Stapleford and Carr, 1970) lift and drag could not be measured in every setup using a force balance. However, (Fackrell, 1974) measured the pressure with pressure taps on the surface. This resulted in the pressure coefficient distribution on the surface of the wheel, as well as the lift- and drag coefficient, which can be obtained by integration the pressure directly.

The first known CFD investigation on isolated wheels, using a steady state RANS solver, resulted in a clear picture of the flow field (Axon, 1999). The wheel was modelled as a solid disc with chamfered edges. There was a good agreement in the flow field between the simulations and (Fackrell, 1974)'s experiments. Although the general flow field was captured well, the simulations showed poor agreement in the separation zones. It was suggested that the assumption of a fully turbulent boundary layer, in the RANS simulations, resulted in an underprediction of the peak pressure on top of the wheel, since the real flow over the wheel in the validation experiments experienced transition. The magnitude of the error in the location of separation, computed with simulations, is approximately 30° further around the wheel (Axon, 1999; Fackrell, 1974).

Further experiments (Mears et al., 2002, 2004a) and simulations (Skea et al., 2000; Mears et al., 2004b) were conducted on isolated wheels. The flow field in the wake, and on the surface, was measured with pressure probes and PIV. The experimental results, with one minor exception, by (Fackrell, 1974) were confirmed with simulations and experiments. The measurements and PIV experiments showed that the wake of the wheel is highly three-dimensional and unsteady, which implies the need for a time dependent solver (Mears et al., 2004a,b).

Laser Doppler Anemometry (LDA) was used by (Wäschle et al., 2004) to obtain velocity and pressure fields in the wake of the isolated wheel. The measurements were compared to two different commercial CFD codes. The results from the both codes (transient Lattice-Boltzmann and steady RANS) showed good overall agreement with the measurements, and it was claimed that there was no clear best. In other studies, LDA was used to measure the distribution of flow in the wake and established a new overview of the flow field near and behind an isolated wheel (Knowles, 2005). Although the main focus of that study was on the interference of the support sting with the flow in the wake of the race car, the author was able to present findings on the distribution of the wake of isolated wheels.

(Dimitriou and Klussmann, 2006) performed an extensive series of wind tunnel tests to accurately determine the vertical load acting on isolated wheels, as well as the aerodynamic effects. The authors claimed that with the existing measurement techniques the measured lift forces on an isolated wheel cannot be easily validated, which adds to the uncertainty of the results. They develop a new method to obtain lift and drag from the pressure distributions, which was the main reason for their experiments. Simultaneously, experiments to determine the influence of edge profile, rims and wheel covers, and grooves were performed.

A detailed description of the flow structures around an isolated wheel, both with stationary, as well with moving ground, is given in (McManus and Zhang, 2006). The lift- and drag coefficients computed with unsteady RANS show good agreement with the experimental data of (Fackrell, 1974). In case of the rotating wheel, the agreement on surface pressure measurements near the contact patch is poor, which is reflected in the value of the lift coefficient. Furthermore, the Spalart-Allmaras and Realizable $k-\epsilon$ turbulence models were tested. The grid sensitivity of the computations was studied and shown to be small, with both turbulence models.

The wake of rotating and stationary Formula 1 tyres was studied with PIV experiments, as well as RANS and LES simulations (Axerio et al., 2009; Axerio-Cilies, 2012). The LES simulations show a better agreement with PIV measurements, in the position of the vortex cores than the RANS simulations, which are known for having trouble modelling highly separated and three-dimensional flow. It was claimed that, if time constraints allow, LES is always preferred over RANS. Unsteady RANS simulations showed an improvement in predicting the vortex cores, although not all wake dynamics that were captured by LES were revealed (Axerio-

Cilies et al., 2012). Finally, it was found that the velocity profile in the wake is sensitive to minimal changes in tyre shape, such as the geometry of the contact patch and orientation of tyre grooves (Axerio-Cilies, 2012).

2.1.2 Physics

This section presents the basic flow field found behind an isolated tyre. This includes the flow behaviour near the contact patch, effects of rotation and other phenomena.

The technique used to measure the pressure on the surface of the wheel, introduced by (Fackrell, 1974), was the first step in understanding the distribution of flow near the isolated tyre. This resulted in the centreline pressure coefficient distributions over the surface of the tyre, illustrated in Figure 2.1. The pressure measurements were obtained using pressure taps on the surface of the wheel, averaged over several wheel rotations (Knowles, 2005). The sign convention of the wheel is defined counter clockwise (i.e. same direction of rotation as the wheel), with the contact patch located at 90°, see Figure 2.2.

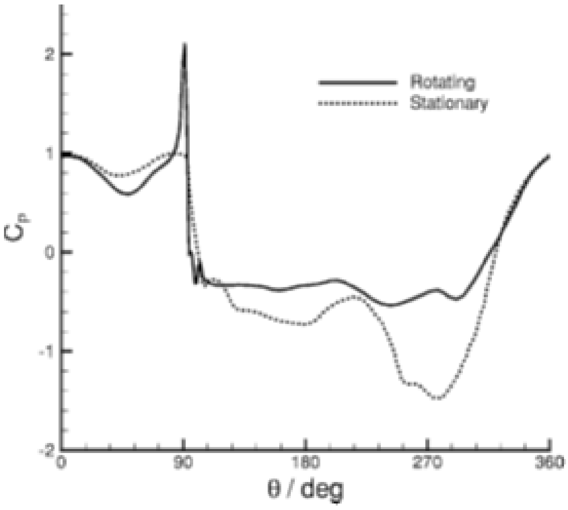

Figure 2.1: Pressure coefficient distribution in centreplane of an isolated tyre (Fackrell, 1974)

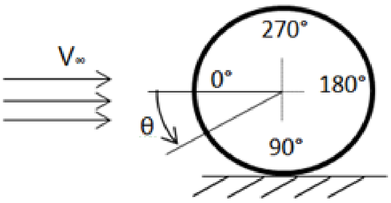

Figure 2.2: Sign convention isolated wheel, introduced by (Fackrell, 1974)

It can be seen in Figure 2.1 that the freestream air experiences a drop in pressure as it flows over the top of both the stationary and rotating wheel. It can also be observed, though, that the suction on the stationary wheel is significantly higher than on the rotating wheel. The pressure coefficient with the stationary wheel exceeds a pressure coefficient of -1, while the pressure coefficient with the wheels rotating does not reach that value. Since the airflow moves in the opposite direction of the movement of the rotating wheel (and the attached boundary layer) the freestream flow encounters a strong resistance (Fackrell, 1974). Separation will therefore occur earlier than the flow over the stationary wheel: the location of separation of the rotating tyre is approximately 70° earlier than the stationary tyre, which can be verified by observing Figure 2.1 carefully (Axon, 1999). Note that the boundary layer itself remains attached and follows the direction of rotation of the tyre (Knowles, 2005).

Observing Figure 2.1, another difference between rotating and stationary wheels can be identified in the rotating case. Just in front of the contact patch a strong peak in pressure coefficient can be observed in the rotating case. Due to the two converging boundaries, created by the rotation of the wheel, work is being done on the flow near the contact patch (hence: $C_p > 1$). This coincides with squeezing the air in- or outboard ('jetting') (Fackrell, 1974; Axon, 1999). After the contact patch, a negative pressure peak also appears. It has been postulated that if two converging boundaries result in a positive pressure peak, two diverging boundaries should result in a negative pressure peak (Fackrell, 1974). This negative pressure was not observed in the initial experiments, but its existence has been verified in later experiments (Mears et al., 2002).

The rotation of the wheel results in a higher pressure on the surface, and in the wake, of the wheel, as can be observed in Figure 2.1. Although the rotating tyre experiences an earlier separation, both lift and drag forces will decrease with the rotation of the wheel. There are no conditions, however, where the rotation of the wheel compensates for the loss of attached flow (Wäschle, 2007).

2.1.3 Vortex structures

To gain a better understanding of the flow over the isolated wheels behaves, the main phenomena occurring are identified. The flow surrounding the isolated wheel is dominated by boundary layer separation. The vortex skeleton method by (Régert and Lajos, 2007) was the best way to identify the vortex structures surrounding the isolated wheel. These are described for different cases between the isolated stationary and rotating wheels, and their difference, respectively.

Stationary tyres

The vortex structures near the stationary tyre are presented in Figure 2.3. The flow behind the isolated wheel is dominated by a pair of counter-rotating vortices (CVP), see (1) in Figure 2.3 (and 2.4). As the freestream air flows over the sides of the wheel it entrains the flow over the top (centre) of the wheel. This results in an attached flow over the surface of the wheel, which leads to a strong downwash behind the tyre. This down-wash impings on the ground, roll ups and forms the CVP (Axerio-Cilies et al., 2012).

The second pair of vortices that make up the flow picture originates at the contact patch.

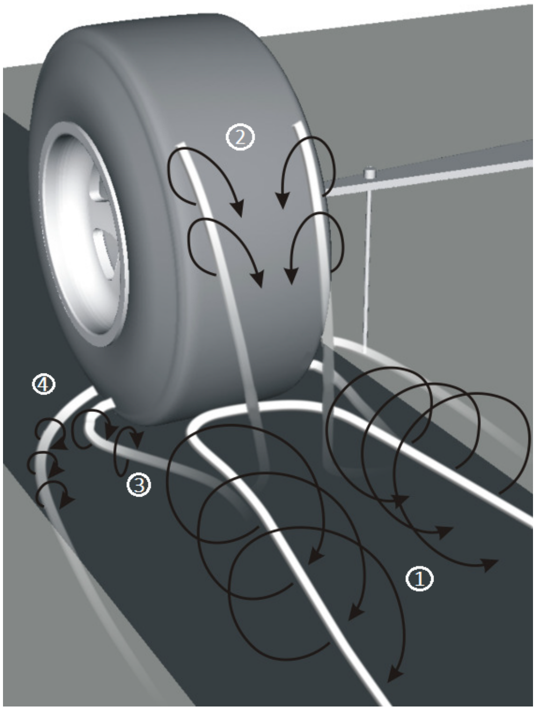

Figure 2.3: Sketch of dominant vortex structures behind a stationary wheel (Wäschle, 2007)

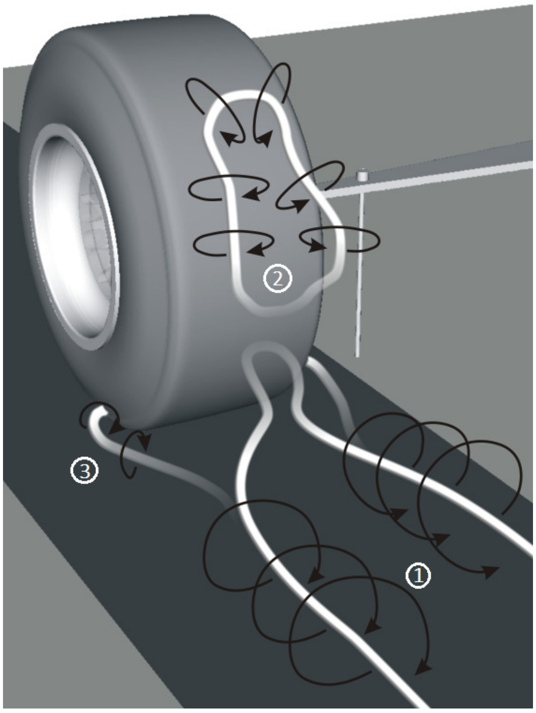

Figure 2.4: Sketch of dominant vortex structures behind a rotating wheel (Wäschle, 2007)

Since the air near the contact point cannot flow into the ground, there is a strong tangential velocity component allowing the flow to evade the wheel. This strong component cannot follow the sharp edges of the tyre and separates. The separated flow is entrained by the freestream, creating a shear layer between the high and low speeds in the domain. Due to the high momentum and the presence of the shear layer, the flow from the contact patch will roll up and form the second pair of vortices (McManus and Zhang, 2006; Wäschle, 2007). It must be noted that the air evading the contact patch shows a behaviour similar to the jetting, but should not be mistaken with the actual jetting which occurs on rotating wheels only. Nevertheless, the vortex structure will be referred to as jetting vortex.

Furthermore, in front of the jetting vortex a second vortex can be identified: the horseshoe vortex (4). The presence of the horseshoe vortex was already postulated but was never observed experimentally. Using CFD, the presence of the horseshoe vortex has been reported and observed by multiple researchers (e.g. (Axerio-Cilies et al., 2012; Wäschle, 2007), whereas others could not detect the vortex and doubt its existence (e.g. (McManus and Zhang, 2006)).

Finally, in Figure 2.3 a set of top-vortices can be identified. The top-vortices have the same direction of rotation as the CVP, but are smaller in size and strength. It is believed that the low pressure region behind the wheel sucks in the air that flows over the side of the wheel, resulting in separation of the flow over the shoulder of the tyre (McManus and Zhang, 2006; Knowles, 2005). It can be shown that covering the hub will not affect the formation of the top-vortices (Axerio-Cilies et al., 2012), i.e. the edges of the tyre are the main cause for the generation of the vortex.

Rotating tyres

In Figure 2.4 flow surrounding the rotating wheel is sketched. As discussed, the jetting is a feature observed by the rotating wheel only, and can therefore be identified clearly, see 3 in Figure 2.4. It is claimed that the energy transferred from the wheel diminishes the jetting vortex strength in the wake (Wäschle, 2007).

The flow pattern over the top of the wheel is different compared to the stationary wheel. The resistance the flow encounters flowing over the top of the wheel results in separation of the freestream flow, near the top of the wheel (Fackrell, 1974) (sketched with (2) in Figure 2.4). Note that the boundary layer itself remains attached and follows the direction of rotation of the tyre. The flow over the sides of the wheel cannot entrain the flow over the top of the wheel as effectively as in the stationary case, resulting in a large separation region behind the wheel and a weaker CVP (Wäschle et al., 2004; Knowles, 2005).

Experiments have also shown that there are two top-vortices originating from the shoulder of the top of the rotating tyre, similar to the vortices in the stationary case. The vortices roll up on the shoulders of the top of the wheel, immediately following the flow separation (Saddington et al., 2006; Axerio-Cilies, 2012). The sketches presented in Figure 2.4 are therefore not entirely correct, but nevertheless still the clearest available in the literature.

2.1.4 Wake structure

To have an even better understanding of the flow, it is essential to understand the development of the flow structures downstream.

The first research of the downstream flow field was performed by (Fackrell, 1974). The total pressure in the wake was measured with Kiel tubes (insensitive to a flow angle of ±35°), defining the wake as the region with less than 90% of the total pressure. Due to the high unsteadiness of the wake, and the possibility of overshooting the 35° threshold of the Kiel tube, the validity of these results was argued (Axon, 1999). Experiments by (Bearman et al., 1988) indicated that the wake is dominated by the CVP, with a significant difference in strength (and location) between the rotating and stationary wheel. The CVP emanating from the stationary wheel was stronger than the CVP found in the rotating case, since the downwash is much stronger (Axerio-Cilies, 2012). Furthermore, the CVP of the stationary case remained close to the ground, whereas the CVP from the rotating case was situated at approximately 0.25D (Bearman et al., 1988).

Figure 2.5 presents pressure measurements in the wake, obtained with LDA (Wäschle et al., 2004). It can be seen that wake structure down-stream (x/D = 0.7) differs for the rotating and stationary wheel and agrees with the conclusions drawn by (Bearman et al., 1988). It can be seen that the pair of counter-rotating vortices for the rotating wheel are closer together, and are much weaker compared to the stationary wheel (Wäschle et al., 2004). Further downstream it can be observed that the wake structure of the stationary wheel remains wider than the wake of the rotating tyre. It was expected that due to jetting, the wake for the rotating wheel would be wider, but the opposite is observed though (Wäschle et al., 2004; McManus and Zhang, 2006; Knowles, 2005). The wider wake of the stationary tyre is a direct effect of the presence of the horseshoe vortex (Axerio-Cilies et al., 2012).

Furthermore, it can be seen that the wake of the rotating tyre is a lot taller than the wake of the stationary tyre. The rotating wheel experiences the separation on top of the wheel, which results in a taller wake, and a wake region in the upper half of the wheel. This can be seen immediately behind the wheel, as well as further downstream (Wäschle et al., 2004; McManus and Zhang, 2006).

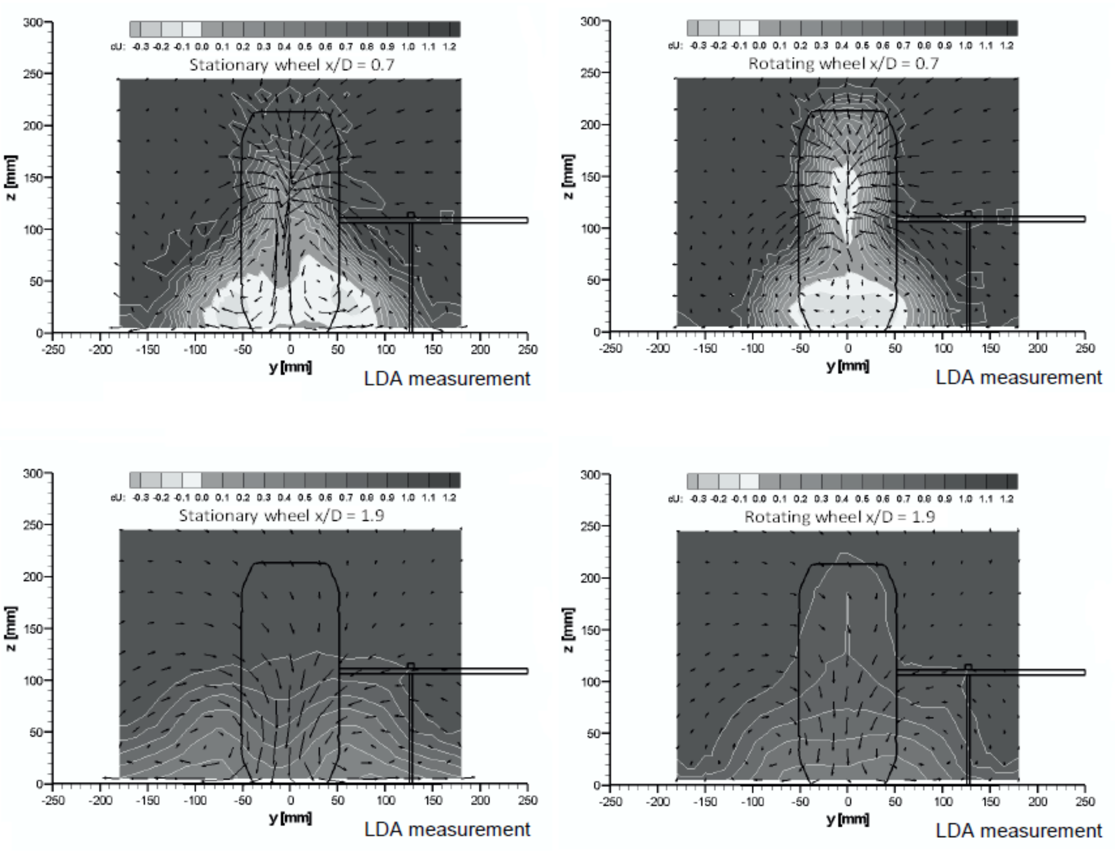

Figure 2.5: Wake structure of isolated and rotating wheel at different locations in the wake (Wäschle et al., 2004)

2.1.5 Non-idealized tyre models

Simplified models for the tyres are used in most experiments. They contain some sort of edge representation, but other details, such as grooves and tyre roughness are usually neglected. This section will present the effects of grooves, hub-flow, deformation and camber, respectively, on the aerodynamic characteristics of an isolated wheel.

Experiments have shown that a rotating tyre with grooves does not encounter the jetting phenomenon (Dimitriou and Klussmann, 2006). With grooves it was seen that the tyre experiences the jetting phenomenon due to the convergences of two boundaries. Without grooves the need for jetting is eliminated, since the air is allowed to flow through the grooves of the tyre. Figure 2.6 presents the difference in velocity field as a result of including grooves in the tyre, compared to a solid tyre. The mass flow through the grooves is evident, but also a shift in the shear layer can be observed. The mass flow through the grooves results in a shift of the shear layer (less jetting) and a decrease in drag (higher backpressure) (Axerio-Cilies, 2012). It is claimed that adding 0.45 cm deep grooves in an isolated rotating tyre decreases the tyre drag by 4.2% (Axerio-Cilies, 2012), but increases the intensity of the CVP with 1%. Since the jetting is not seen on the stationary tyre, adding grooves to a stationary tyre does not result in a change in velocity field (Axerio-Cilies, 2012).

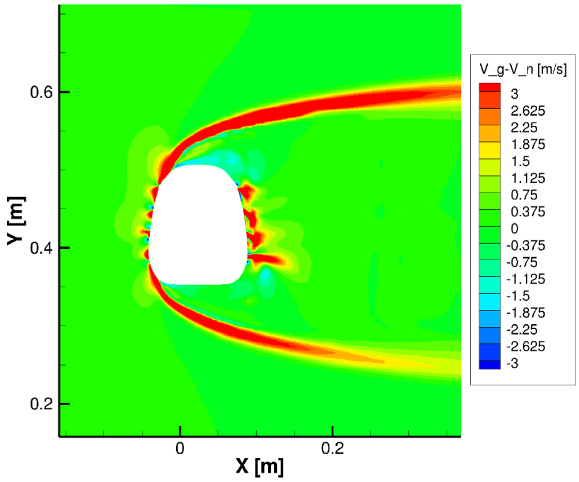

Figure 2.6: Change in velocity magnitude as a result of adding grooves to an isolated rotating wheel (Axerio-Cilies, 2012)

(Sprot et al., 2011) performed an investigation into the effects of hub flow on the aerodynamic characteristics of an isolated Formula 1 wheel. The basic principle of flow through the hub is sketched in Figure 2.7. One of the effects of through flow in the hub is that the formation and strength of the counter-rotating pair of vortices is affected. The airflow flowing out of the hub ends up in the outboard vortex, re-energizes the flow and suppresses the formation of the CVPs. The investigation of (Axerio-Cilies, 2012) confirms that the vortex formation on the outboard of the wheel can be influenced when air is allowed to flow through the hub. According to (Sprot et al., 2011) significant drag savings can be achieved when the formation of the CVPs is suppressed by the hub-flow.

Experiments on a model tyre by (Sprot et al., 2012) have shown that the deformation of tyres can have a significant effect on the flow. This is because the flow is strongly influenced by the sidewall shape. Examples of high and low tyre deformation are shown in Figure 2.8 and 2.9. A tyre with high deformation (i.e. a larger contact patch) generally experienced less drag than a tyre with low deformation. The tyre with low deformation (smaller contact patch) has a large gap on the outboard side. It has been observed that this larger gap encourages low

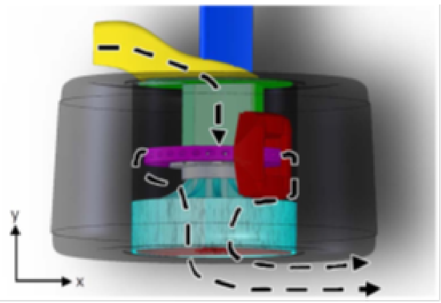

Figure 2.7: Common F1 front wheel assembly and suggested flow pattern through the hub (Sprot et al., 2011)

pressure flow and higher vorticity (Axerio-Cilies, 2012). The formation of the jetting vortices is suppressed, but this does not prevent the formation of the wider wake region. The same reasoning can be applied to cambered tyres, where it is observed that low camber tyres have a stronger downwash, which reduces the size of the separation bubble behind the rotating tyre. Tyre drag savings in the order of 5-6% are claimed by applying large deformation on the tyre (Axerio-Cilies, 2012).

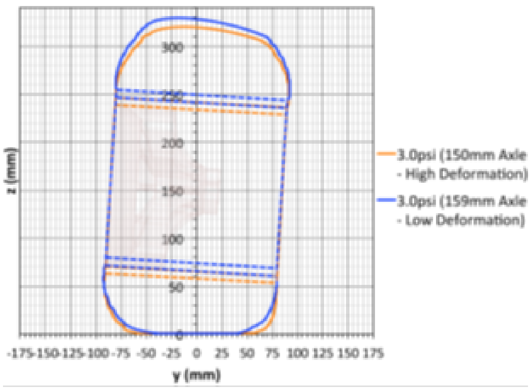

Figure 2.8: Geometry of the tyre profile under high and low deformations (Sprot et al., 2012)

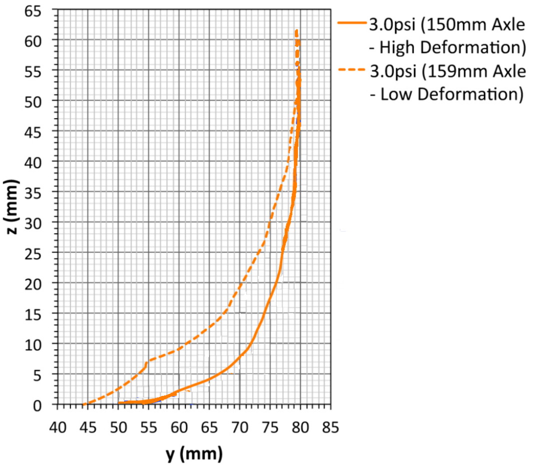

Figure 2.9: Close-up of the tyre profile under high and low deformations (Sprot et al., 2012)

2.2 Shrouded wheels

The goal of this section is to present the current knowledge of the flow in a wheel-wheelhouse configuration. The wheelhouse adds considerable complexity to the system compared to the isolated wheels. In contrast to the isolated wheel case the models presented in this section focusses on the aerodynamics of rotating wheels only, unless mentioned otherwise.

This section starts with an overview of the experiments that have been performed to date, in Section 2.2.1, after which the physics and flow mechanisms are presented in Section 2.2.2. Finally, the parametric studies that have been performed to date, and parameters that are known to influence the flow field in the wheelhouse, are presented in Section 2.2.3.

2.2.1 Overview of previous studies

Over the years, experiments and computations have resulted in a description of the wheelhouse flow of simplified model. Understanding the research of other experimentalists is the first step in understanding the flow in the wheelhouse of a full-scale truck. The literature review will unveil the pitfalls and conclusions of other researchers, and serves as guidelines for future work.

After his work on isolated wheels, (Morelli, 1969) was the first experimentalist to conduct research into the effect of wheels inside a wheelhouse. The studies were performed inside a wind tunnel, but due to the cavity between the wheel and the stationary ground the data was claimed to be unreliable (Axon, 1999).

(Oswald and Browne, 1981) performed experiments with a car on a test track. Tufts were attached in the wheelhouse, to visualize the direction of the flow. An adjacent vehicle, and cameras inside of the wheelhouse, were able to photograph the direction of the tufts during the tests. This flow field information was then used to decide the placement of a hot wire anemometer in the wheelhouse to obtain more accurate measurements. In the end a flow model, depicted in Figure 2.10, could be constructed.

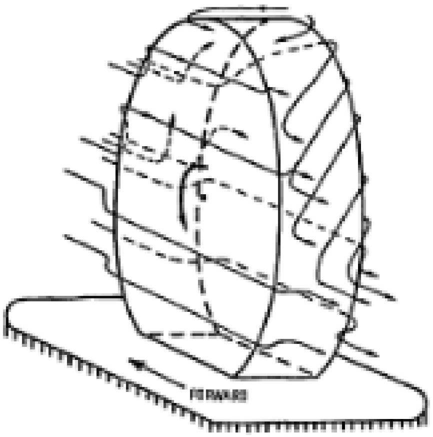

Figure 2.10: Flow field visualization obtained with tufts and hot wire (Oswald and Browne, 1981)

(Cogotti, 1983) performed wind tunnel tests on a passenger car with stationary wheels. It was found that the wheelhouse draws the airflow from the underbody and creates a highly yawed flow. Experiments on an idealized body with two front wheels, resulted in the conclusion that lift and drag are minimal if the wheelhouse volume was kept as small as possible. It was noted though, that the experiments on the idealized body may not be applicable to passenger cars (Cogotti, 1983).

Following the experiments of (Cogotti, 1983) studies into wheelhouse geometry were performed (Fabijanic, 1996). Several parameters were altered on the wheelhouse of the model to identify the changes in lift and drag. One of the main conclusions was that drag increased when the wheelhouse radius was increased and the wheelhouse depth was increased. This generally agrees with (Cogotti, 1983)'s findings that wheelhouse volume should be kept as small as possible. The main part of the drag increase originated in the interaction of the flow out of the wheelhouse, with the rest of the body.

The first CFD computations on the wheelhouse geometry were performed on the model shown in Figure 2.11(a) (Axon, 1999). The asymmetric shaped body contained a solid disc with chamfered edges to represent the wheel. The influence of the wheels on the shroud, the geometry of the shroud, and the thickness of the stationary ground plane boundary layer were investigated using both computations and wind tunnel experiments. Surface pressure measurements on the wheel and in the wheelhouse resulted in a clear picture and understanding of the flow inside of the wheelhouse. It was found that lowering the ride height and incorporating spoilers on the model help decrease drag. Furthermore, increasing the stationary boundary layer thickness on the ground plane was found to affect the pressure on the lower half of the wheel and resulted in a drag reduction.

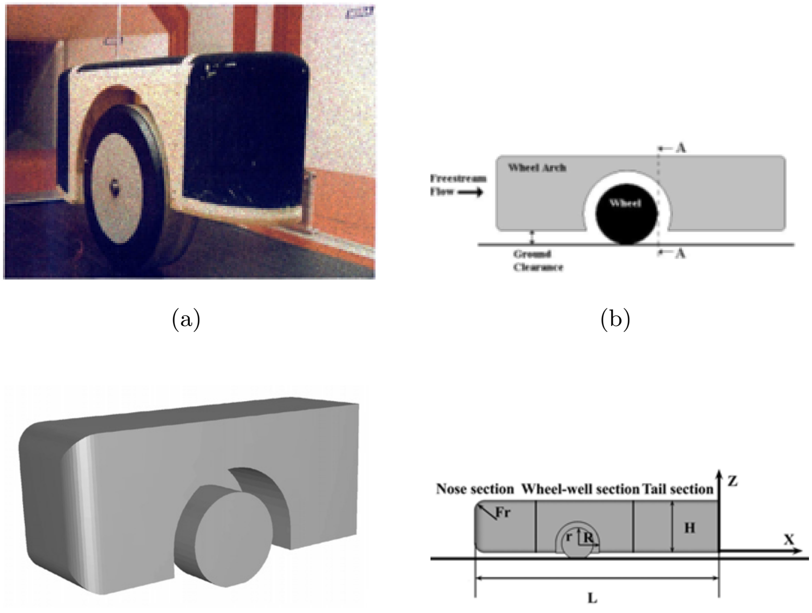

(a) (b)

(c) (d)

Figure 2.11: Wheelhouse models used in the studies of 2.11(a) (Axon, 1999), 2.11(b) (Skea et al., 2000), 2.11(c) (Régert and Lajos, 2007) and 2.11(d) (Krajnović et al., 2011). Although models 2.11(b)-2.11(d) are all derived from (Fabijanic, 1996), the geometry was altered to the experimentalists' needs

Computations and experiments performed by (Skea et al., 2000) on the model shown in Figure

2.11(b), indicated that the disturbance of the wheel in the wheelhouse to the freestream air flow was significantly less than that of the isolated wheel. Comparison with experiments showed that the general pattern of the flow was predicted by the CFD code, but due to the transient nature of the flow, some patterns were not captured. It was postulated that with better models certain features (e.g. the up flow and suction peak) can be better captured.

(Damiani et al., 2004) presented the first investigations using transient simulations for two wheel wheelhouse configurations (the MIRA model (Axon, 1999) and a realistic car model). Both a steady state and unsteady state solver were considered. The increase in drag with rotating wheels was captured by both the steady and unsteady (immersed boundary) RANS methods and it was found that the unsteady method is preferred.

A flow picture of the flow in the wheelhouse was constructed by (Régert and Lajos, 2007), using vortices identified with the Q-criterion (Jeong and Hussain, 1995). The wheelhouse geometry that was used in the studies is depicted in Figure 2.11(c). It was found that the presence of six vortices can be classified as qualitatively independent of the grid, numerical scheme, turbulence model and the shape of the body, but the strength and position of the vortices depended on the profile of the wheel and yaw angle of the approaching flow (Régert and Lajos, 2007). The conclusions concerning the location and strength of the vortex cores were later supported with LES simulations (Krajnović et al., 2011).

(Régert and Lajos, 2007) also presented a study into the aerodynamic effects of changing the wheelhouse topology. It was found that the forces on the body, and flow structures in the wheelhouse were affected significantly when the opening on the bottom side was closed. However, the effect on forces and flow structures was less when only the side gap is covered. This supports the view that the flow in the wheelhouse interacts strongly with the flow from the underbody.

Experiments into the wheelhouse flow of a half-scale BMW Z4 model were presented in (Dimitriou and Klussmann, 2006). The change in pressure coefficient as a result of the wheelhouse was presented. It was shown that enclosing the wheel resulted in different pressures on top of the surface of the wheel. It was claimed that as a result of the yawed inflow, as discussed by (Cogotti, 1983), it is necessary to have a detailed representation of the wheel rims. Furthermore, it was found that adding a spoiler decreases the pressure in the wheelhouse, resulting in a decrease of drag coefficient (as was seen in idealized cases (Axon, 1999)).

Simulations on a full-scale passenger car showed that modelling the wheels with a rotating wall condition is sufficient for capturing the correct drag figures (Duncan et al., 2010). It was postulated that local changes in transient flow caused by the rotation of the wheel rim openings do not have a significant aggregate effect on the wheel forces. Simulations containing a no-slip condition on the wall, combined with a velocity specification, should therefore yield reasonable results. It was observed that using a scanned geometry results in better predictions than when CAD data is used (Duncan et al., 2010; Sebben and Landström, 2011).

The recent experiments by (Söderblom et al., 2012) aimed to investigate the local flow field around the wheels and in the wheel housing on a heavy truck; and how different approaches to modelling the wheel rotation in CFD influences the results. Emphasis was on effects of ground simulation and different wheel rotation models. It was found that changes in the local velocity field could have dramatic effects downstream.

2.2.2 Physics

In the same way as for isolated wheels, the flow around the wheel in the wheelhouse can be analysed by identifying the vortex structures surrounding the wheel. This section will present the aerodynamic characteristics of the shrouded wheels, compare them to those of isolated wheels. Furthermore, the vortex structures and the behaviour of the flow in the wake will be presented. Unless mentioned otherwise, the configuration has rotating wheels.

A pair of jetting vortices is present in a wheel-wheelhouse configuration and can be identified in Figure 2.12, labelled L and R. Since the jetting phenomenon is caused by the convergence of two moving boundaries (i.e. the wheel and the floor) the formation of these vortices is not affected by the presence of the wheelhouse (Régert and Lajos, 2007).

The presence of the wheelhouse has a significant influence on the direction and structure of the flow. Figures 2.12 (obtained with LES simulations (Krajnović et al., 2011)) and 2.13 (RANS simulations (Régert and Lajos, 2007)) present the vortex structures surrounding the wheel inside the wheelhouse. Figure 2.12 presents a detailed overview of the position and size of the vortex cores. Contrarily, the vortex skeleton model in Figure 2.13 gives a more apprehensive overview of the vortex structures. It is claimed that there is a good agreement between the flow structures found with LES and RANS simulations (Krajnović et al., 2011).

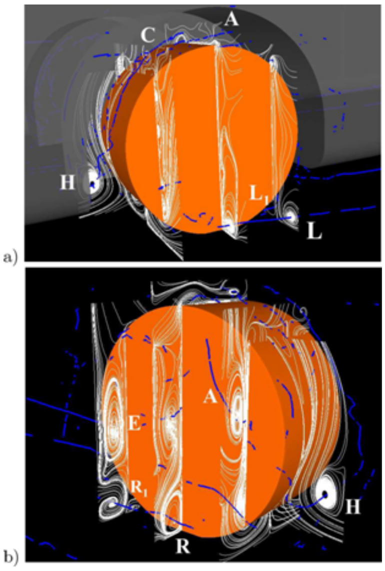

Figure 2.12: Vortex cores and time-averaged streamlines (Krajnović et al., 2011). The freestream flow direction in (a) is from left to right, (b) from right to left

Vortices H (same direction of rotation as the wheel), S and C are solely the result of flow separating over the edges of the wheelhouse (Régert and Lajos, 2007). The formation of

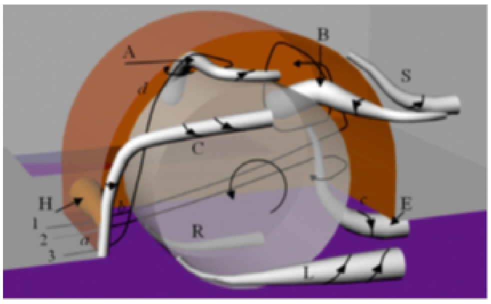

Figure 2.13: Vortex skeleton of flow in a wheelhouse (Régert and Lajos, 2007)

vortex A begins with flow entering the wheelhouse from the underbody, as is sketched with streamline 3 in Figure 2.13. The flow moves up over the surface of the wheel, and separates as a result of the wheel rotation, similar to the separation of flow of the rotating tyre in the isolated case (Régert and Lajos, 2007). The direction of rotation of vortex A is opposite to the rotation of the wheel (and its boundary layer). The vortex is elongated in the direction of the wheelhouse and reaches the inner wall. When the flow hits the outboard side of the wheel, it is deflected into the main stream, and the vortex is stretched (Régert and Lajos, 2007).

Vortex B originates with flow entering from the underbody via streamline 1 in Figure 2.13, and impinging on the end of the wheelhouse. The direction of rotation corresponds to the rotation of the wheel (Régert and Lajos, 2007). Vortex B moves behind the wheel and is finally elongated in the freestream. It must be noted that the existence of vortices A and B is doubted in realistic configurations, since the path of these vortices would be obstructed by the driveshaft, which is not modelled (Krajnović et al., 2011; Régert and Lajos, 2007).

Vortex E forms as the flow separates behind the wheel (streamline (2) in Figure 2.13), and is sucked into the freestream under the underbody (Krajnović et al., 2011).

Finally, two additional vortices, L_1 and R_1, were identified with the LES simulations, that were not obtained with the RANS simulations, nor observed in the experiments. These are thought to be as a result of the strong negative pressure peak behind the contact patch the airflow is entrained in the region behind the tyre. Subsequently the air is entrained upwards due to the rotation of the wheel, which results in the formation of vortices L_1 and R_1. The vortices rotate in opposite direction of the main vortices L and R (Krajnović et al., 2011).

In comparison with the isolated rotating wheel a few things can be noted from the pressure coefficient distribution of the shrouded wheel. Note that the sign convention in Figure 2.14 is different from the convention introduced earlier (Figure 2.2); the sign convention is defined clockwise, with the contact point located at 0°. It can be noted that the suction, which is visible in the isolated case (Figure 2.1), disappears under the influence of the wheelhouse. In fact, the pressure slightly rises when it moves over the wheel.

It can be noted that the negative pressure peak, right behind the contact patch, is less negative when compared to the isolated rotating wheel. Due to the yawed inflow, the flow can proceed behind the contact patch. This reduces the accelerations invoked by the diverging boundaries right behind the contact patch (Dimitriou and Klussmann, 2006). As a result the suction peak behind the contact patch is reduced. It can be seen that the pressure coefficient distributions near the edges of the tyre are different from the pressure coefficient distributions on the centreplane of the tyre. The presence of the wheelhouse results in an asymmetric distribution of flow (Axon, 1999).

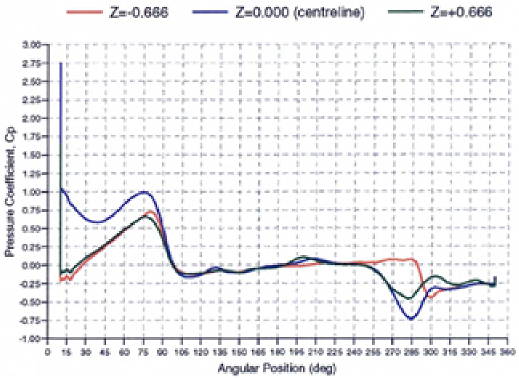

Figure 2.14: Pressure coefficient distribution of a wheel in a wheelhouse (Axon, 1999)

2.2.3 Parametric Studies

This section will present the parametric studies of wheelhouses that are performed to date. The main parameters that are found to have a beneficial effect on the aerodynamic characteristics will be presented. There is a limited amount of studies performed into the truck wheelhouse aerodynamics, therefore studies on cars and simplified wheelhouse models will be presented as well. This section starts with an overview of the conclusions drawn with respect to isolated wheelhouses, after which the aerodynamics of trucks and passenger cars will be presented.

Isolated wheelhouses
In the wind tunnel studies of (Fabijanic, 1996) and (Cogotti, 1983) the observations were made that the wheelhouse volume is an influential parameter. It was reported that keeping the wheelhouse volume as small as possible resulted in the lowest drag. It was postulated that the volume of the wheelhouse is a contributor in the flow out of the wheelhouse, which is closely related to the drag of the wheelhouse (Fabijanic, 1996).

A large parametric study into the effects of geometry changes using CFD was performed on the model presented in (Axon, 1999) (Mavuri and Watkins, 2011). The authors supported their key findings with drag coefficient deltas only, hence lacking flow field information. The effect of the geometry on the position and strength is therefore not known. Nevertheless, certain parameters were found that decreased the drag coefficient of the model. It was found that, applying a chamfer fill to the wheelhouse (see Figure 2.15), a larger clearance gap (gap around the wheel) and lowering ride height were found to have the largest potential in terms of drag savings (Mavuri and Watkins, 2011). The latter observation supports the theory of (Axon, 1999) that lowering the ride height of the wheelhouse is beneficial for the drag coefficient.

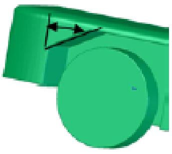

Figure 2.15: Illustration of chamfer fill in a wheelhouse (Mavuri and Watkins, 2011)

Although the flow emanating from the wheelhouse has a significant influence on flow over the back of the vehicle, the development of the wake downstream (i.e. not limited to a few mm behind the wheel) has not received any attention in studies.

Trucks and passenger cars

In the studies of (Dimitriou and Klussmann, 2006) several conclusions were made with respect to the modelling of the tyres. For instance, it was found that a spoiler in front of the tyre is an effective way of reducing drag, an observation which was made earlier (Axon, 1999). Furthermore, due to the yawed flow into the wheelhouse the model of the tyres requires a correct representation of the rims, and it is desirable to model the wheel uprights and suspension components.

There is a strong relation between the flow in the wheelhouse and the flow on the trailer (Söderblom et al., 2009). During studies on a simplified tractor-trailer model it was found that local changes in the flow field can have a significant effect on the global drag values; it was seen that the drag coefficient on the wheel and wheelhouse could decrease, while the drag coefficient of the complete configuration showed an increase. On passenger cars this sensitivity has been found as well (Elofsson and Bannister, 2002). Although some changes have a negative effect, it was found during a parametric study that decreasing the wheelhouse volume resulted in less drag on the complete model.

Furthermore, adding wheelhouse ventilation on the back of the wheelhouse (ducting a part of the wheelhouse flow in order to re-energize the wake down-stream) can have a positive effect as well. It was also postulated, however, that due to the sensitivity of the problem, conclusions drawn with respect to the simplified geometry are not necessarily valid for real trucks (Söderblom et al., 2009, 2012).

2.3 Summary and Conclusions

The goal of this literature overview is to present the current knowledge and obtain a baseline for future work on shrouded wheels. This chapter will present a quick summary of the experiments that were discussed in Section 2.3.1, after which conclusions with respect to the experiments are drawn in Section 2.3.2

2.3.1 Summary

In Tables 2.1 and 2.2 an overview of the known research into (shrouded) wheels is presented.

Table 2.1: Overview of research into isolated wheels

Author	Method	Wheels	Floor
(Morelli, 1969)	Experiment	RW	SF
(Stapleford and Carr, 1970)	Experiment	SW/RW	SF
(Fackrell, 1974)	Experiment	SW/RW	SF/MF
(Bearman et al., 1988)	Experiment	SW/RW	SF/MF
(Mears et al., 2002)	Experiment	SW/RW	SF/MF
(Mears et al., 2004a)	Experiment	SW/RW	SF/MF
(Mears et al., 2004b)	CFD	RW	MF
(Wäschle et al., 2004)	CFD	SW/RW	SF/MF
(Knowles, 2005)	Experiment/CFD	RW	MF
(Dimitriou and Klussmann, 2006)	Experiment	RW	MF
(Axerio et al., 2009)	CFD	SW	SF
(Sprot et al., 2011)	Experiment/CFD	RW	MF
(Sprot et al., 2012)	Experiment	RW	MF
(Axerio-Cilies et al., 2012)	CFD	SW	SF
(Axerio-Cilies, 2012)	CFD	SW/RW	SF/MF

SW: Stationary Wheels, RW: Rotating Wheels, SF: Stationary Floor, MF: Moving Floor

Table 2.2: Overview of research into shrouded wheels

Author	Method	Wheels	Floor
(Oswald and Browne, 1981)	Experiment	N/A	N/A
(Fabijanic, 1996)	Experiment	RW	MF
(Axon, 1999)	CFD	SW/RW	SF/MF
(Skea et al., 2000)	Experiment/CFD	RW	MF
(Elofsson and Bannister, 2002)	Experiment	SW/RW	SF/MF
(Damiani et al., 2004)	CFD	SW/RW	SF/MF
(Thivolle-Cazat and Gilliéron, 2006)	Experiment	RW	MF
(Wäschle, 2007)	Experiment/CFD	SW/RW	SF/MF
(Régert and Lajos, 2007)	CFD	RW	MF
(Söderblom et al., 2009)	CFD	RW	MF
(Sebben and Landström, 2011)	Experiment/CFD	MF	RW
(Duncan et al., 2010)	Experiment	RW	MF
(Krajnović et al., 2011)	CFD	RW	MF
(Mavuri and Watkins, 2011)	CFD	RW	MF
(Söderblom et al., 2012)	CFD	RW	MF

SW: Stationary Wheels, RW: Rotating Wheels, SF: Stationary Floor, MF: Moving Floor

2.3.2 Conclusions

Isolated Wheels

It was seen that the rotation of the wheel differed from the stationary tyre, due to flow separation on top of the wheel and the squeezing of flow in the contact patch. The dominant flow structures around the isolated wheels consisted of three pair of vortices: to start, the jetting vortices, originating in the contact patch was found in both cases. Although the formation of the vortices is different for the rotating and stationary case, they are comparable in size and strength. Furthermore, a pair of counter-rotating vortices and shoulder vortices form from the flow over the top of the wheel. In the stationary case an additional horseshoe vortex could be observed.

It was seen that the shape of the tyre had a strong influence on the flow distribution and drag coefficient. Jetting vortices were suppressed as a result of cambering the tyre. Furthermore, it was seen that a tyre with air flowing through the grooves experiences less jetting. Finally, it has been observed that flow through the hub of the tyre is a powerful method to control the wake of the isolated tyre: flow is injected into the freestream through the hub and re-energizes the slow momentum air.

Shrouded Wheels

The dominant vortex structures surrounding the shrouded wheel were also explored. It was found that six vortices can be classified as qualitatively independent of the grid, numerical scheme and the shape of the body. The strength and size of the vortices varies with changing geometry, but the presence of the six vortices remains. Some flow features show similarities to the structures observed in the isolated case, but the wheelhouse affects the flow field around the wheel significantly.

Several parameters were identified that have a profound effect on the drag coefficient. Air flowing out of the wheelhouse, interacting with the freestream, was found to be a major contributor to drag. Generally, air flows in from the underbody and flows out of the wheelhouse behind the wheel. Ventilating a part of the wheelhouse (i.e. ducting flow downstream) is a powerful way of controlling the wake. Furthermore, it was found that keeping the wheelhouse volume as small as possible and lowering ride height reduces the drag coefficient.

Studies into the shrouded wheels have focussed on the aerodynamics of the wheelhouse. Studies into the behaviour of the flow in the wake of the wheelhouse are not performed. Furthermore, studies into geometry changes in front of the wheelhouse (i.e. the effect flow separating of the vertical front edge) are not presented in the literature.

Chapter 3

Validation

Since no experimental data of flow in a truck wheelhouses was available, a study was performed to validate the model settings. This validation study focussed on the effects of mesh refinement, wall modelling and turbulence models. Furthermore, a comparison between a transient and steady state solver was made. A simplified wheelhouse model was developed by Rover Group Ltd. to investigate wheelhouse aerodynamics. This model and its experimental data were used to validate the model settings, which were later applied on the full-scale truck model.

Section 3.1 presents the model that was used in this validation study. Section 3.2 presents the considerations that were made with respect to the mesh and wall modelling. Section 3.3 presents the results of the mesh sensitivity study. Section 3.4 presents a study of turbulence models and Section 3.5 discusses the difference between transient and steady state modelling. Finally, Section 3.6 presents a summary of this chapter.

3.1 Model description

This section briefly presents the model that was developed by Rover Group Ltd. to investigate wheelhouse aerodynamics. The model was a simplified representation of a wheelhouse and was tested in the MIRA Model Wind Tunnel (Axon, 1999). In the report the model was described as follows:

"The wheel, essentially a solid disc with 0.014m chamfered edges, had a diameter, D, of 0.5m and an aspect ratio, AR, of 30%. The shroud represented a single wheelhouse cavity and consisted of a wooden box with external dimensions 0.685m long by 0.275m wide. The wall thickness was 0.0125m. The depth of 0.325m at the front increased to 0.425m at the rear. The wheelhouse cavity was open on the underside and there was a part circular opening on one side with a radius of 0.3m. Adding the semi-elliptical front fairing and the tapering tail section increased the length of the model to 1.285m. A faired top section, with a 0.05m edge radius, was also added to give an overall shroud height of 0.475m. The wheel and shroud geometries were designed to give an acceptable wheelhouse size without high wind tunnel blockage. CAD plots of the validation model are shown in Figure 3.1".

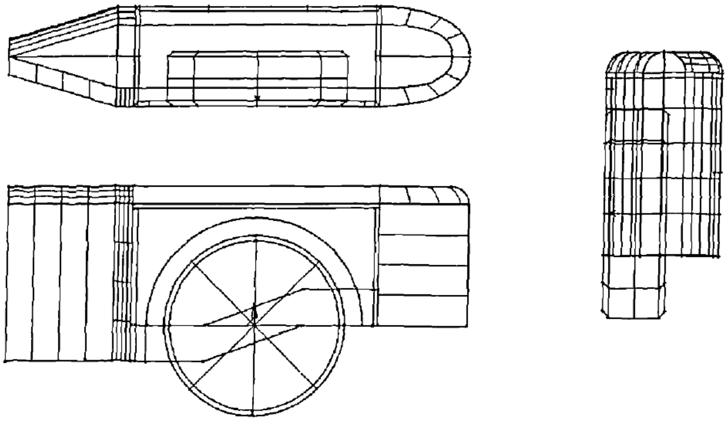

Figure 3.1: CAD drawings of model used in validation study (Axon, 1999)

The experimental setup was recreated into a CFD model, consisting out of the simplified wheelhouse model and the test section of the wind tunnel. The dimensions of the test section of the MIRA Model Wind Tunnel were as follows: 1.029m high, 2.057m wide and 4m long (Ahmad et al., 2009). The inlet of the test section was modelled with a 25m/s velocity inlet condition. The velocity inlet was placed at a distance of five times the length of the validation model upstream. The outlet of the test section was modelled with a pressure outlet condition. Since the validation study aimed to recreate the experiments as closely as possible, the walls were set to a no-slip condition. The floor of the wind tunnel was moving with a 25m/s velocity.

Wheel rotation can be modelled in several ways: rotating wall, Multiple Reference Frame (MRF) or a Sliding Mesh. It was concluded in the literature, based on flow fields only, that the sliding mesh approach showed the best agreement with experimental data, with an increase in computation time in the order of 15-20% (Söderblom et al., 2012). It was also shown in the report that the flow field is very sensitive to the choice of MRF region and that the domain should therefore be considered. It was shown that in most studies wheel rotation is modelled with a specification of velocity on the wall, resulting in an adequate approximation of wheel rotation (McManus and Zhang, 2006). Following the literature, it was chosen to model the wheel rotation with a specification of velocity on the wall.

3.2 Mesh settings

This section presents the different methods which were considered to generate the volume mesh. The focus was on the choice of cells, the approaches to modelling the behaviour of the near wall flow and the position of mesh refinements to capture the dominant phenomena.

3.2.1 Types of meshes

In STAR-CCM+ v7.06 three types of cells can be used to generate a volume mesh: polyhedral, tetrahedral and hexahedral cells. Tetrahedral and polyhedral meshes are best advised for rotating flows, or for flows where the main direction(s) cannot be aligned with an orthogonal set of faces. A comparison of polyhedral and tetrahedral cells yields that the polyhedral cells, for the same accuracy, require less cells and computation time. On the other hand, polyhedral cells are computationally more expensive. It is generally advised, unless resources are limited, to favour polyhedral cells over tetrahedral cells (CD-adapco, 2013; Peric and Ferguson, 2005).

It is known that hexahedral cells perform well if the flow direction is normal to the faces of the mesh; this is best suited for the modelling of freestream flow, where the faces of the cells can be aligned with the main direction of the flow. Since the polyhedral cells have more neighbours, they require more storage and are therefore more expensive than hexahedral cells (CD-adapco, 2013).

Considering that the domain for the validation model (and full-scale truck model) is rectangular, the main direction of the flow is known and computing power is limited, the volume was meshed using hexahedral cells.

3.2.2 Wall modelling

This section briefly discusses the approach to wall modelling. The solver shows a different behaviour depending on the size of the cells adjacent to the body. The dimensionless y^+ variable determines whether the flow near the wall was computed or modelled.

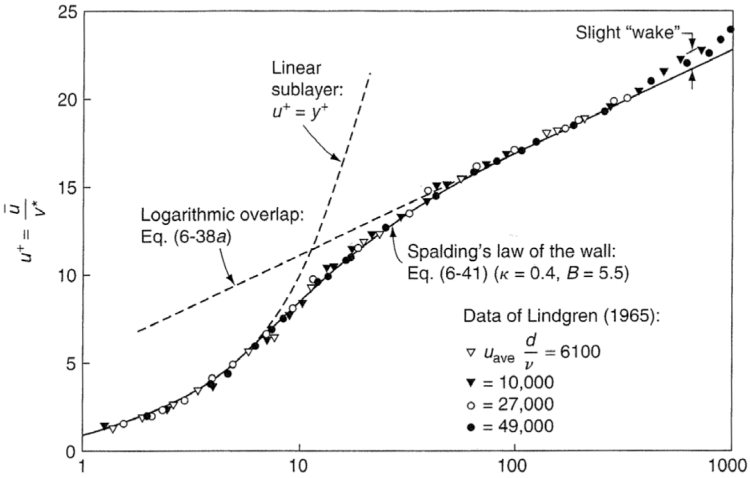

Figure 3.2: Behaviour of the boundary layer in the vicinity of the wall (White, 2006)

Figure 3.2 shows the behaviour of the velocity as function of distance from the wall for a flat plate flow. The velocity profile is expressed in non-dimensionalised wall coordinates $u^+ = \frac{\overline{u}}{v^*}$ and $y^+ = \frac{yv^*}{\nu}$ (White, 2006). The velocity profile shows different behaviours in the inner regions ($y^+ \lesssim 5$) and in the outer regions ($y^+ \gtrsim 30$). This has an effect on the modelling of the flow in the near wall region.

If the distance (y) from the first cell results in a y^+ value larger than 30, the solver automatically models the flow in the first cell according the logarithmic trend shown in Figure 3.2. If the y^+ reaches values smaller than 5 the flow in the first cell is computed, according to the linear relation between y^+ and u^+. It is postulated that computing the viscous regime improves the accuracy of the solution (CD-adapco, 2013). The region between $5 < y^+ < 30$, as observed in Figure 3.2, should be avoided since both methods do not yield a correct representation of the flow. Furthermore, it must be noted that this applies to the first cell only. It is generally advised, if the viscous layer is resolved, to have y^+ at approximately 1 (CD-adapco, 2013).

To ensure that the cells in the boundary layer are aligned with the flow, wall prism layers were added. These layers provide an overlap region between the wall and the freestream, while providing cells that are in alignment with the direction of the body and thus boundary layer. The difference between the prism layers for the $y^+ = 1$ and $y^+ = 30$ condition is presented in Figure 3.3. The prism layers have the same growth rate and should result in roughly the same amount of cells. It shows that the size of the total prism layer for $y^+ = 1$ is much smaller. Of course, to model the viscous regime small cells near the wall are required. In the $y^+ = 30$ case, the thickness of the prism layer becomes larger than the size of the cells in the refinement volume. Since most of the flow follows the rotation of the tyre it is important to align the cells with the flow as much as possible. It is therefore not bad to have cells that are slightly larger than specified in the refinement volume.

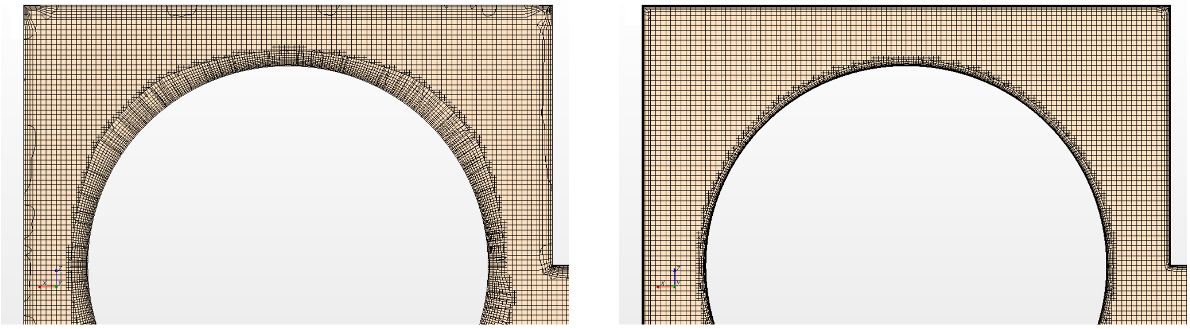
(a) (b)

Figure 3.3: Difference in prism layer, in the centreline of the wheel, between $y^+ = 30$ (Figure 3.3(a)) and $y^+ = 1$ (Figure 3.3(b)).

3.2.3 Mesh refinements

The literature review presented the position of the most dominant phenomena in the flow near wheelhouses and isolated wheels. Refinement volumes were added to capture these

Table 3.1: Overview of refinement volumes

Volume	Cell size (mm)	Cell size (%)
Baseline	0.064	100
Refinement 1	0.032	50
Refinement 2	0.016	25
Refinement 3	0.008	12.5
Refinement 4	0.004	6.25
Refinement 5	0.002	3.125

phenomena. This section presents the positioning of these refinement volumes.

Since the main direction of the flow in the wheelhouse is parallel to the wheel it was chosen to include a large prism layer. This ensures that the direction of the cells is in alignment with the main direction of the flow. Figures 3.4 and 3.5 present the positioning of the refinement volumes. It shows the mesh in the freestream (1) and in the far wake (2). Refinement volume (3) was added to capture the flow inside of the wheelhouse and in the near wake. Refinement volume (4) was added to capture the formation of the CVP and refinement volume (5) was added to capture the jetting. Table 3.1 presents an overview of the refinement volumes and the base length of the cells. The smallest cells in the validation study can be found in refinement volume (5), near the contact patch, to capture the jetting.

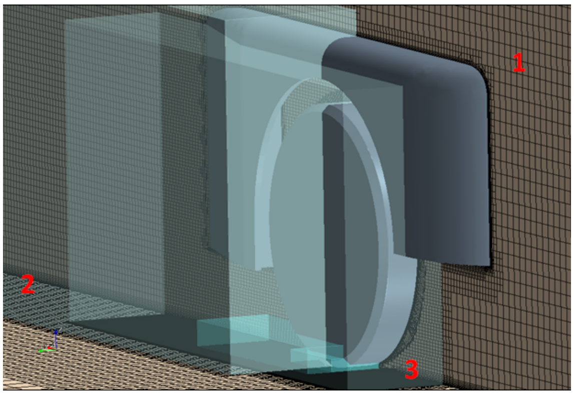

Figure 3.4: Positioning of refinement volumes

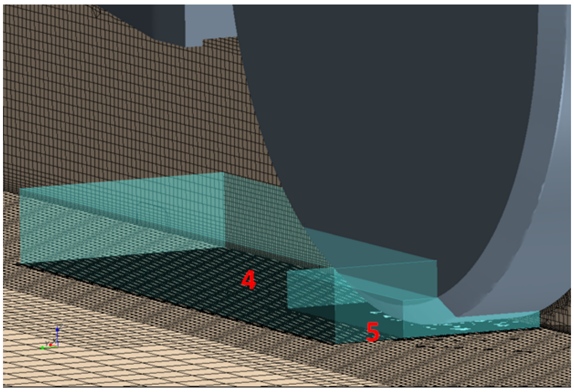

Figure 3.5: Close up of refinement volumes surrounding the contact patch of the wheel

3.3 Mesh sensitivity study

The goal of this section is to present an overview of the mesh refinement study that was performed. The mesh refinement study was performed to refine the mesh up until the point there is little change in the solution (i.e. C_D, $C_{p,tot}$ hardly change). Initially the mesh was refined by decreasing the base length of cells in fixed steps. This approach also refined the cells far away from the body, which is inefficient since they hardly have an influence on the solution. Therefore a hybrid (restructured) approach was introduced, where the cells in the vicinity of the body were refined and cells far from the body were kept at baseline levels.

3.3.1 Approach

The turbulence model chosen for this study is $k-\omega$ SST, as was recommended in the literature for the flow in isolated wheelhouses (Régert and Lajos, 2007). For this turbulence model it was advised to compute the viscous regime (Axerio-Cilies, 2012). In this particular section transition was modelled, accidentally, with the $\gamma - Re\theta$ model. This should be taken into account when analysing the results. This first stage of the mesh refinement study was crude, since all cells in the domain were evenly affected.

The baseline mesh of the validation model, presented in the previous section, was labelled M_1. Mesh M_2 indicates a refinement with the aim to increase the total number of cells in the volume by a factor of 2, i.e. a base length decrease of $\sqrt[3]{2} = 1.25$. The mesh refinements went up to M_{16}, each time doubling the total number of cells in the volume.

To have a comparison where only the influence of the mesh is considered, the near wall behaviour of the flow was treated equally for all simulations, i.e. roughly the same y^+ conditions apply. Since the y^+ value is dependent on the velocity in the boundary layer, small differences were expected, but it was seen that the values remained in the same order of magnitude.

3.3.2 Results

Although the simulations were done steady state, fluctuations can be found in the solution as a function of the iteration number. Figure 3.6 shows the drag coefficient of the wheel and wheelhouse separately, following the convention in the literature (Axon, 1999). It was seen though, that the total drag coefficient also fluctuated. Therefore instantaneous values should be approached with caution, especially when flow fields are compared. A better approach is to create mean velocity and pressure fields, by averaging the variables over a large number of iterations. Figure 3.6 shows that the last 500 iterations span at least two fluctuation cycles in drag coefficient. It was judged that averaging over this span removed the periodic influences from the flow eliminating the dependence on the outcome of the last iteration.

Figure 3.7 presents the effect of mesh refinement, plotted on a logarithmic scale. A converging trend can be identified clearly from mesh M_1 to M_4, indicating that the baseline mesh of the validation model was not mesh independent. Since the drag coefficient of mesh M_8 showed a small increase with respect to mesh M_4 it was argued whether mesh M_8 was the mesh independent solution. The result of mesh M_{16} shows that the drag coefficient is at the same level of M_4, and it was thought that the slight increase in drag coefficient of mesh M_8 was due to the refinement in the wake of the model. The trailing edge of the validation model was sharp and thus sensitive to the changing mesh.

Figures 3.8(a) to 3.8(h) present the total pressure coefficient and vorticity fields for meshes M_1

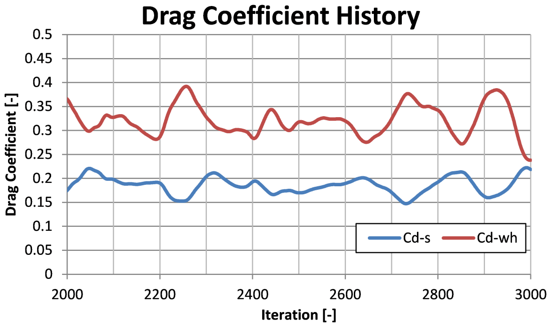

Figure 3.6: Drag coefficient per iteration, for mesh M_8

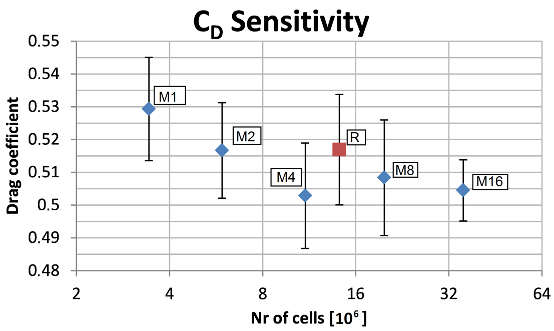

Figure 3.7: Drag coefficient as a result of mesh refinement

and M_{16}. It can be seen that there is no significant difference in the formation of the jetting and the development of the vortex downstream. The changes in position and strength of the jetting vortex were minimal. A small change in vorticity was observed between Figures 3.8(a) and 3.8(b) in the region of the jetting, but since the drag coefficient decrease was minimal, it led to believe the near wheel behaviour was mesh independent. This was also concluded in the literature (Régert and Lajos, 2007). Therefore, mesh M_8 was considered to be the mesh independent mesh.

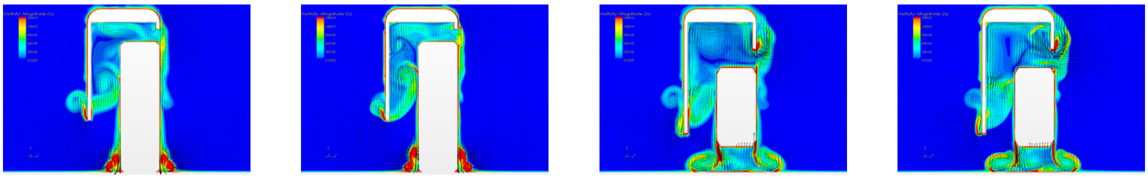

(a) Vorticity magnitude, mesh M_1, X = 0m

(b) Vorticity magnitude, mesh M_{16}, X = 0m

(c) Vorticity magnitude, mesh M_1, X = 0.3m

(d) Vorticity magnitude, mesh M_{16}, X = 0.3m

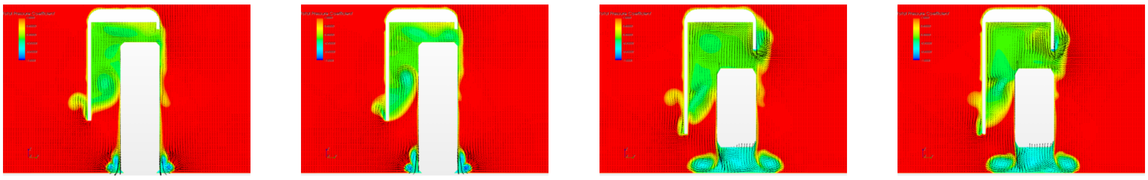

(e) Total pressure coefficient, mesh M_1, X = 0m

(f) Total pressure coefficient, mesh M_{16}, X = 0m

(g) Total pressure coefficient, mesh M_1, X = 0.3m

(h) Total pressure coefficient, mesh M_{16}, X = 0.3m

Figure 3.8: Behaviour of the flow as a result of mesh refinement

3.3.3 Mesh restructuring

It was already discussed in the previous section that decreasing the base length of all cells is not the most efficient way of refining. Therefore a restructured mesh was introduced that had cells near the surface at levels of mesh M_8 and kept cells in the freestream at levels of M_1.

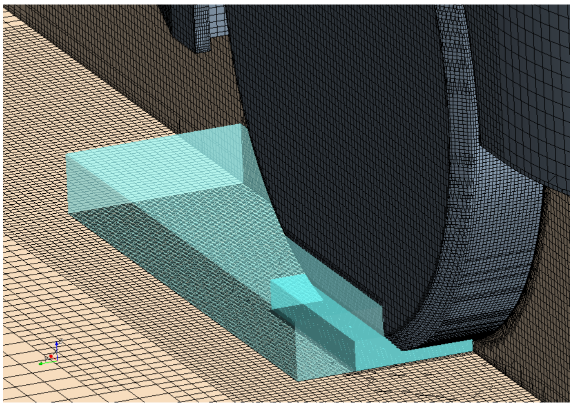

Figure 3.9: Refinement volumes near the contact patch of the validation model

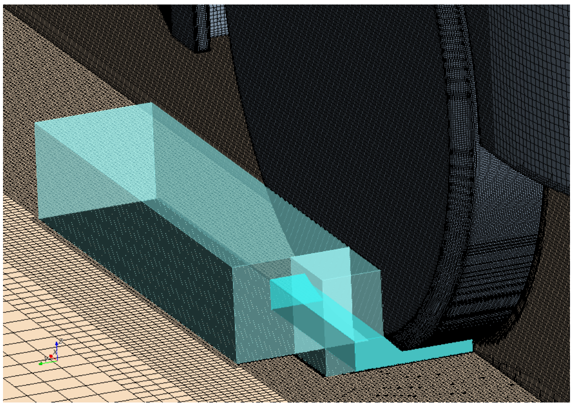

Figure 3.10: Refinement volumes near the contact patch of the restructured mesh

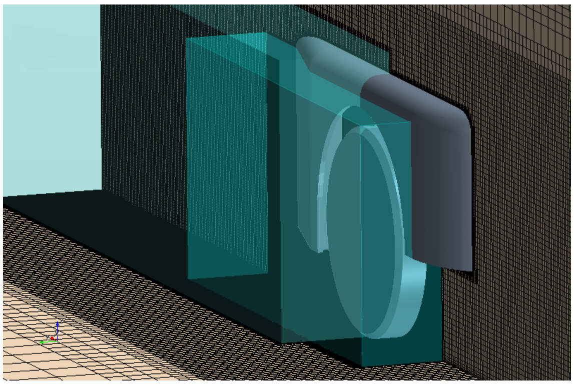

Figure 3.11: Positioning of baseline refinement volumes in the wake

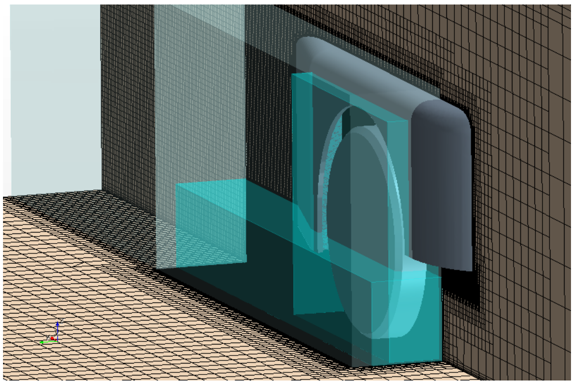

Figure 3.12: Positioning of the restructured refinement volumes in the wake

This approach resulted in a 30% decrease in cells in the volume. Figures 3.9 and 3.11 present the volume refinements for the baseline mesh and Figures 3.10 and 3.12 present them for the restructured mesh. It shows that the cells of the restructured mesh were twice as large in the regions close to the body. It was also observed that small changes in the refinement volume that captured the CVP were made. No significant changes in the position of the dominating phenomena were found, as was also demonstrated in the previous section.

Figure 3.7, however, does show an increase in drag coefficient. It was already suggested that this increase is due to the sensitivity of the drag coefficient to the refinement of the wake. It was seen that the cells in the wake returned to baseline levels faster than in the mesh independent mesh. Furthermore, it will be demonstrated in the next section that the drag coefficient of restructured meshes, with other turbulence models, show a close agreement with their respective mesh independent grids.

3.3.4 Summary of mesh settings

It was shown that for open road conditions hexahedral cells were best suited to generate the volume mesh, since they were less expensive than polyhedral cells and the faces could be aligned with the main direction of the flow. The baseline mesh near the validation model and its wake consisted out of 64mm cells. Furthermore, mesh refinements were added to capture the dominating phenomena. Near the contact patch 1mm cells were added to capture the jetting. A large refinement volume with 2mm cells was added for $Z/D < 0.25$ to capture the CVP. The mesh in the wheelhouse and near wake consisted out of 8mm cells. A restructured approach resulted in a decrease of total cells of 30% compared to the mesh independent mesh. The cells near the body were kept at mesh independent levels, while in the freestream baseline values were applied. There was no decision in the wall modelling approach since that is dependent on the type of turbulence model.

3.4 Turbulence models

In this section the effects of different turbulence models on the simulation are discussed. The turbulence models tested are the common used models in the industry, namely: Realisable $k - \epsilon$ and $k - \omega$ SST models. Furthermore, for computational purposes the standard $k - \omega$ model was tested as well.

3.4.1 Description of turbulence models

The comparison of the turbulence models is done on identical meshes, except when the effects of y^+ conditions were investigated. The analysis in Section 3.2 was done with a transition model, which was selected by accident. It was seen that running the simulation without the transition model resulted in (almost) the same drag coefficient, with a decrease in computation time. For this reason, it was chosen to omit the transition model in future computations. The analysis in this section was done using averaged variables, as discussed in the previous section.

The current study considered the following turbulence models. A summary of the settings used per turbulence model is presented in Table 3.2:

- Realisable $k - \epsilon$
    - Two equation model, wall function approach.
    - Most applied in automotive industry since it is stable and fast converging, due to the increase in dissipation. Although it is known that there is less agreement with

flow structure, the prediction of the forces is acceptable (Söderblom et al., 2009; Régert and Lajos, 2007).

- Standard $k-\omega$
  - Two equation model, wall function approach.
  - Sensitive to inlet conditions and considered to be better in flows with adverse pressure gradients (Régert and Lajos, 2007; CD-adapco, 2013)
- $k-\omega$ SST
  - Two equation model, both wall function and computation of boundary layer
  - Mixture of $k-\omega$ in the near wall and $k-\epsilon$ in the far field. This keeps the advantageous properties in adverse pressure gradients, but eliminates sensitivities to inlet conditions (CD-adapco, 2013).
  - As discussed, further $k-\omega$ SST models were without transition modelling.

The following turbulence models were also considered, but not chosen:

- Reynolds stress models: this turbulence model solves 7 equations per iteration and was judged to be computationally too expensive. It was further seen that using the full Reynolds stress model does not yield a significant change in the qualitative structure of the flow field (Régert and Lajos, 2007)
- Spallart-Allmaras: this one equation turbulence model is known for its fast and stable behaviour, but is known for having troubles with massively separated regions (Bakker, 2005). Therefore it was not considered in this study.

Table 3.2: Overview of simulations performed to investigate the turbulence settings

Simulation name	Mesh	Turbulence model	y^+	Cells (10^6)
$k-\epsilon$	Mesh M_8	$k-\epsilon$	$30 < y^+ < 100$	16
$k-\epsilon$ OPT	Restructured	$k-\epsilon$	$30 < y^+ < 100$	11
$k-\omega$	Mesh M_8	$k-\omega$	$30 < y^+ < 100$	16
$k-\omega$ OPT	Restructured	$k-\omega$	$30 < y^+ < 100$	11
$k-\omega$ SST_{30}	Mesh M_8	$k-\omega$ SST	$30 < y^+ < 100$	16
$k-\omega$ SST_{30} OPT	Restructured	$k-\omega$ SST	$30 < y^+ < 100$	11
$k-\omega$ SST_1	Mesh M_8	$k-\omega$ SST	1	20
$k-\omega$ SST_1 OPT	Restructured	$k-\omega$ SST	1	16

3.4.2 Results

The outcome of the simulations with different turbulence models was subjected to a series of tests to determine which turbulence model shows the best agreement with experimental values.

At the end a trade-off will be performed. Two quantitative variables were used to compare the simulations with the experiments, i.e. drag coefficient and pressure coefficient distribution in the wheelhouse. Since no experimental data was available about the distribution of vortices in the validation model, it was decided to compare it to CFD results on similar geometries. This was done by computing isosurfaces of Q-criterion and total pressure.

Drag Coefficient

Figure 3.13 presents the drag coefficients computed with the different turbulence models, with respect to the experimental drag coefficient. The conditions of the mesh were the same for all simulations, except for SST_1 and SST_1 OPT which had a wall refinement to satisfy $y^+ = 1$ conditions.

It can be seen that the $k - \epsilon$ model underpredicts the drag coefficient by more than 10% and shows a small spread in data. Furthermore, it can be noticed that the $k - \omega$ SST_1 model results in an overprediction of the drag coefficient by more than 10%. Although it was advised to have y^+ conditions in the order of 1 (Axerio-Cilies et al., 2012) it did not improve the estimate of drag coefficient. It was thought that viscous regime was computed well in the first cell (hence $y^+ = 1$ conditions), but that the size of the succeeding cells grew too fast to accurately model the boundary layer flow.

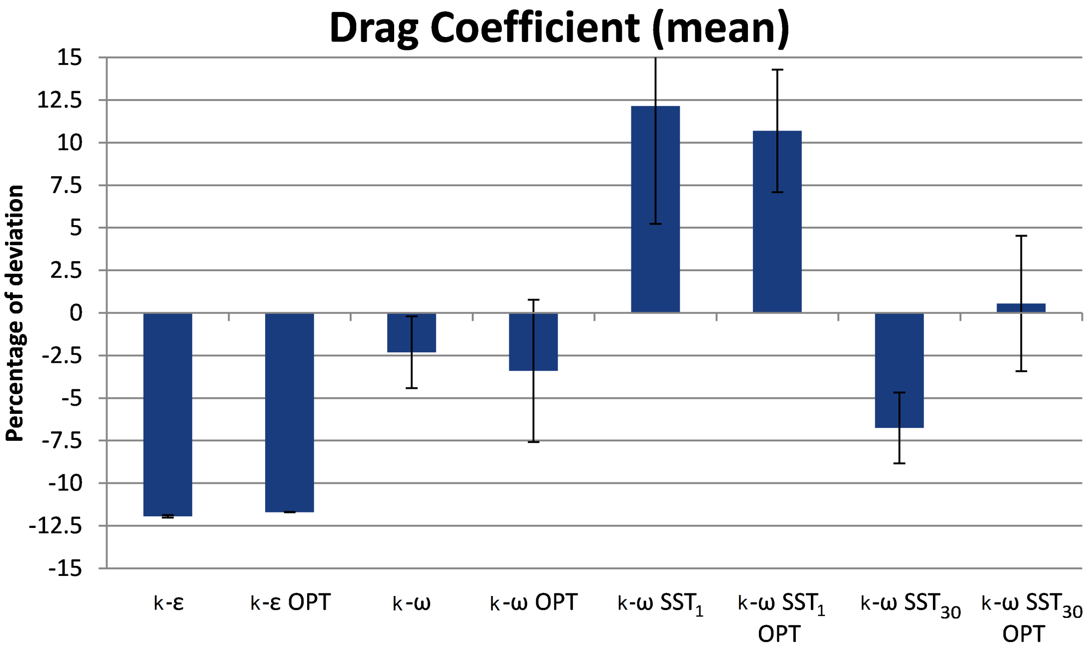

Figure 3.13: Drag coefficients for difference turbulence model settings, compared to experimental data (Axon, 1999)

Figure 3.13 also shows that restructuring the mesh depends on the turbulence model. In case of the $k - \epsilon$ model there is a good agreement between the original and the restructured mesh. The $k - \omega$ and $k - \omega$ SST_1 models show a difference in drag coefficient between the original and restructured mesh, but within 1% of each other. The difference between the $k - \omega$

SST_{30} models was called significant. This shows that for each turbulence model a separate mesh independence study should be performed. However, since $k-\omega$ SST_{30} OPT shows the closest agreement with the experimental drag coefficient and the effect of restructuring with the other turbulence models showed a good behaviour, the restructured mesh was trusted in this case.

Pressure coefficient contours

This section presents a quantitative comparison between the numerical results and experimental data. Since the experimental data is available in tabular form, along the centreline of the wheel only, the analysis of the distribution of pressure coefficient on the inner faces of the wheelhouses will be quantitative. The qualitative comparison of pressure distributions in the centreline is presented in the next section.

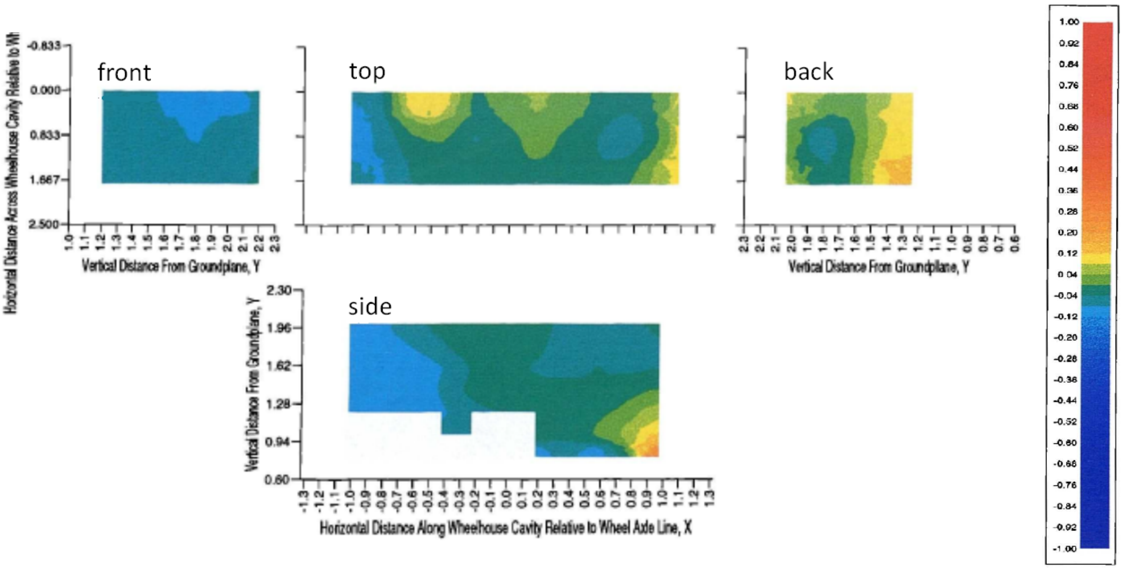

Figure 3.14: Experimental pressure coefficient distribution on the inner surface of the wheelhouse (Axon, 1999)

Figure 3.14 presents the experimental distribution of pressure coefficient in the wheelhouse, obtained by extrapolating measured data. For accuracy reasons, the data was not extrapolated onto the boundaries (Axon, 1999). This data was reconstructed with the simulations, of which the best agreement is shown in Figure 3.15 and the rest is presented in Appendix B.

From Figure 3.15 it can be seen that the position of the first peak on the top surface agrees reasonably, and also a second peak (although not at the exact same position) is visible. It can also be observed that most turbulence models (except $k-\epsilon$) overpredict the magnitude of the pressure peak. Figure 3.17 illustrates how the pressure peak is created by the separated flow stagnating on the top surface of the wheelhouse. It can be concluded that the difference in magnitude and location of the stagnation is a direct result of the different predictions of separation.

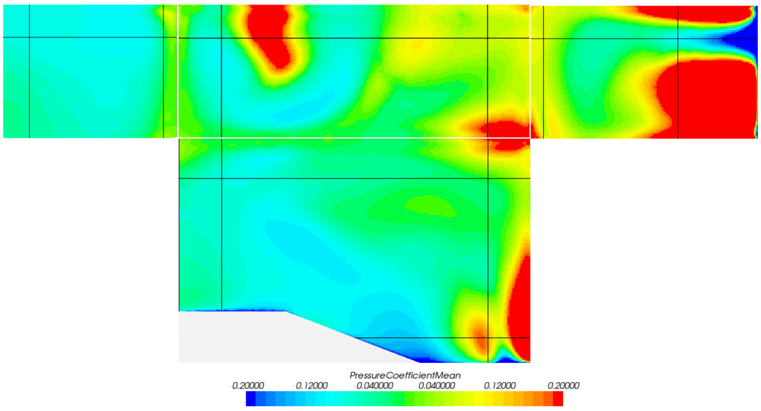

Figure 3.15: Computed pressure coefficient distribution on the inner surface of the wheelhouse, $k-\omega\ SST_{30}$, mesh OPT. Note, black lines correspond to the boundaries seen in Figure 3.14

All turbulence models were able to predict the behaviour of the pressure coefficient on the front and side surfaces of the wheelhouse correctly. The experiments showed a negative pressure region on the back surface, which is predicted by SST_{30} OPT and SST_1 only. The region behind the rotating wheel is a region dominated by separated flow. It was observed that flow is entrained into the wheelhouse by the rotation of the wheel, but air also tries to flow out of the wheelhouse through the same region (Régert and Lajos, 2007). It is difficult to accurately predict the mean behaviour of the flow in this region (Axon, 1999). Therefore, turbulence models that predict a negative pressure on the back surface were judged to be in agreement with the experiments.

Pressure coefficient graphs

This section presents the pressure coefficient distribution on the inner surface of the wheelhouse. The measurement points are positioned along the plane through the centreline of the wheel that intersects with the inner surface of the wheelhouse, see Figure 3.16.

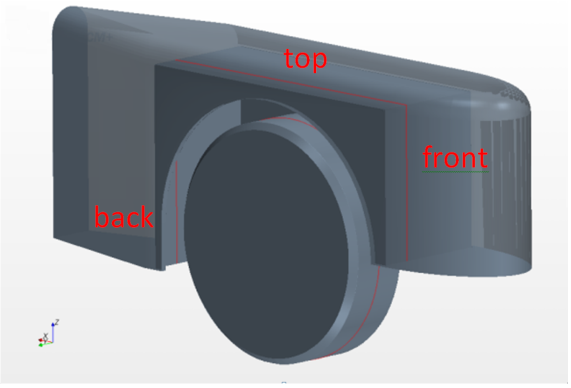

Figure 3.16: Measurement planes of the pressure coefficient distribution in the centreline of the wheel

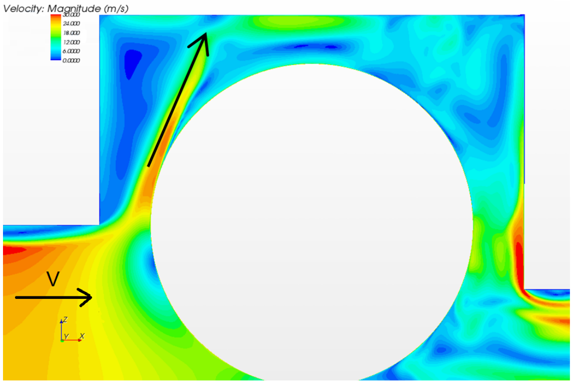

Figure 3.17: Illustration of flow separation on front wheel and stagnating on the top surface of the wheelhouse

Figure 3.18 presents the pressure coefficient distribution on the front face of the inner wheelhouse. It can be seen that the behaviours of the $k - \epsilon$ and $k - \epsilon$ OPT curves are almost identical. It was already noted that the drag coefficient of the restructured mesh was close to the non-restructured mesh. Observing that the pressure coefficient distributions are (almost) identical verifies that the $k - \epsilon$ turbulence model shows a mesh independent behaviour.

At the top of the front surface three turbulence cases ($k - \epsilon$, $k - \epsilon$ OPT and $k - \omega$ SST_1 OPT) show a different behaviour and appear to be missing the rise in pressure at Z $>$ 0.55m. Due to the lack of experimental data near the boundary, it can be argued whether the three different turbulence models show the correct behaviour. It was also observed that the $k - \omega$ SST_{30} model underpredicts the pressure coefficient in the lower region and that the $k - \omega$ model shows fluctuations between the measurement points that were not observed in Figure 3.14. All other turbulence models agree reasonably with the experimental values.

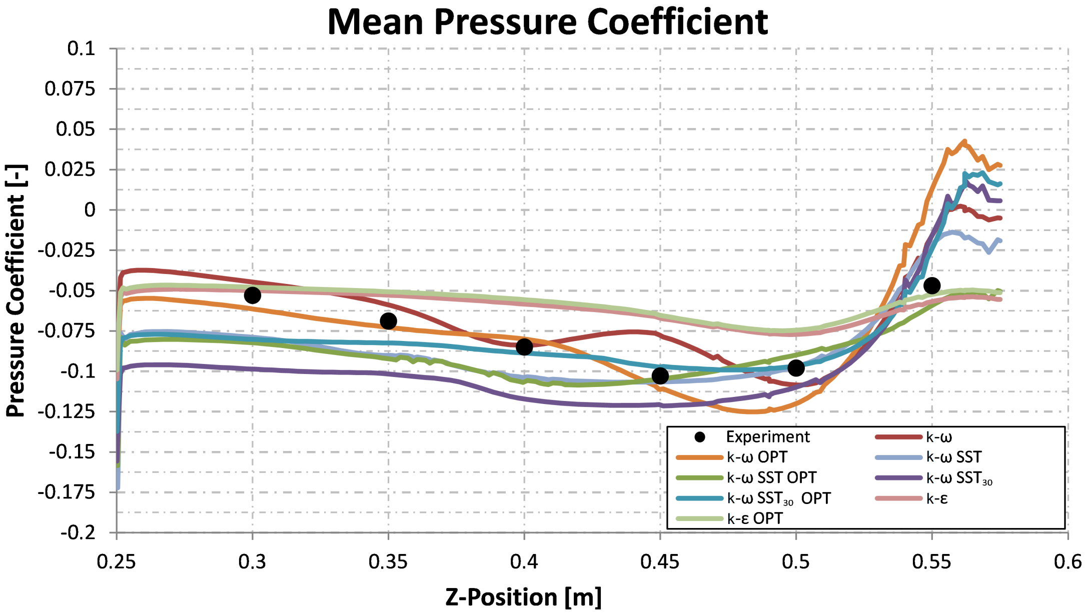

Figure 3.18: Pressure coefficient distribution on front surface of wheelhouse

Figure 3.19 presents the distribution of pressure coefficient on the top surface of the inner wheelhouse. The pressure coefficient distribution is heavily influenced by the separation of flow from the tyre, as discussed in the previous section.

Figure 3.14 shows that the location of the pressure peak is between 0.35 $<$ X/R $<$ 0.65; or in the coordinates of Figure 3.19: -0.16m $<$ X $<$ -0.08m. Figure 3.14 shows, when observed more closely, that there is no clear peak, but an area of increased pressure. Figure 3.19 shows that the pressure peak predicted by the $k - \epsilon$ models shows good agreement, but also shows that the location of separation was completely mispredicted.

The standard $k - \omega$ shows the best agreement with the experiments by predicting the smallest pressure peak and correct location. The prediction of the peak for $k - \omega$ SST also shows a good agreement, although it predicts the location of the peak (and thus separation of the wheel) too early. The SST_{30} models underpredict the separation point of the tyre. The SST_1 and standard $k-\omega$ already better predict the location of separation.

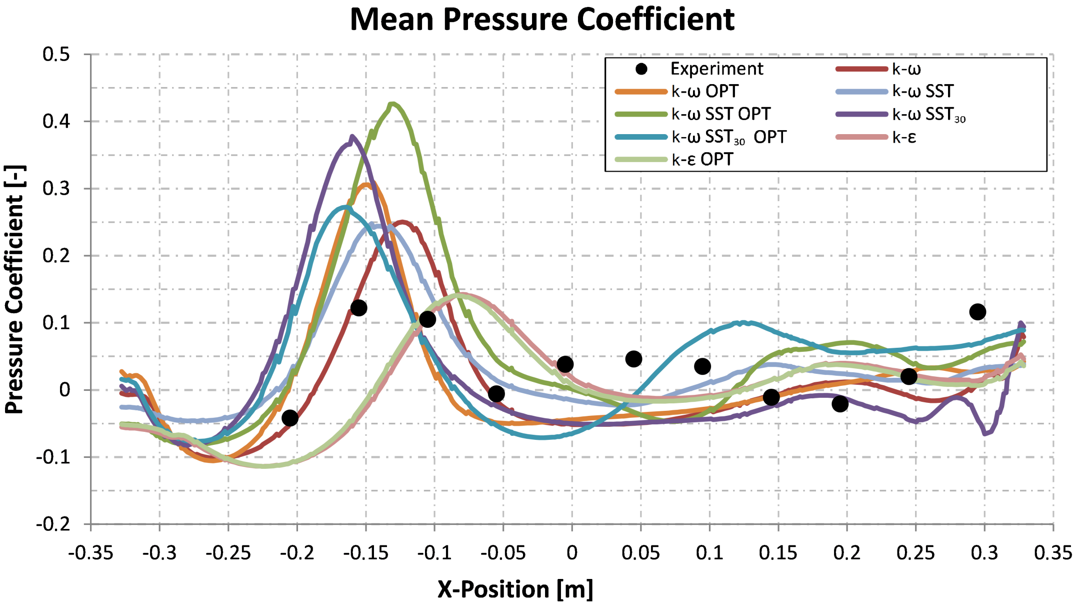

Figure 3.19: Pressure coefficient distribution on top surface of wheelhouse

All turbulence models miss the second, smaller, pressure peak located just above the wheel, between 0m < X < 0.1m. Some of the turbulence models are able to predict some sort of second pressure peak at an aft location, but none showed a reasonable agreement with experiments. The increase in pressure behind the wheel (X > 0.25m) is missed by all the turbulence models.

Finally, Figure 3.20 presents the pressure coefficient distribution on the back face of the wheelhouse. Figure 3.14 showed that in the region where the measurements were taken (Z/R > 1.25; or Z > 0.31m) the pressure coefficient remains positive. It can be seen that the $k-\epsilon$ models show adequate behaviour on the back of the wheelhouse and are the only models that keep the pressure coefficient larger than zero. The trend it predicts, on the other hand, does not agree with the experiments. The region behind the tyre is dominated by separated flow, which is the reason that $k-\epsilon$ predicts the mean behaviour of the flow reasonably well. Apart from $k-\epsilon$, the standard $k-\omega$ model is the only one that has some agreement with the experimental results, i.e. the only model that picks up on the rise in pressure in the region below Z = 0.3m.

Figure 3.15 showed that the line where pressure coefficient is measured (black horizontal line), negative pressure dominates. This patch was predicted in the experiments as well, but not in the centreline of the wheel. This is the cause for the large underprediction of all the turbulence models and it was questioned whether the results from the experiments are correct. Therefore, the results of the pressure coefficient on the back surface of the wheelhouse are considered, but the quantitative analysis in the previous section was better trusted.

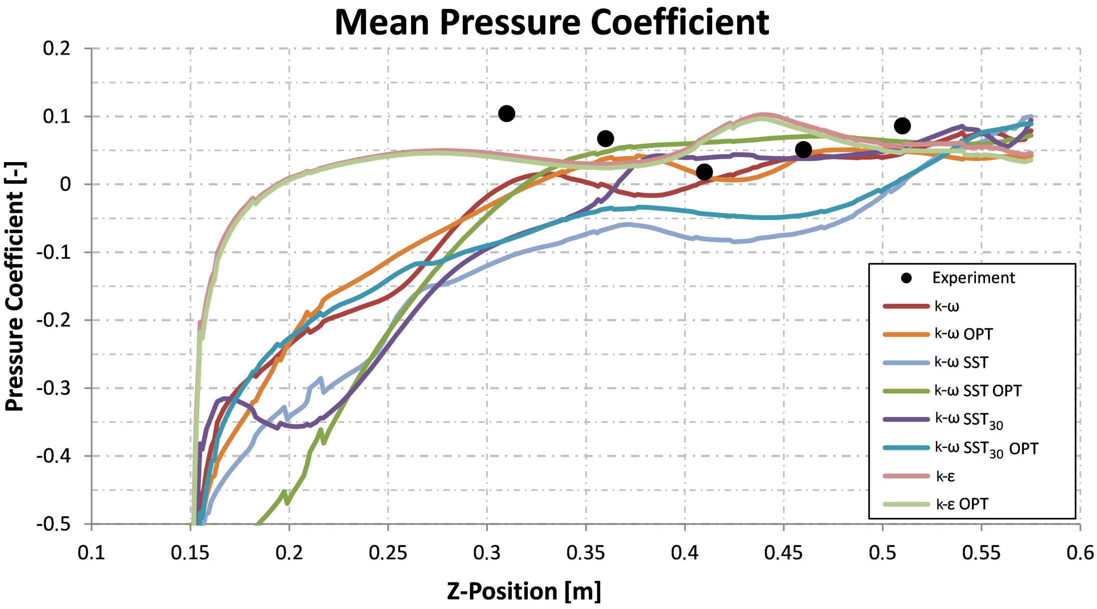

Figure 3.20: Pressure coefficient distribution on back surface of wheelhouse

Isosurfaces of Q and p_{tot}

To identify the position of vortex cores and separated regions, isosurfaces of Q-criterion and total pressure were computed. Since (Axon, 1999) did not report on the dominant phenomena in the wheelhouse, the results were compared with other computations by (Régert and Lajos, 2007). There is a slight difference in geometry, so differences in the position and strength of the vortices were anticipated. However, it was also suggested that the presence of the dominant phenomena was independent of geometry (Régert and Lajos, 2007). This allowed for a qualitative comparison of the phenomena in the flow field with the literature.

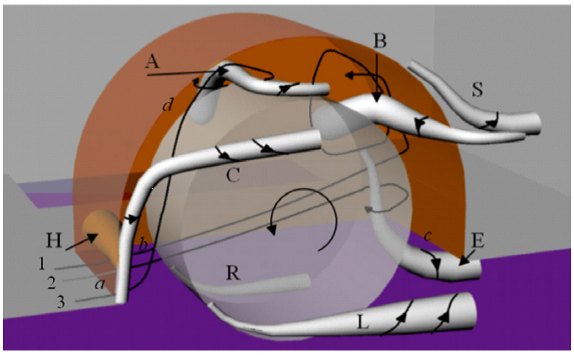

Figure 3.21: Sketch of position of most dominant vortices (Régert and Lajos, 2007)

Figure 3.21 presents the vortex structures found in the literature, which were constructed using a combination of vortex identification methods, such as total pressure coefficient, the Q-criterion and a vortex skeleton method (Régert and Lajos, 2007). They observed that the Q-criterion method visualised the presence of vortices best in high-velocity areas only, i.e. vortices H, L, R, C and E. The isosurfaces of zero total pressure were found to be better suited for visualising lower energy (separated) flows, i.e. vortices A, B and S. It was also demonstrated that the isosurfaces of Q-criterion cannot visualise low velocity phenomena, such as vortices A and B (Régert and Lajos, 2007).

Figures 3.22 and 3.23 present isosurfaces of Q-criterion and total pressure, respectively, for the $k-\omega$ SST_{30} model. The results from the simulations with the other turbulence models are presented in Appendix B. In the previous chapter it was seen that the pressure distribution of the SST_{30} turbulence model showed a good agreement with the literature. It was seen that all turbulence models predicted the position of vortices H, L, R and (in lesser extent) E with the isosurfaces of Q-criterion and A, B and S with the isosurfaces of total pressure. The presence of vortex C cannot be identified, or slightly, and it is questioned whether the formation of this vortex was affected by the different geometries. It was also shown that the isosurfaces of Q-criterion for $k-\epsilon$ model were less pronounced compared to all the $k-\omega$ models. Finally, the isosurfaces showed a difference between the outflow of $k-\omega$ and $k-\omega$ SST_{30}. Both models had an identical mesh and the SST formulation consists of the standard $k-\omega$ model near the wall. This shows that the changed far field formulation of the SST model had influence on the near wall flow behaviour.

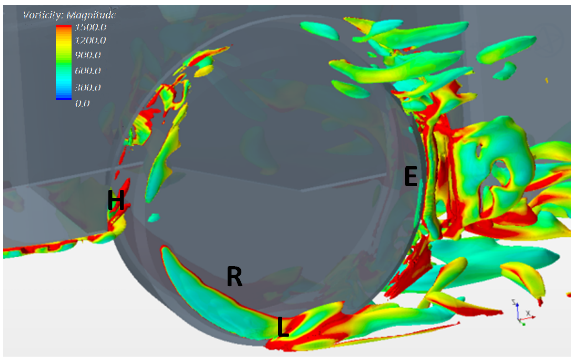

Figure 3.22: Isosurfaces of QD/U_∞ = 50000, SST_{30} OPT

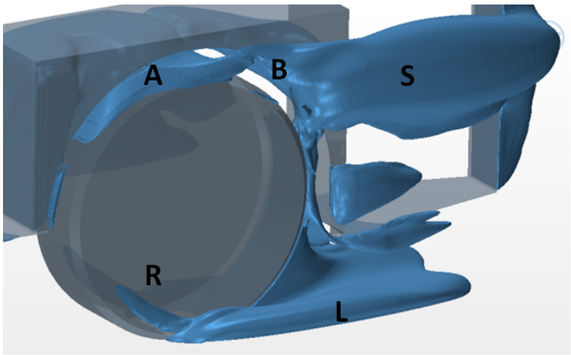

Figure 3.23: Isosurfaces of p_{tot} = 0, SST_{30} OPT

3.4.3 Trade off

Table 3.3 presents a summary of the criteria which were used to judge the performance of the turbulence models. The behaviour of the turbulence models has been discussed in the previous sections and the agreement with the experiments determines the performance of the turbulence model. It was seen that the $k-\epsilon$ underpredicted the drag coefficient and showed a poor agreement with the experimental pressure distribution. It was seen though that in regions dominated by separated flow (behind the wheel) the stability of the $k-\epsilon$ model predicted the mean behaviour better than the other turbulence models. In spite of this, its

Table 3.3: Turbulence model trade off table

	Pressure graph			**Pressure contours**	**Q/p_{tot} plots**	C_D
	top	front	back			
$k-\omega$ SST_{30}	0	-	0	0	0	0
$k-\omega$ SST_{30} OPT	0	+	-	+	0	++
$k-\omega$ SST_1	+	+	-	+	0	- -
$k-\omega$ SST_1 OPT	0	0	0	0	0	- -
$k-\epsilon$	-	-	+	0	-	- -
$k-\epsilon$ OPT	-	-	+	0	-	- -
$k-\omega$	+	+	0	0	0	+
$k-\omega$ OPT	0	0	0	0	0	+

Poor performance	- -
Weak performance	-
Reasonable performance	0
Good performance	+
Excellent performance	++

poor prediction of drag and pressure distribution made it unsuitable.

The results from the standard $k-\omega$ model showed good agreement with the results from the SST models. This was expected since the $k-\omega$ SST model uses the standard $k-\omega$ formulation near the wall. In terms of drag coefficient and pressure graphs the $k-\omega$ model showed good agreement with the experimental values. The drag coefficient computed by the SST_1 overpredicted the experimental value by more than 10%. The distribution of pressure on the inner surface showed a reasonable agreement with experiments though, but did not seem to distinct from the model with wall functions. It was argued that the cells in the near wall grew too fast to accurately model the boundary layer, making the model unsuitable.

Based on the excellent agreement of the drag coefficient, and general good agreement in terms of pressure graphs, the $k-\omega$ SST_{30} OPT model was judged to be the best model. The wall function approach saved in computation time when compared to fully resolving the boundary layer. Furthermore the results did not seem to be inferior to the results of the SST_1 models. Isosurfaces of Q-criterion and total pressure showed a good agreement with the literature, where it must be noted that most of the turbulence models predicted the dominating phenomena reasonably well. It must also be noted that $k-\omega$ SST_{30} is (minimally) computationally more expensive than the $k-\omega$ model, but this was justified by a more accurate prediction of drag coefficient.

3.5 Transient solvers

Due to the unsteady nature of the physics it can be argued whether using a steady state solver is the correct approach. It was shown in the previous section that the steady state

RANS solvers were able to predict the drag coefficient within a range of 10%, with the best prediction within 1%. This section demonstrates that an unsteady solver does not result in a better agreement with the experiments.

To start, a velocity field was initialized with a steady state run, using a $k-\epsilon$ turbulence model in order to achieve fast convergence. After convergence in drag coefficient was obtained (see Figure 3.24) the switch to the unsteady solver was made. This also came with a switch in turbulence model. To comply with the y^+ conditions small changes in the mesh were made, which is the reason for the negative peak in Figure 3.24.

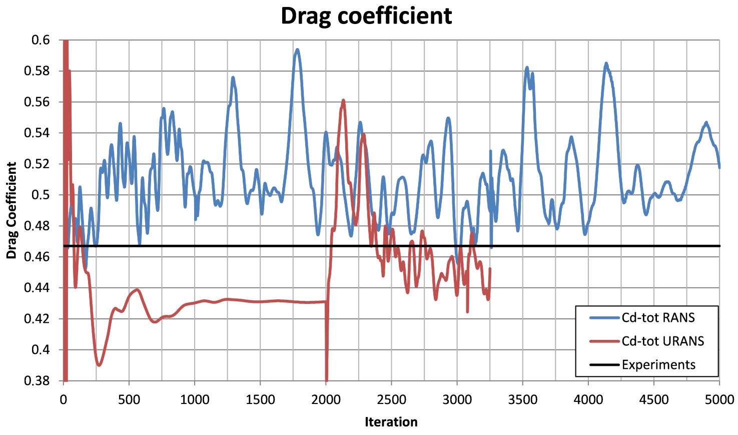

Figure 3.24: Comparison of drag coefficient of steady and unsteady simulations

Figure 3.24 presents the drag coefficient for the unsteady and steady runs. Note that after 2000 iterations the switch to the unsteady solver was made. As a result, the results are no longer a function of iteration, but of time step. The time step used in this exercise was 0.0004s, complying with the CFL conditions. The 1250 time steps observed in Figure 3.24 result in a total resolved flow of 0.5s. Figure 3.24 shows that the steady state resulted in an overprediction of the drag coefficient by 10% (as was already shown in the previous section). Figure 3.24 also shows that the steady state $k-\epsilon$ turbulence model resulted in fast convergence (underpredicting drag coefficient by 10% though). After the switch to the unsteady solver it showed that the mean drag coefficient of the last 500 timesteps underpredicted the experiments by approximately 5%.

This illustrates that an unsteady RANS simulation does not necessarily result in a better prediction of the flow. It is known that unsteady RANS models compute the unsteady phenomena in the mean flow, but still model the eddies in the turbulence to some respect. Furthermore, it was postulated that unsteady RANS models were best suited when the unsteadiness is deterministic, which is not the case in this thesis. This means that unsteady RANS models do not result in a better prediction of drag coefficient (Iaccarino et al., 2003).

3.6 Summary

The goal of the validation study was to find settings that showed good agreement with the experimental results and obtain reliable model settings. A mesh sensitivity study was performed to find the influence of mesh refining on the solution. An independent mesh, of approximately 16 million cells, was found after refining the baseline mesh of the validation model. This was done inefficiently, however, by equally refining all the cells in the domain. If the refinement was applied close to the surface only, a reduction in cells of 30% was obtained.

Furthermore, a turbulence model study was performed. It was found that the Realisable $k - \epsilon$ model did not show a good agreement with the experiments. The $k - \epsilon$ model had difficulty dealing with flow dominated by separation and rotation. As a result, the drag coefficient and pressures on the inner wheelhouse were underpredicted. The standard $k-\omega$ also showed reasonable agreement with the experiments, but underpredicted the drag coefficient. Furthermore, it was seen that it did not always predicted the pressure in the wheelhouse correctly.

It was seen that the $k - \omega$ SST with $y^+ = 1$ conditions overpredicted the drag coefficient, but showed a reasonable behaviour in terms of pressure distribution on the inner faces of the wheelhouse. The $k - \omega$ SST model, with wall functions, did not underperform from resolving the boundary layer and even resulted in a more accurate prediction of drag coefficient. This method was also found to be computationally less expensive. The computation time of the SST model was (marginally) more than for the standard $k - \omega$ model, but is justified by the better agreement with the experiments.

It was also shown that unsteady RANS simulations did not provide a better prediction of the drag coefficient compared to the steady state simulations. This is likely due to the fact that the unsteady RANS model both resolved and modelled the turbulent eddies and best performs when the unsteadiness is deterministic. Since URANS is computationally more expensive and did not result in a better prediction of the flow, it was chosen to continue with the steady state solver.

Chapter 4

Baseline truck model

The previous chapter presented model settings that were validated through comparison with experimental values. These model settings will be applied to the baseline truck model. Due to the extra detail in the baseline truck model, the mesh settings from the validation studies serve only as a guideline. With the correct model settings different variants will be constructed with the intention understanding the sensitivity of the flow to changes.

The geometry of the baseline truck model is presented in Section 4.1, after which the mesh settings are presented in Section 4.2. The boundary conditions of the model are presented in Section 4.3 and finally Section 4.4 presents different variants that were simulated.

4.1 Geometry

The baseline truck model is presented in Figure 4.1, with the x-axis running through the centreline of the wheel, the y-axis in the symmetry plane and the z-axis intersecting with the floor of the truck cabin (DAF conventions). The emphasis in this research is on the flow in and near the wheelhouse. To reduce the complexity of the model, the underhood was modelled in detail, whereas areas above $Z = 0$m were kept as simple as possible. To ensure attached flow on the cabin and along the roof all edges were smoothened. This also means that features such as wipers, mirrors and sun visors were omitted from the model. The grille was open and modelled as realistically as possible such that flow is able to enter the underhood.

It is known that a tyre under load compresses and creates a contact patch. It was demonstrated that modelling the contact patch of a tyre is difficult, since the tyre is continuously deforming due to its rotation and wear (Sprot et al., 2012; Axerio-Cilies, 2012). On the other hand, it was postulated that the modelling of the contact patch is of importance (Hobeika, 2012). Furthermore, it was demonstrated that the side walls of the tyre are deformed near the contact patch due to compression (Axerio-Cilies, 2012; Sprot et al., 2012), illustrated in

Figure 4.2. Finally, the behaviour of the tyre in the contact patch is unknown and it can be argued that the deformation has an effect on the flow.

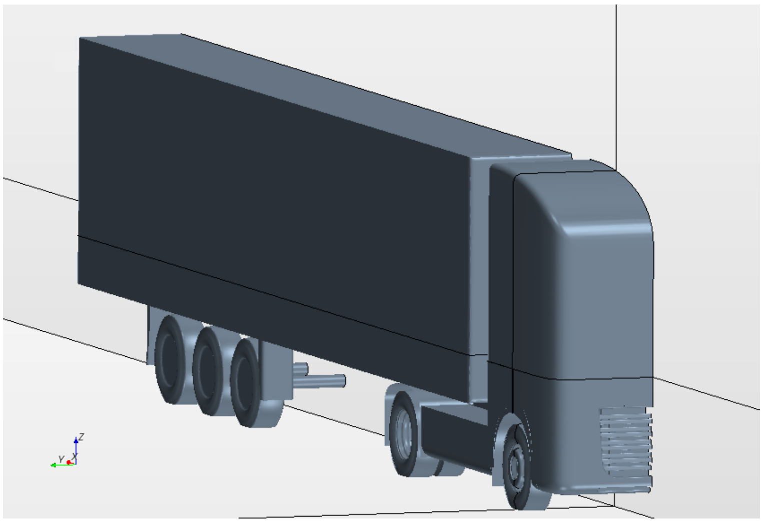

Figure 4.1: Baseline truck model geometry, with x- and z-axis plotted

Although the discussion above describes the need for a detailed and accurate representation of the contact patch, it was chosen to model it by intersecting the floor with the bottom 1.5 cm of the tyre (see Figure 4.3), essentially trimming the bottom of the tyre. The size of the contact patch due to a fully loaded truck was accurately modelled in this way, but tyre deformation effects were neglected in order to reduce model complexity.

The tyres of the trailer are of less importance to the flow in the wheelhouses, so they are modelled in less detail. Furthermore, the edges of the trailer are rounded with 2.5mm edges, to eliminate the effect of sharp pressure gradients.

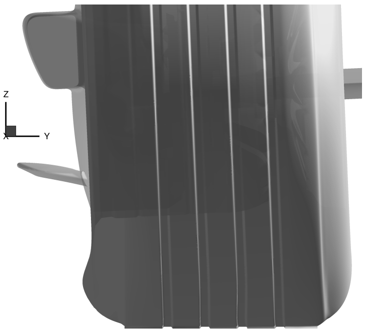

Figure 4.2: Bulge radius

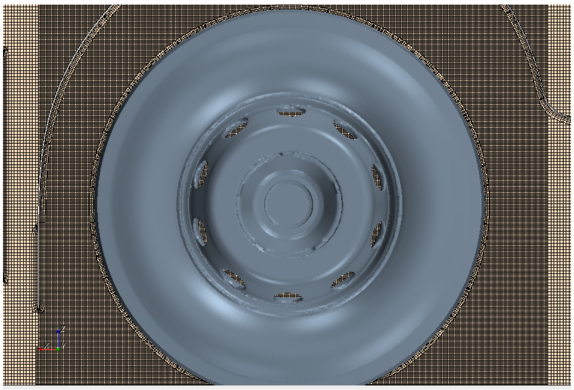

Figure 4.3: Mesh near the contact patch

The inner wheelhouse consisted out of two wheelwells and the side step for the cabin, as is shown in Figure 4.8(a). The inner part of the sidesteps, together with the front wheelwell, shields the front tyre. To save on computation time it was chosen to model the truck using a half model, as shown in Figure 4.1. It was shown that using a half model, for a steady state solver, results in an error in the order of 1% (Ahmad et al., 2009).

The truck model had a complete length (L) of 16.5m, width of 2.55m and height of 4.00m, in compliance with European regulations. The truck was simulated in open road conditions. The dimensions of the walls, measured from the origin as sketched in Figure 4.1, were as follows: width of the tunnel 5.5L, the height 4.5L and the length 7.5L upstream and 14.5L downstream. This resulted in a blockage factor of less than 0.01%, which was considered as sufficient to replicate open road conditions. The tunnel extended far enough downstream have a minimal influence on the wake formation.

4.2 Mesh settings

As described in the previous section the emphasis in the model is on capturing the phenomena that dominate in the region and wake of the wheelhouse. From the literature, this is the area where the dominating phenomena are anticipated. The mesh in these region was refined in order to capture these phenomena correctly.

From the validation study appropriate mesh settings were found. The validation study contained a wheel that is half as large as the current wheel, so the dimensions of the refinement areas were scaled up accordingly. The resulting dimensions of the major refinement areas, in the presence and in the wake of the contact patch can be found in Table 4.1 and are sketched in Figure 4.4.

A first simulation with the same mesh settings applied to the truck model, however, showed that the settings from the validation case could not be applied directly to the truck model. For starters, the separation of the flow on the shoulders of the wheel, which has been discussed in the previous section, showed asymmetrical behaviour. On the outboard side (i.e. flow side) of the wheel the separation spread wider than the refinement blocks could capture. Furthermore, the jetting vortex on the inner side of the tyre was less prominent than seen in the validation case. Therefore, keeping approximately the same amount of cells, it was chosen to redistribute more of the inboard cells to the outboard side. In this way the separation could be captured both in- and outboard, along with the wider wheel wake.

Table 4.1: Overview of refinement volumes

	Refinement areas	Cell size (mm)	Cell size (%)
1	Contact patch	1	3.125
2	Jetting vortex	2	6.25
3	Wheel wake + shroud	4	12.5
4	Underhood	8	25
5	Trailer + trailer	16	50

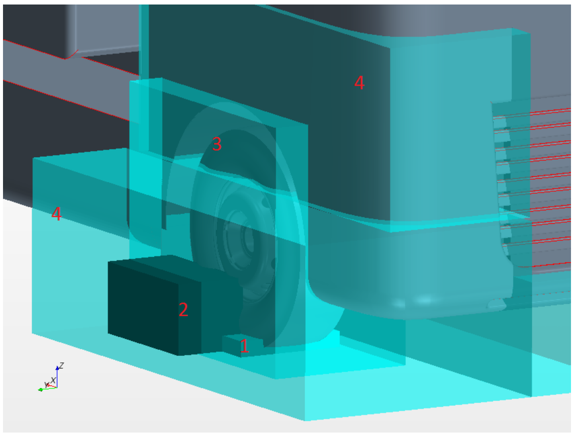

Figure 4.4: Distribution of refinement volumes on baseline truck model

The result was a mesh of more than 100 million cells. This was reduced by noting that the lower half truck was of primary interest, allowing derefinement in other areas. This finally resulted in a mesh size of 50-55 million cells. As discussed, the main focus is on the wheelhouse area and the wheel wake. The mesh in other areas was kept as large as possible, while capturing the basic phenomena. Figures 4.5 and 4.6 present an overview of the mesh size surrounding the truck. Due to the small scale of the cells, with respect to the length of the truck model, only the largest cells were visualised.

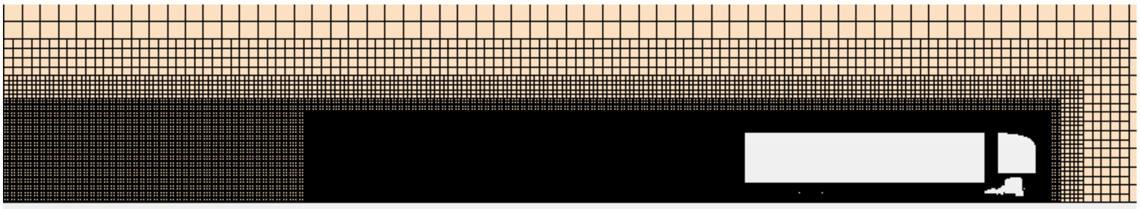

Figure 4.5: View of mesh around the baseline truck model

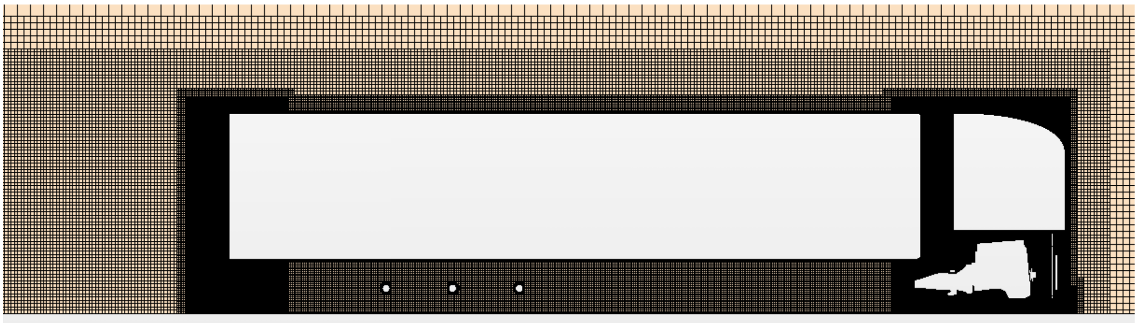

Figure 4.6: Close up view of mesh around the baseline truck model

4.3 Model settings

As discussed in the previous chapter the simulations were performed with steady state RANS and a k-ω SST turbulence model. Using wall functions resulted in the closest to the experiments, so y^+ values were above 30. There is no predetermined upper limit for y^+ values, but from Figure 3.2 it can be observed that y^+ values approaching 1000 start to deviate from the logarithmic law of the wall. It was recommended to keep the highest y^+ values around 200-300 (CD-adapco, 2013).

The inlet was modelled as a velocity inlet, with a 25 m/s uniform flow (90 kmph, 0° yaw) and the outlet was modelled as a pressure outlet. Since the model replicated a truck moving in open road conditions, the floor was set to move with 25 m/s. Furthermore, the wheels must be rotating. For a wheel of 0.5m radius, this equates to rotational velocities specified at the surface of the wheel of 50 rad / s. Due to the contact patch the radius was less than 0.5m, as illustrated in Figure 4.3. As a result a slightly higher velocity needed to be specified on the wheels.

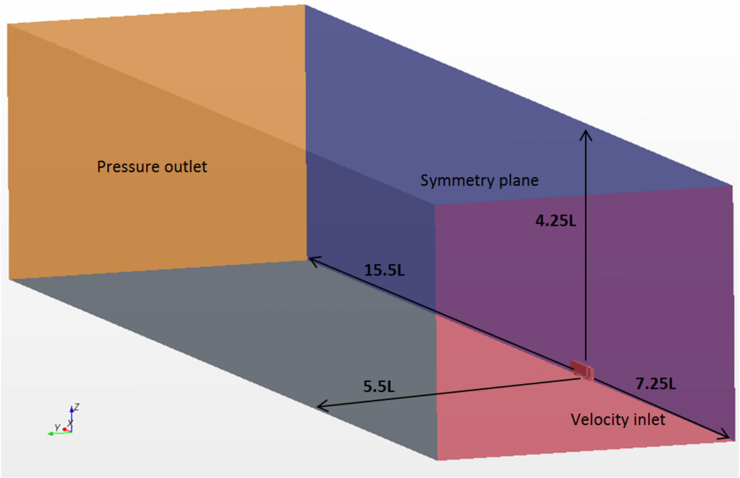

Figure 4.7: Boundary conditions of the walls surrounding the truck model

The conditions in the freestream were a uniform 25 m/s flow in the x-direction. To ensure freestream conditions at the walls, velocities on the walls (except for in- and outlet) were specified. Observing the conditions of the flow near the walls, it was seen that the flow was near freestream conditions and it was seen that the walls had a negligible influence on the flow field of the baseline truck model, making this a valid approach.

4.4 Modifications

To investigate the effect of geometry changes a range of modifications was tested. Some of the modifications were adapted from conclusions by other researchers, other modifications were based on the analysis of the results of the validation (presented in previous chapter) and the baseline truck model (presented in following chapter).

There are a few modifications that were done with the goal of preventing the outflow through the wheelhouse. To start, the complete closing of the wheelhouse (Figure 4.8(c)) logically prevents any outflow through the wheelhouse. This variant was considered to be the most optimal configuration for the current design of trucks, and was considered to assess the possible reduction in drag coefficient. A similar approach can be obtained by reducing the clearance gap between the tyre and the body (Figure 4.8(b)). This is a more viable option, since the tyres do not intersect with the bodywork and are not restricted by the cover during turns. Furthermore, it was seen that there is a large outflow at the mudguards (discussed in the next chapter) and it is thought that extending the body work up to the mudguards (Figure 4.8(d)) would prevent this. Furthermore, a wheelhouse side cover was placed to prevent air to flow from the underhood into the wheelhouse (Figure 4.8(g)). Finally, a top cover to decrease the volume of the wheelhouse (as suggested in the literature) was placed (illustrated in Figure 4.8(h)). All these variants had one goal in common: preventing flow from leaving the wheelhouse and alter the conditions in the wake.

Other variants that were considered focussed more on changing the up- and downstream conditions, i.e. deflecting air in and out of the wheelhouse. Three different kind of spoilers were simulated: two wheel spoilers with the intention of changing the upstream conditions in the underhood (Figures 4.8(f) and 4.8(e)) and one wheel spoiler that deflected the flow upstream away from the wheel (Figure 4.8(i)). The wheelhouse vent (Figure 4.8(l)) was also placed to deflect flow out of the wheelhouse into the freestream in a more favourable manner.

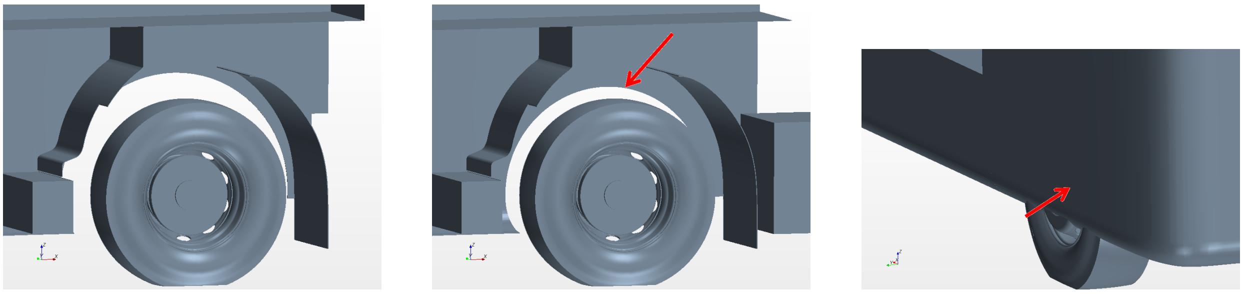

(a) Baseline (B)

(b) Clearance 6cm (6CM)

(c) Covered wheelhouse (WCR)

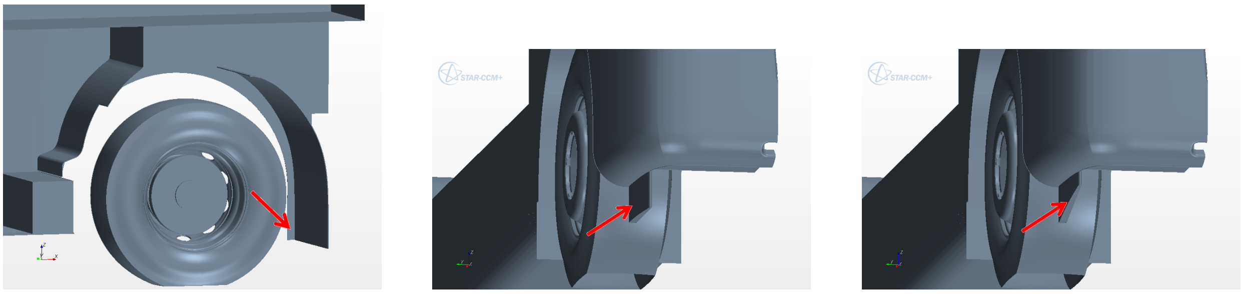

(d) Mudguard extension (MGC)

(e) Spoiler (S)

(f) Trimmed spoiler (TS)

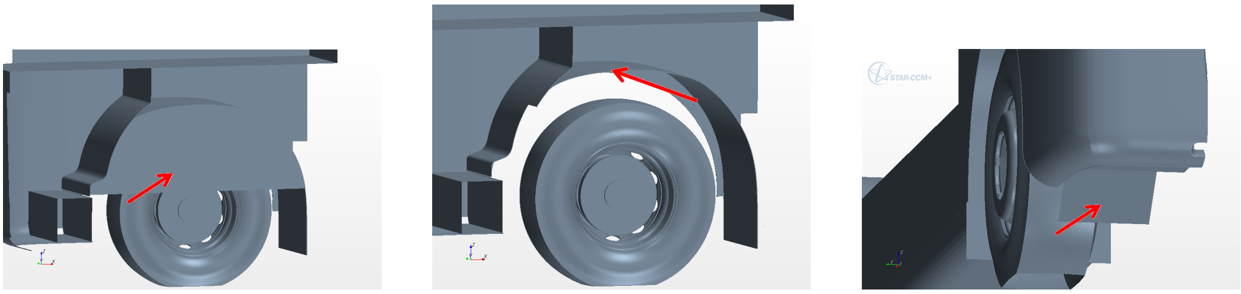

(g) Side cover wheelhouse (WSC)

(h) Top cover wheelhouse (WTC)

(i) 45° spoiler (W45)

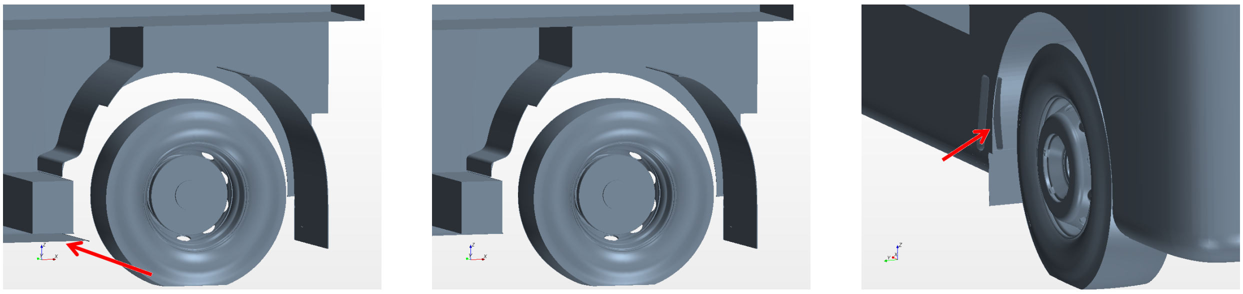

(j) Underhood cover (UHC)

(k) Aligned wheel (WA)

(l) Wheelhouse ventilation (WHV)

Figure 4.8: Overview of modifications

Chapter 5

Results

In this chapter the results of the baseline model and the variants are presented and analysed. Since it was seen that the results are dependent on the iteration, Section 5.1 begins with a description of how to use the results of the simulations. Section 5.2 presents the results of the baseline model and compares it with the results of the validation model. Section 5.3 then briefly presents the results of the modifications, while Section 5.4 presents a detailed analysis of the variants. A comparison of the variants with the literature is presented in Section 5.5, after which a summary of the chapter is presented in Section 5.6.

5.1 Statistical analysis

Chapter 3 demonstrated that even though a steady state solver was used, the variables showed fluctuations per iteration. This section starts with creating averaged values, eliminating the dependence on iteration and useful for the analysis further on.

Figure 5.1 presents the drag coefficient per iteration of the baseline model. It can be seen that the fluctuations per iteration are large, with the difference in drag coefficient between the minimum and maximum close to 0.05. It can be estimated from Figure 5.1 that the standard deviation is in the order of 10-15% of the mean drag coefficient. Considering that improvements in the drag coefficient of the modifications were in the order of 1%, it shows the need for a better method of accurately predicting the mean drag coefficient. For this application it is best to compute the standard error, which indicates how close the estimated mean is to the real mean. The definition of standard error is presented below:

$$SE_x = \frac{s}{\sqrt{n}} \tag{5.1}$$

Where s is the real standard deviation, and n the size of the population. This illustrates that the larger the population size n, the more accurate the prediction of standard error

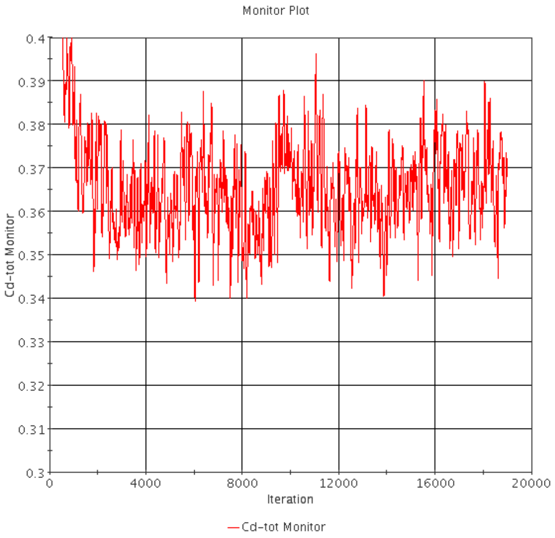

Figure 5.1: Drag coefficient of baseline model

becomes. It must be noted, however, that the standard deviation s in Equation 5.1 is the real standard deviation and that statistical analysis only computed an *estimate* of the real standard deviation. It was assumed that the estimate of the standard deviation was equal to the real standard deviation. Internal discussions determined that this is valid if the data set is large enough.

However, this method can only be used when the data is uncorrelated. Since the drag coefficient of iteration i is heavily dependent on the outcome of iteration i-*1*, the current data set is correlated. Using an autocorrelation function (ACF) the amount of correlated data was determined. The autocorrelation of the baseline truck model is plotted in Figure 5.2 and shows a clear oscillating pattern, showing that the solution is dominated by periodic phenomena. Internal discussions also determined that an ACF value of 0.2 was the threshold for data being correlated or not. Figure 5.3 shows that this threshold was reached after 43 iterations. In other words, the first 43 iterations after iteration i are affected and cannot be treated as separate measurement points. It was found that the autocorrelation of the variants resulted in roughly the same number. To ensure that the ACF remained under 0.2 for all variants a

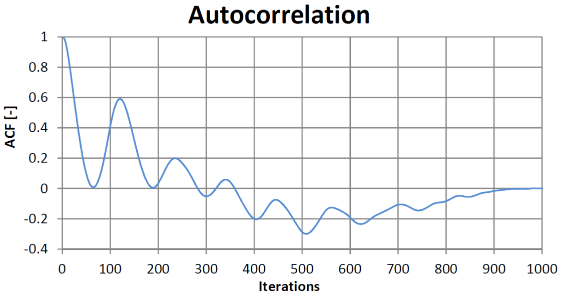

Figure 5.2: Autocorrelation function of the baseline truck model

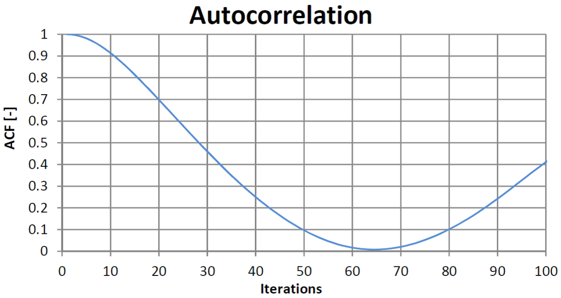

Figure 5.3: Close-up of the first valley of the autocorrelation of the baseline model

threshold of 50 iterations was taken. Therefore, when calculating the standard error not n points must be used, but $\frac{n}{50}$ to compensate for the autocorrelation of the data. The standard error then gives the band in which the real mean is located. If the band for the modifications falls outside of the band of the baseline truck model, the result is called significantly different (see Figure 5.19).

5.2 Baseline truck model results

This section presents an analysis of the results of the baseline truck model. Furthermore, a comparison of the baseline model with the validation model was made. Finally, the behaviour of the flow downstream of the wheelhouse was discussed, since this was not taken into account in the validation study.

5.2.1 Flow fields

This section presents the flow fields of the baseline truck model. Most of the analysis was done in Z-planes, illustrated in Figure 5.4. For convenience, the non-dimensionalised coordinate Z/D was introduced, which will be used in the next sections. With Z being the distance measured from the floor, Z/D = 0 corresponds to the floor and Z/D = 1 to the top of the wheel. Note that the Z-coordinate is translated with respect to the coordinate system shown in Figure 4.1.

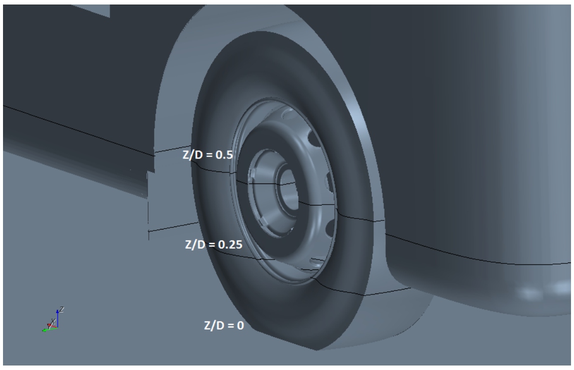

Figure 5.4: Location of planes used in the analysis of the flow fields

Figures 5.5 and 5.6 present sections of velocity and Figures 5.7 and 5.8 sections of total pressure coefficient. A large wake region was observed next to the front wheel, which grows significantly in size further downstream. It was seen that this wheel wake extended from the floor to the top of the wheelhouse. The energy in wake region was dependent on the vertical position. The lowest values of total pressure were found in the lower wheel wake: Z/D < 0.25.

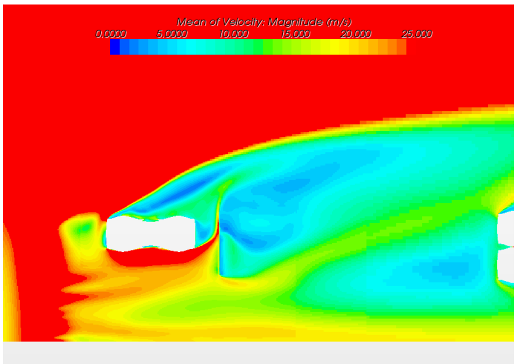

Figure 5.5: Baseline: velocity magnitude, Z/D = 0.2

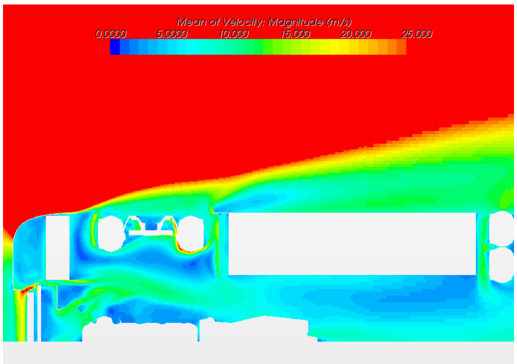

Figure 5.6: Baseline: velocity magnitude, Z/D = 0.5

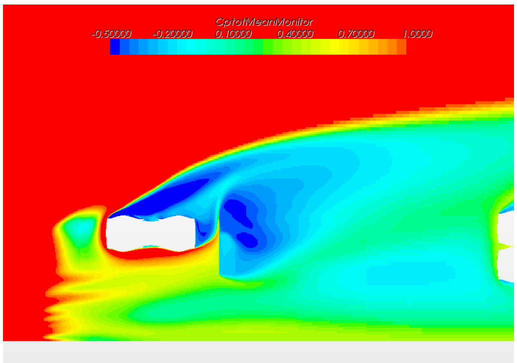

Figure 5.7: Baseline: total pressure coefficient, Z/D = 0.2

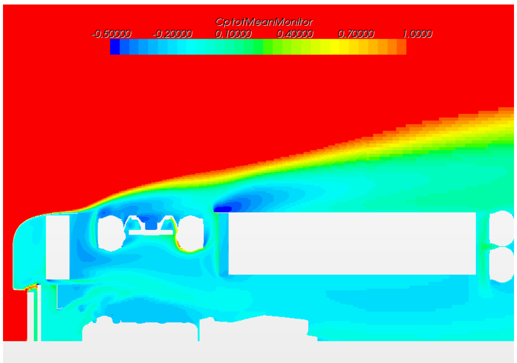

Figure 5.8: Baseline: total pressure coefficient, Z/D = 0.5

Furthermore, Figures 5.7 and 5.8 show that the flow through the underhood lost a lot of energy, which is the main reason that the underhood is a large contributor to aerodynamic drag. Furthermore, it shows large separation regions induced by the mudguard. Finally, observing Figures 5.7, 5.8 and 5.9 it can be concluded that most of the massflow through the wheelhouse occurs at locations of $Z/D < 0.5$. It was also seen that the width of the lower wheel wake was largest, which was caused by the larger outflow at lower locations.

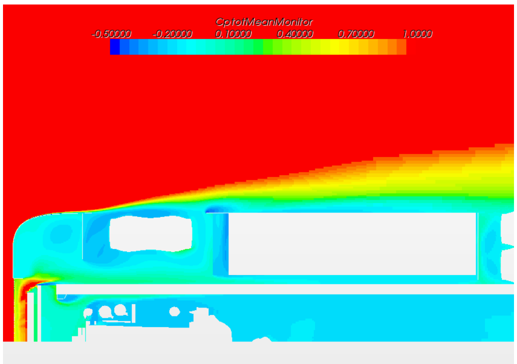

Figure 5.9: Baseline: total pressure coefficient, Z/D = 0.8

5.2.2 Comparison with validation model

This section presents a comparison of the flow structures in the wheelhouse of the baseline model with the flow structures described in the validation study and the literature. Since no experimental data was available, this comparison serves as a confirmation whether the results can be trusted.

Figures 5.10 and 5.11 present the pressure coefficient through the centreline of the wheel for the baseline and validation model, respectively. It can be seen that there is a significant difference in stagnation on the front wheel. The flow in the baseline model, has a stagnation region lower than in the validation model. The bumper of the truck shields a larger part of the wheel, but also triggers separation. Furthermore, flow moves out of the gap behind the bumper, illustrated with the arrow, enlarging the separated region. Due to the flow out of the gap behind the bumper, the freestream flow is being squeezed through an effectively smaller area, which increases the incoming velocity on the tyre.

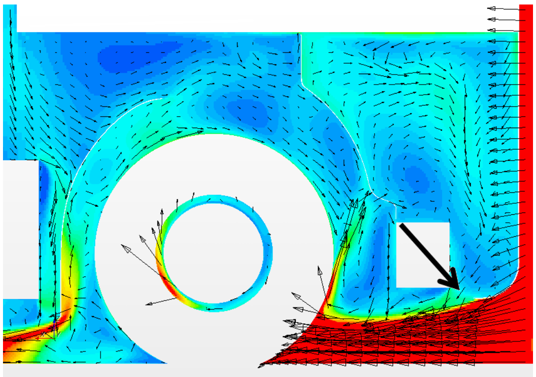

Figure 5.10: Truck baseline: velocity vectors, plotted on $C_{p,t}$ field, centreline of the wheel

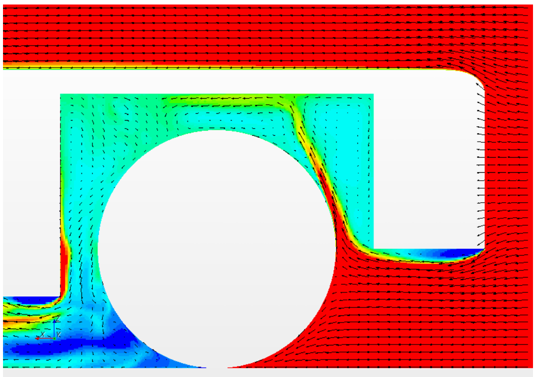

Figure 5.11: Validation model: velocity vectors, plotted on $C_{p,t}$ field, centreline of the wheel

In the validation study, and in the literature, it was seen that the freestream flows into the wheelhouse. Figure 2.13 showed that a part of the freestream followed streamline 3 into the wheelhouse. Eventually this resulted in separation due to the tyre rotation, creating a vortex that moved into the freestream. When the stagnation point of the wheel is lower, as the difference between Figures 5.10 and 5.11 shows, less air flows into the wheelhouse.

Figures 5.12 and 5.13 present the flow near the contact patch of the validation and baseline truck model, respectively. In the validation model, the flow onto the tyre was undisturbed. It is seen however that the flow in the truck model is under an angle. Comparing Figures 5.12 and 5.13 it becomes clear that the yawed flow creates an asymmetric distribution of the jetting vortices and wheel wake. The yawed flow suppresses the separation of the flow on the inboard side of the wheel, reducing the size of the inboard jetting vortex. On the other hand, the yawed flow induced more separation on the outboard side of the tyre, which results in a larger wake. This shows that the jetting phenomenon remains present, but the size and strength of the resulting wheel wake are dependent on the conditions in the flow upstream.

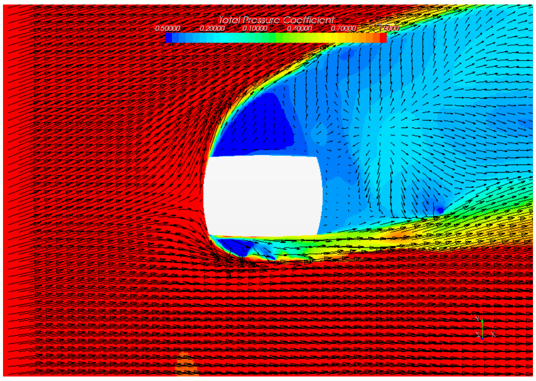

Figure 5.12: Truck baseline: velocity vectors, plotted on $C_{p,t}$ field, Z/D = 0

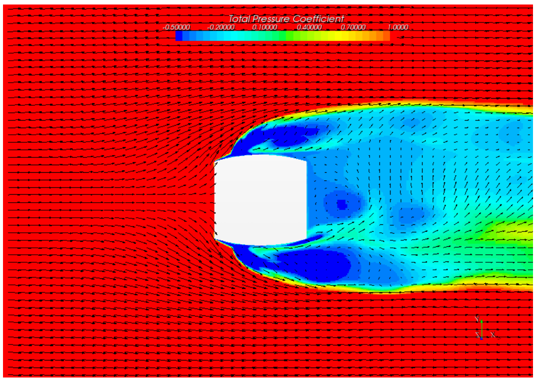

Figure 5.13: Validation model: velocity vectors, plotted on $C_{p,t}$ field, Z/D = 0

The yawed flow is induced by the strong crossflow component at the front of the tractor due to the stagnation flow. This crossflow component entrains the flow in the direct underhood, creating the yawed inflow on the front tyre. It was found that there was a slight variation in vertical distribution of yaw angle, in the centreline of the wheel. The variation was between $26 - 27°$.

Furthermore, the presence of the mudguard was found to have a large influence on the velocity field. It was seen in the studies that the wake of an isolated wheel mostly consists of the counter rotating pair of vortices, located at Z/D < 0.25. The mudguard of the truck intrudes into this region and disturbs the wake formation. Figures 5.5 and 5.7 show that there is a large crossflow, coinciding with the location of the mudguard.

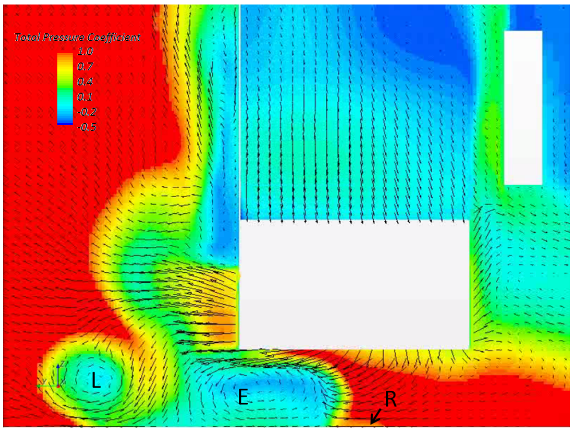

Figure 5.14: Baseline model: distribution of $C_{p,t}$ near the mudguard, plotted with velocity magnitude vectors in normal plane

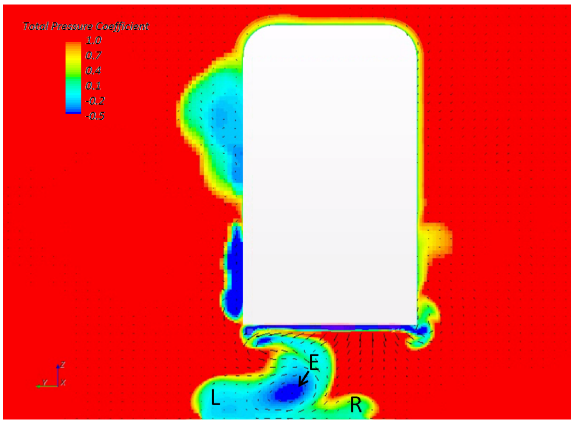

Figure 5.15: Validation model: distribution of $C_{p,t}$ behind the wheel, plotted with velocity magnitude vectors in normal plane

Figures 5.14 and 5.15 show the wake formation for the baseline and validation model, respectively. The position of the vortices in the validation model remained at the location where they originated and were not disturbed in their formation. On the other hand, the position of the vortices in the baseline truck model was shifted outboard. It was observed that the large crossflow of the mudguard was one of the reasons for the shift in vortex position. The yawed flow in the underhood was also responsible for the shift in vortex positions. Figure 5.14 also shows that the outboard vortex L significantly grew in size and inboard vortex R was almost eliminated.

5.2.3 Effects of geometry on wake formation

The previous section focussed on the comparison of the flow structures of the validation and baseline truck model. Since the validation models and the models in the literature were studies on isolated wheelhouses, the interference of the wake with the geometry downstream has not been investigated. This section discusses the behaviour of the flow downstream of the wheelhouse.

Just as in the validation study, isosurfaces of Q-criterion and total pressure coefficient were compared with the literature. Figure 5.16 and Figure 5.17 present the isosurfaces of zero total pressure and Q-criterion, respectively. The jetting vortices were identified clearly with both methods. Furthermore, a large wake at the top of the wheelhouse was observed, reminiscent of vortex structure A observed in Figure 2.13.

It was also found that the outflow of air behind the bumper gap resulted in separation on the bumper edge, creating a vortex that propagated downstream and interfered with the wake formation of the wheel. This vortex is highlighted in Figure 5.16 and also was identified in Figure 5.17. The existence of this vortex is specific to truck models, but was not observed other studies on trucks (Söderblom et al., 2009). Separation regions S and B were identified in Figure 5.16, although the vortex induced by the separation of the bumper and vortex A dominated the flow in the upper wheel wake.

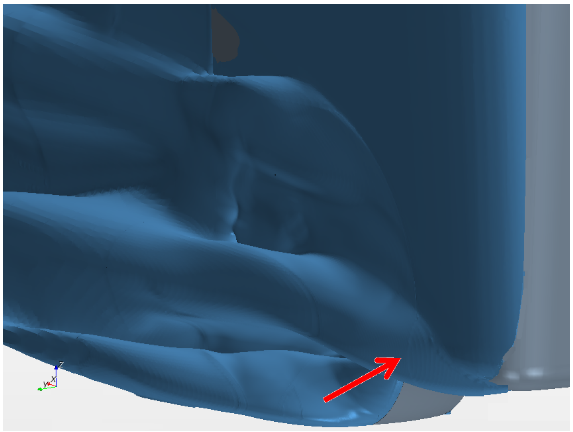

Figure 5.16: Baseline model: isosurfaces of $p_{tot} = 0$

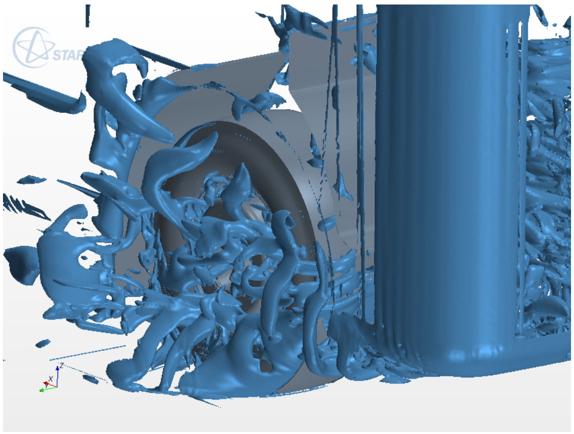

Figure 5.17: Baseline model: isosurfaces of QD/U_∞ = 50000

As a result of the trailer behind the tractor, the formation of the wake was disturbed. It was already demonstrated that the wake showed an unsteady behaviour. Figure 5.18 presents the result of the baseline model for two different iterations. It can be observed that the total pressure coefficient does not show much fluctuations in the front wheel region. The energy in the wake next to the front wheel looks constant, whereas small changes in energy were found behind the front wheel and throughout the underhood. The largest fluctuations, however, were observed in the flow behind the rear wheels and in front of the trailer wheels. The direction of the flow impinging on the trailer mudguards changed per iteration. This is one of the contributors to the fluctuations in drag coefficient.

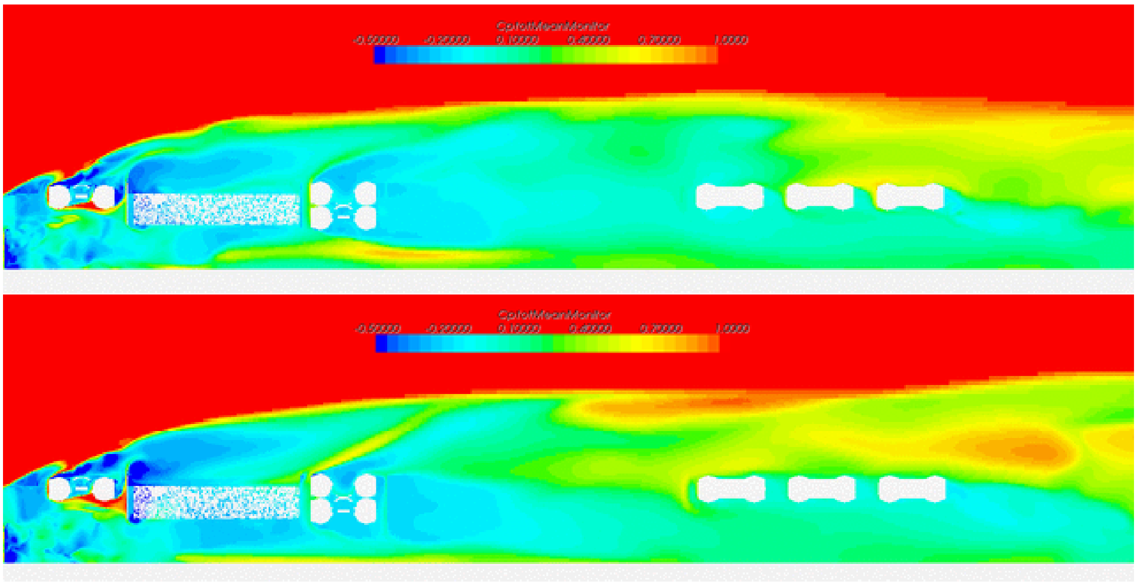

Figure 5.18: Baseline model, distribution of $C_{p,t}$, Z/D = 0.5 for two different iterations

5.3 Results of the modifications

The results of the study of the variants are presented in Figure 5.19 and Table 5.1. Due to the large number of iterations of the baseline simulation the estimated mean is within 0.2% of the real mean. Note that drag coefficients were normalised, with respect to the baseline, for convenience.

Figure 5.19 shows that 5 of the modifications have a significant difference in drag coefficient; 4 of them have a beneficial effect on the drag coefficient and 1 resulted in a higher drag coefficient. This does not necessarily mean that the results of the other variants should be disregarded. An analysis of their flow fields might result in a better understanding of the changes in flow fields.

It was chosen to analyse the two modifications that resulted in the most significant drag reduction, i.e. closed wheelhouse with rotating wheels and the wheelhouse side cover variant. The closed wheelhouse with stationary wheels was not analysed, since its behaviour with respect to rotating wheels was sufficiently described in the literature.

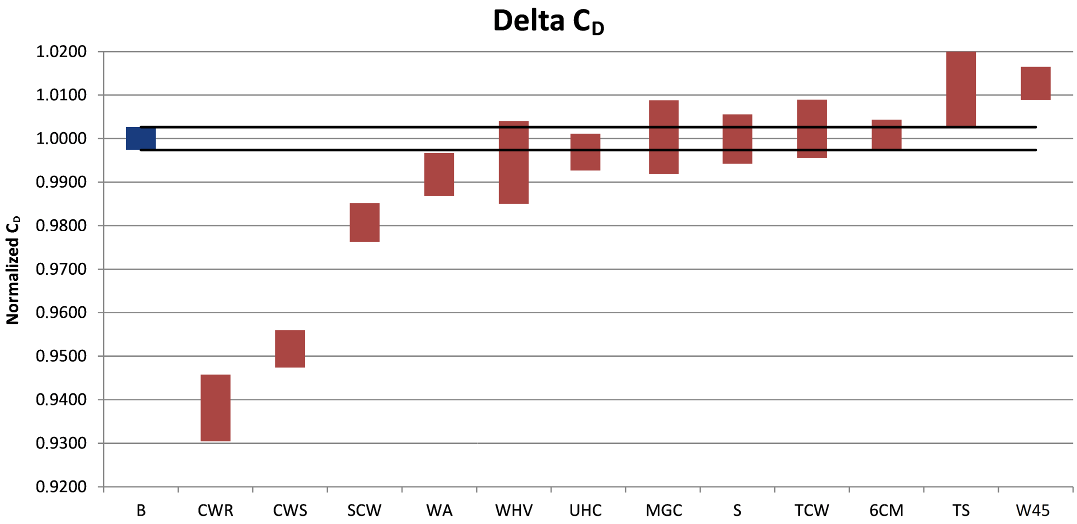

Figure 5.19: Drag coefficients of modifications, compared to baseline

Table 5.1: Drag coefficient of modifications

Name	Description of variant	Normalised C_D	Standard error
B	Baseline	1.000	0.0010
CWR	Closed wheelhouse, rotating wheels	0.938	0.0028
CWS	Closed wheelhouse, stationary wheels	0.952	0.0016
SCW	Side cover wheelhouse	0.981	0.0016
WA	Alignment of wheel with outer body	0.992	0.0018
WHV	Wheelhouse ventilation	0.995	0.0035
UHC	Extension of bumper into underhood	0.997	0.0015
MGC	Extension of mudguard	1.000	0.0031
S	Spoiler in front of wheel	1.000	0.0021
6CM	Smaller clearance gap between body and wheel	1.001	0.0012
TS	Spoiler in front of wheel, trimmed	1.013	0.0035
W45	45° spoiler in front of wheel	1.013	0.0014

Furthermore, the variant with a 45° wheel spoiler was chosen, because of its significantly higher drag coefficient. Finally, two more variants were chosen since their flow fields helped with understanding the sensitivity of the flow, i.e. the clearance gap and underhood cap.

5.4 Analysis of modifications

In the previous section the results of the simulations with the modifications were presented. In this section the results are analysed in order to understand the sensitivity of the flow with respect to the variants. This was done using both a quantitative analysis, e.g. plots of velocity and pressure, and a qualitative analysis, e.g. drag buildup and massflows through the underhood. By analysing the change in flow structures, flow phenomena that dominate the sensitivity of the drag coefficient can be identified.

5.4.1 Drag buildup

The first approach to understanding the changes in flow field is plotting the buildup of drag over the length of the truck. Comparing the drag buildup of the different variants highlights the differences in drag and the location of the areas most affected.

The drag buildup of the baseline model is presented in Figure 5.20. The drag is obtained by computing the surface integral of mean pressure and extracting the component in the flow direction. This yields the mean force in the flow direction, i.e. pressure drag. Since shear forces were not considered in this method the computed drag coefficient is approximately 10% lower than presented in the previous section. This shows that the total drag of the truck consists for 90% out of pressure drag. Figure 5.20 shows that the major components contributing to the total drag are the front of the tractor, the back of the trailer and all the wheels. Furthermore Figure 5.20 demonstrates that shear forces were not considered, since the drag does not increase over large parts of the trailer. Note that although the pressure drag is not equal to the actual drag it is a useful exercise, since it visualises the major affected areas.

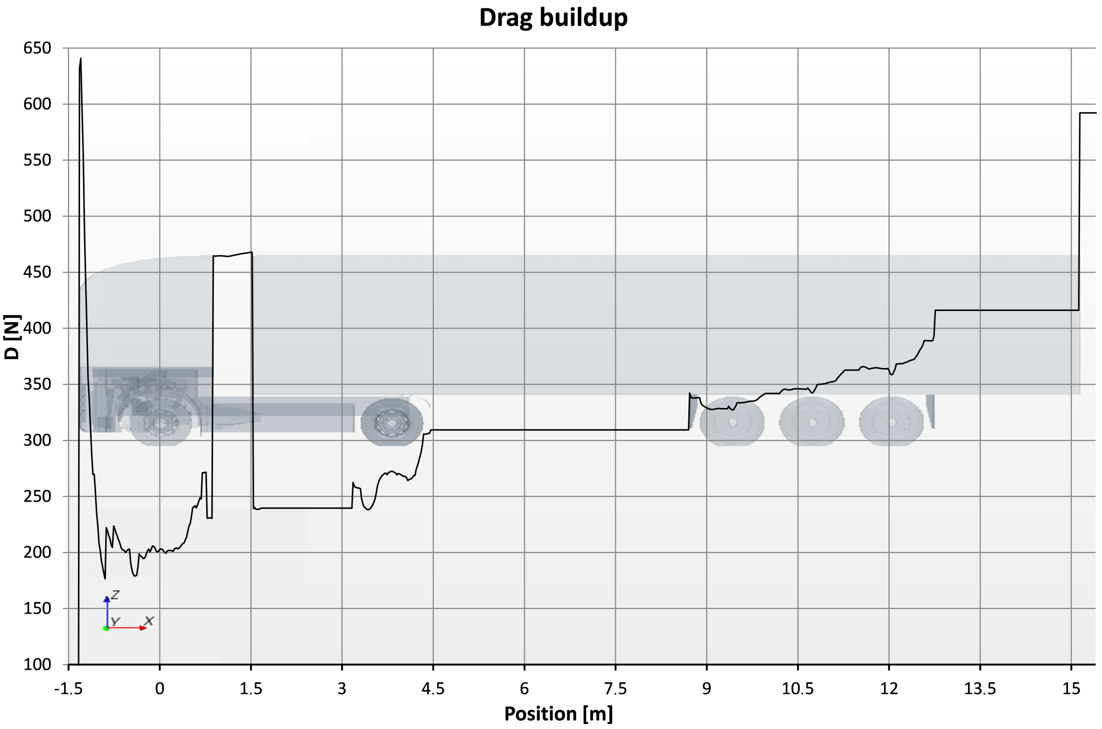

Figure 5.20: Buildup of drag of the truck model (pressure drag only)

The scale in Figure 5.20 is so large, and changes in drag between variants are small, that the differences between the variants were not visible. Therefore, instead of plotting the drag buildup for all variants, the difference in drag with respect to the baseline is computed and plotted in Figure 5.21. Furthermore, in order to clearly visualise the area of interest, a close-up of difference in drag in the wheelhouse area is presented in Figure 5.22.

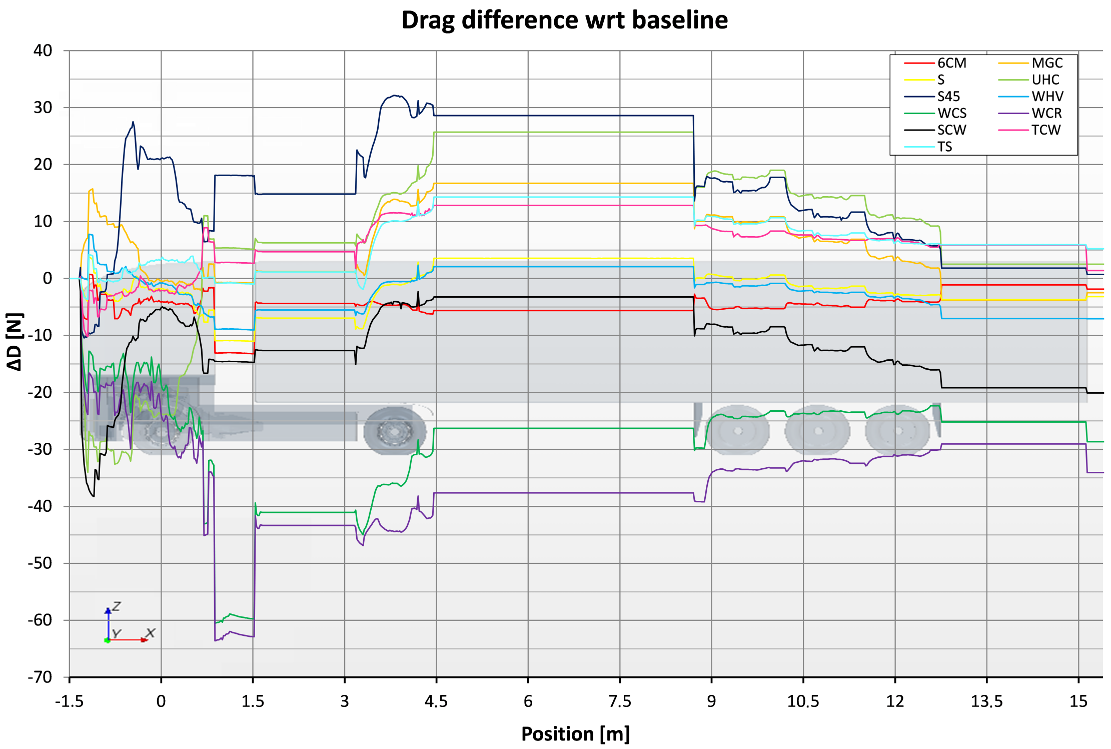

Figure 5.21: Difference in drag buildup, compared to baseline

There are a few observations that can be made from Figures 5.21 and 5.22. To start, the drag is not only affected in wheelhouse region, but also shows large changes downstream. It is seen that the closed wheelhouse results in a total drag on the tractor which is about 30 N (5% of the total drag) lower than in the baseline case. However, it also shows an increase in drag on the rear tractor and trailer wheels. It was already suggested in the literature that local changes could have a significant effect downstream (Söderblom et al., 2009).

The buildup of drag can also be done for the wheel only. Figure 5.23 shows that there are only two simulations that have a significant effect on the drag buildup over the wheel. It was seen that both simulations had a change in position where drag started to increase. From Figure 5.10 it was observed that the stagnation point is beneath the vertical centreline. A change in vertical position of the stagnation point also affects the horizontal position. It was seen that the underhood cap resulted in a higher stagnation point on the wheel. This shifts the stagnation point forward, resulting in an increase of the point where drag is increased. Reversely, the 45° wheel spoiler created a lower stagnation point, decreasing the point where drag is increased. From Figure 5.23 it can be concluded that the total pressure drag of the wheel of the baseline truck model is approximately 3% of the total drag.

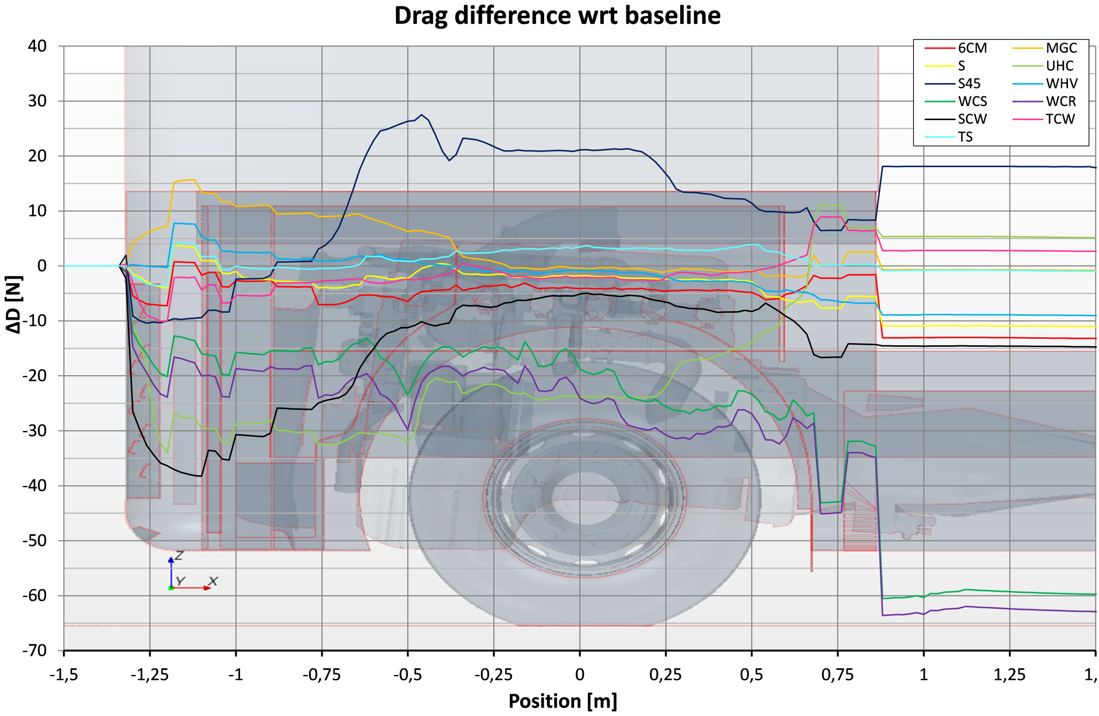

Figure 5.22: Difference in drag buildup, close-up of wheel region, compared to baseline

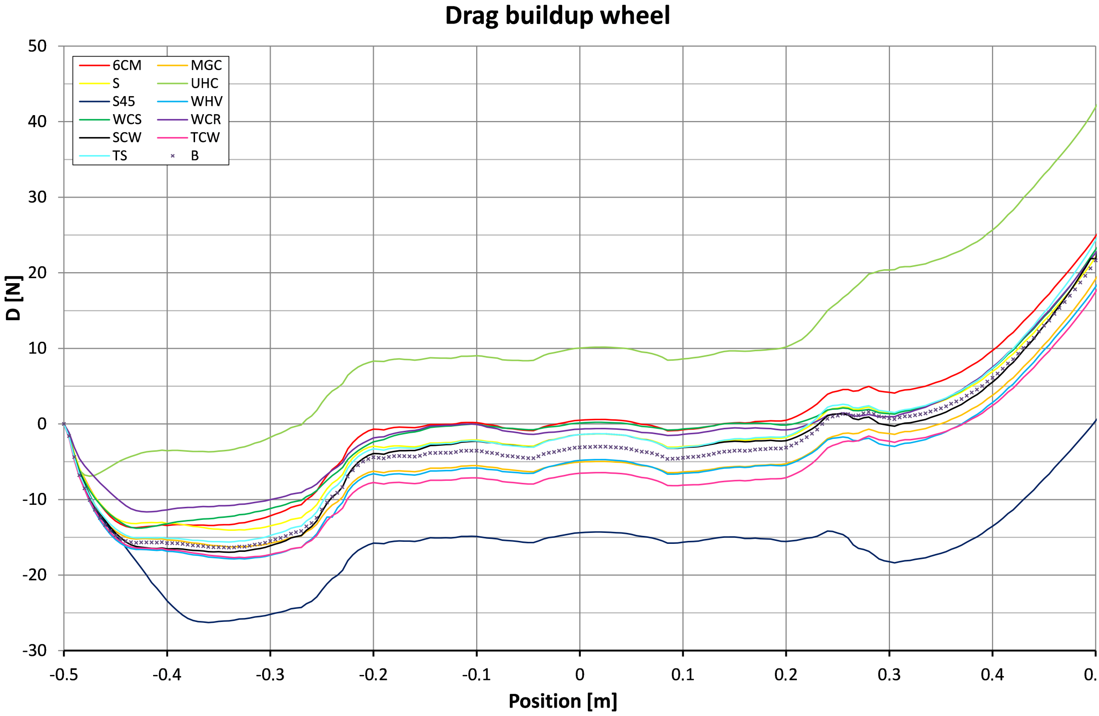

Figure 5.23: Drag buildup of wheel, enclosed by the wheelhouse

5.4.2 Massflow distribution

A second tool for analysing the effect of the variants on the flow field is the massflow through the underhood. This section presents the massflows measured throughout the underhood. Since the massflow through the underhood is primarily in alignment with the direction of flow, changes are only dependent on the normal velocity component. The effects of the variants on the flow can be clearly visualised through the change in massflows.

Figure 5.24 presents the locations of the planes at which the averaged massflow in x-direction was monitored. To clearly highlight the position of the monitors in the underhood it was chosen to leave the monitor at the trailer wheels (5) out of this picture. To have a feeling for the amount of flow entering and leaving the system, it was also chosen to monitor the massflow through wheelhouse, see Figure 5.25. Massflow monitors 1, 2, 6, 8 and 9 in Figure 5.24 and 2 and 4 in Figure 5.24 create a closed system, such that changes in in- and outflow conditions can be identified rapidly.

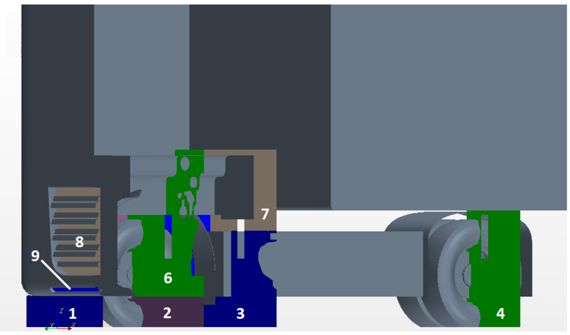

Figure 5.24: Location of planes in underhood that measure massflow in x-direction

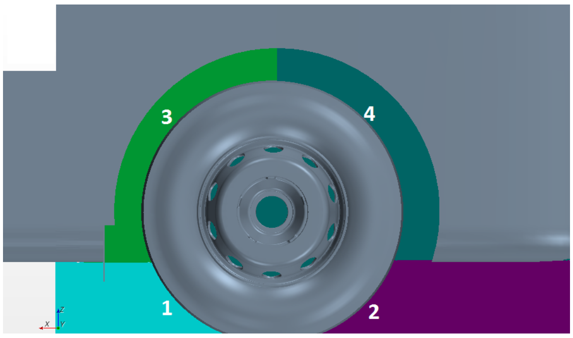

Figure 5.25: Location of planes in wheelhouse that measure massflow in y-direction

For convenience the massflows through planes at the same x-location were added to obtain the distribution of massflow through the underhood. These values are summarised in Table 5.3 and the individual monitors are presented in Tables A.1 and A.2 in Appendix A. Figure 5.26 presents the distribution of massflow through the underhood, as a percentage of the massflow at the beginning of the underhood and Figure 5.27 presents the difference with respect to the baseline. The indices of Figures 5.26 and 5.27 are given in Table 5.2. A correlation study showed that there is no relation between the massflow at any plane in the underhood and drag coefficient.

Table 5.2: Definition of the indices in Figure 5.26 and 5.27

Index	Massflow planes	Location
Station 1	2, 6	Front wheels
Station 2	3, 7	Back of the cabin
Station 3	4	Rear wheels of tractor
Station 4	5	Trailer wheels
Station 5	1,2,3,4 (y)	Wheelhouse

Figure 5.26 and Table 5.3 show that the massflow through the underhood decreases along the

Table 5.3: Massflow through underhood, as percentage of massflow at the beginning of the underhood

	Front wheels	Cabin back	Tractor back wheels	Trailer wheels	Wheelhouse
6CM	0.768	0.648	0.362	0.643	0.346
UHC	0.816	0.698	0.385	0.602	0.292
WCR	0.781	0.696	0.395	0.711	0.288
W45	0.751	0.635	0.426	0.540	0.356
SCW	0.736	0.640	0.375	0.597	0.356
B	0.759	0.635	0.379	0.663	0.352

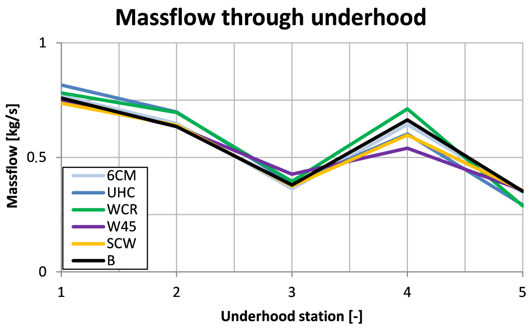

Figure 5.26: Distribution of massflow through the underhood

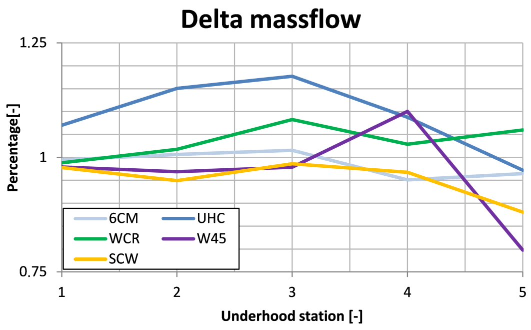

Figure 5.27: Difference in massflow distribution, compared to the baseline

length of the underhood. It shows that less than 60-70% of the massflow that enters through the grille and underhood reached the back of the cabin and only 35-40% of the massflow reached the rear tractor tyres. The rest of the massflow left the underhood through the sides, with 30-35% of the massflow leaving through the front wheelhouse. The other areas where massflow can leave the underhood were not monitored, but it was thought that the flow the front and rear tyre was a large contributor. This was already postulated in Section 5.2.

5.4.3 Closed wheelhouse, rotating wheels

It was found that the closed wheelhouse variant resulted in the lowest drag coefficient. This section focusses on the analysis of the velocity and pressure fields and highlights the differences with respect to the baseline simulation.

It was seen that even for this variant it is difficult to find differences in flow fields with respect to the baseline simulation. Therefore plots that show the difference between the two simulations (deltas) were computed. The following sections present velocity and (total) pressure coefficient deltas in order to gain an understanding in the effect of the modification.

Figures 5.28 and 5.30 present the velocity magnitude deltas for Z/D = 0.2 and Z/D = 0.5, respectively. Figures 5.29 and 5.31 present the total pressure coefficient deltas for Z/D = 0.2 and Z/D = 0.5, respectively. Figures 5.28 - 5.31 show that there is a strong agreement between velocity and total pressure coefficient deltas. Since the velocity deltas do not bring extra information it was chosen to only show the total pressure coefficient deltas. The remaining velocity figures are presented in Appendix B.

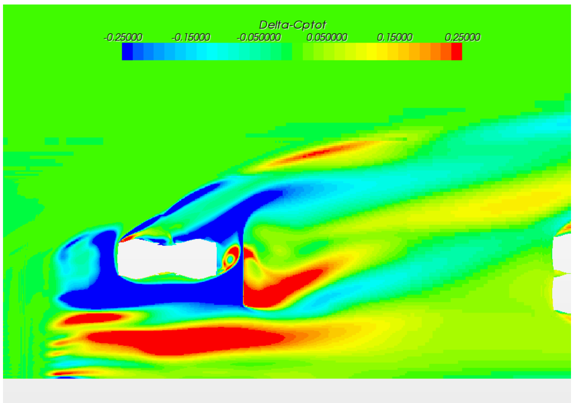

Figure 5.28: $C_{p,t,wcr}$ - $C_{p,t,b}$, Z/D = .2

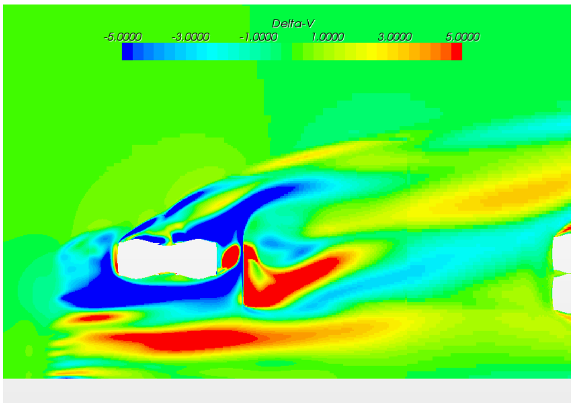

Figure 5.29: $V_{mag,wcr}$ - $V_{mag,b}$, Z/D = .2

Figures 5.28 shows a significant decrease in total pressure in the wheelhouse, which was the main reason for the local decrease in drag for this variant. Three major different flows were distinguished in Figures 5.28 - 5.31, of which the low energy in the wheelhouse was the first. It was observed that there was a higher stream of flow leaving through the gap behind the bumper, resulting in a higher flow through the underhood as discussed in Section 5.2.2. Secondly, since the model did not contain a mudguard there was less outflow as is illustrated in Figures 5.28 and 5.29.

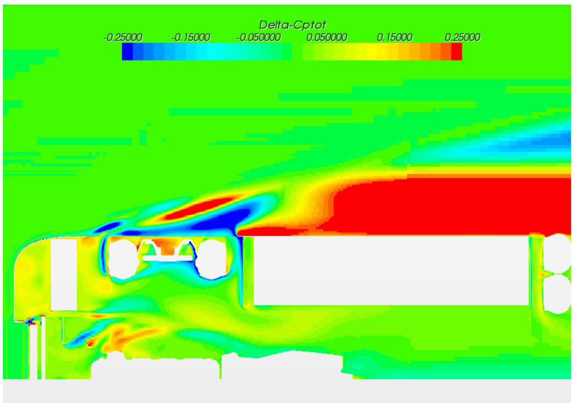

Figure 5.30: $C_{p,t,wcr}$ - $C_{p,t,b}$, Z/D = .5

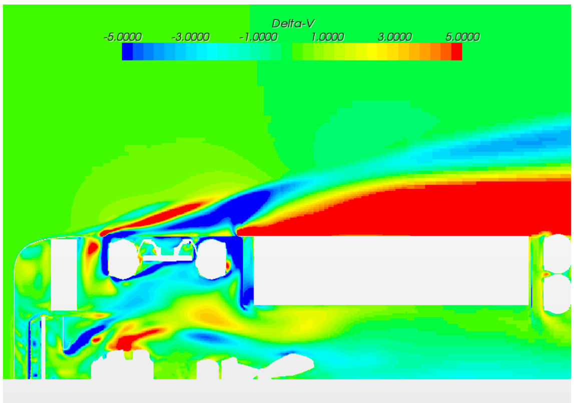

Figure 5.31: $V_{mag,wcr}$ - $V_{mag,b}$, Z/D = .5

Figures 5.28 and 5.30 show that the energy in wheel wake increased significantly. Observing that this region is dominated by separated flow, this suggests that the width of the wake was decreased. Figure 5.33 presents the isosurfaces of zero total pressure (blue), compared with the baseline isosurfaces (green). This shows that the width of the upper wheel wake was indeed reduced. It also shows that due to the higher outflow through the gap behind the bumper, the bumper vortex was more pronounced.

It is also shown that there is an increase in the width of the lower wheel wake. Table 5.3

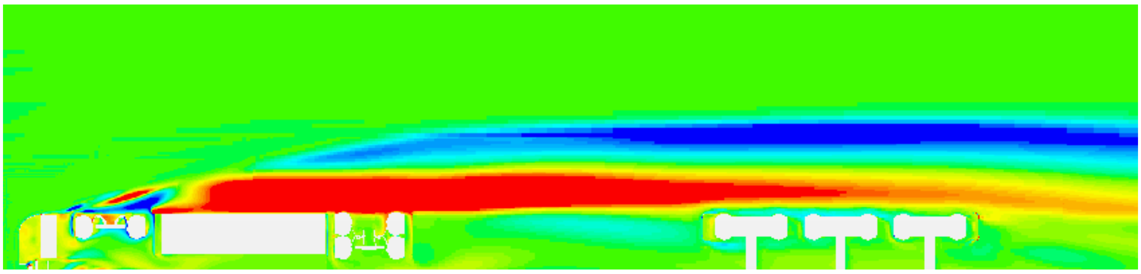

Figure 5.32: $C_{p,t,wcr}$ - $C_{p,t,b}$, Z/D = .5

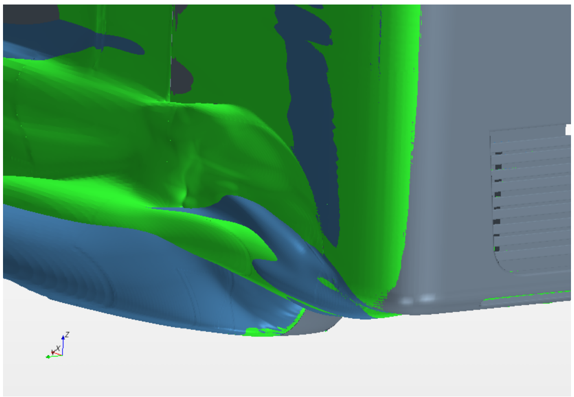

Figure 5.33: Wheelhouse closed rotating: isosurfaces of $p_{tot} = 0$

shows that the flow into the underhood remained approximately equal to the baseline flow. However, there is more outflow in the lower part of the wheelhouse. This increase in outflow behind and in front of the front tyre resulted in a wider wheel wake.

It was thought that completely closing the wheelhouse would result in a beneficial behaviour of the flow in the wheel wake. However, Figure 5.20 indicates that the closed wheelhouse results in an increase of drag of the trailer wheels. Figure 5.32 presents the difference in total pressure coefficient including the trailer wheels. The increased energy on the outboard side of the wheelhouse propagates downstream onto the trailer wheels, which results in a local increase in drag.

5.4.4 Wheelhouse side cover

The wheelhouse side cover variant also showed a significant reduction in drag coefficient. It was thought that preventing air from entering the wheelhouse resulted in less outflow. It was expected that this resulted in a decrease in drag coefficient. This section presents an analysis of the results of the wheelhouse side cover to identify the source of drag reduction.

In contrast to expectations, Figure 5.21 shows a significant increase in drag in the wheelhouse region. Figure 5.35 shows an increase of energy in front of the first wheelwell. This increase in total pressure acts on the first wheelwell and causes the increase of drag. Due to the side cover, the air has more difficulty entering the wheelhouse. As a result, air will remain trapped in front of the first wheelwell or flow out in other regions. An increase in outflow through the gap behind the bumper was observed, increasing the separation region and the bumper vortex. This is similar to the phenomenon discussed in the previous section. As a result, the lower wheel wake was more pronounced.

Furthermore, less outflow was observed in the first and third quadrant of the wheelhouse, as is shown in Table A.1. The wheelhouse side cover prevented air from entering the wheelhouse above Z/D > 0.5. The flow that enters the wheelhouse is distributed over the complete wheelhouse, reducing the massflows through the wheelhouse. It can be noted that the massflow leaving through the first quadrant is not directly affected by the side cover, but reduced nevertheless. Figure 5.37 shows that as a result of the lower massflow, the upper wheel wake width is decreased.

Furthermore, Figure 5.21 shows that the largest part of the drag savings were found at the trailer wheels. Although it was shown that the upper wheel wake is decreased, the increase in lower wheel wake dominates the flow field downstream. Figure 5.35 shows a region of lower energy flow on the outboard side of the body. The lower energy in the lower wheel wake propagates onto the trailer wheels, resulting in less drag on the trailer wheels.

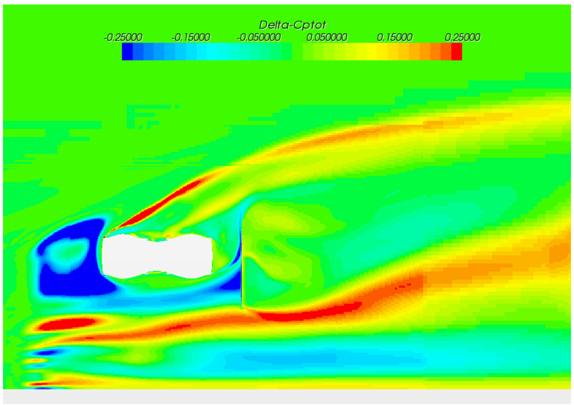

Figure 5.34: $C_{p,t,scw}$ - $C_{p,t,b}$, Z/D = .2

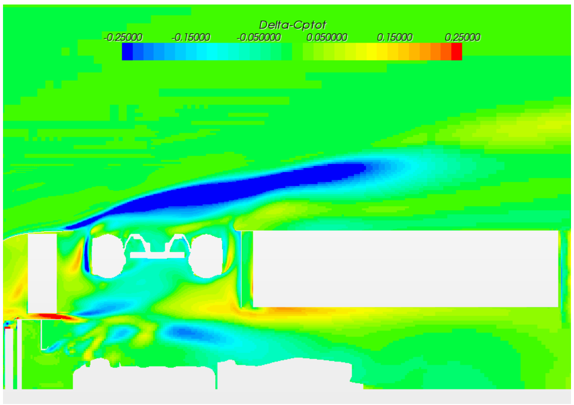

Figure 5.35: $C_{p,t,scw}$ - $C_{p,t,b}$, Z/D = .5

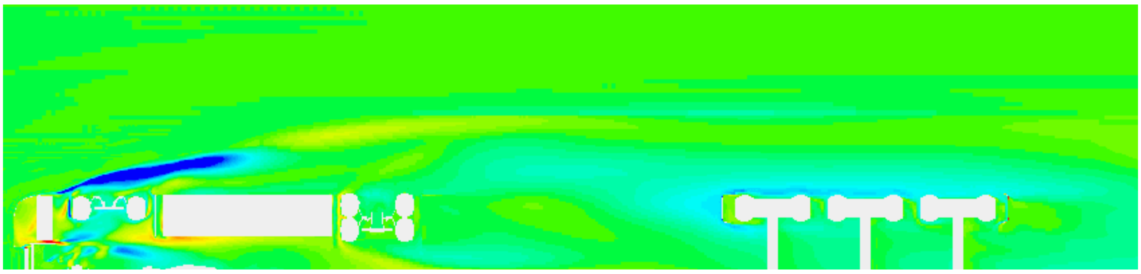

Figure 5.36: $C_{p,t,scw}$ - $C_{p,t,b}$, Z/D = .5

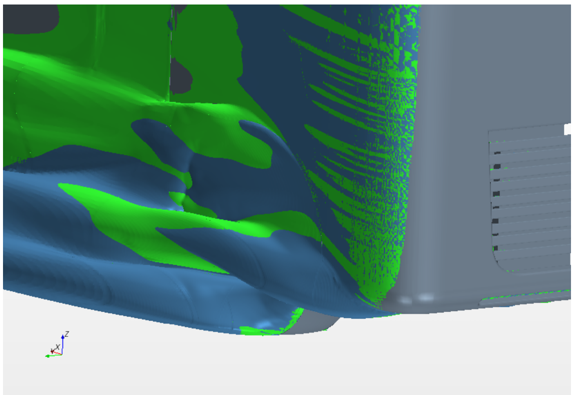

Figure 5.37: Side cover: isosurfaces of $p_{tot} = 0$

5.4.5 Underhood cap

This section presents the results of the underhood cap variant. In the baseline truck model it was seen that flow through the gap behind the bumper interferes with the flow through the underhood. It was thought that this interference was eliminated by extending the bumper further into the underhood.

Figures 5.38 and 5.39 present the difference in total pressure coefficient for the underhood cap variant. It shows that the underhood cap results in a significantly higher total pressure in the underhood. The flow through the gap behind the bumper is blocked, reducing the separation of the flow of the bumper. This results in an increase in momentum and massflow through the underhood.

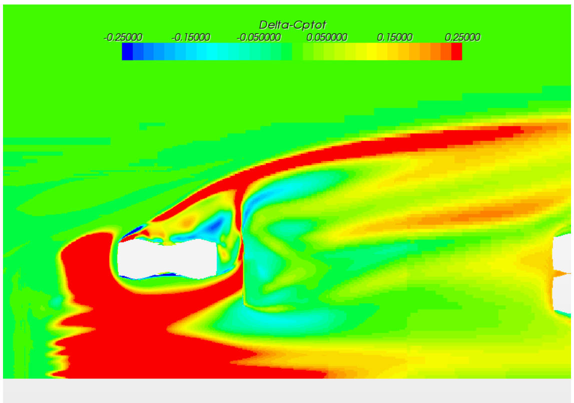

Figure 5.38: $C_{p,t,uhc}$ - $C_{p,t,b}$, Z/D = .2

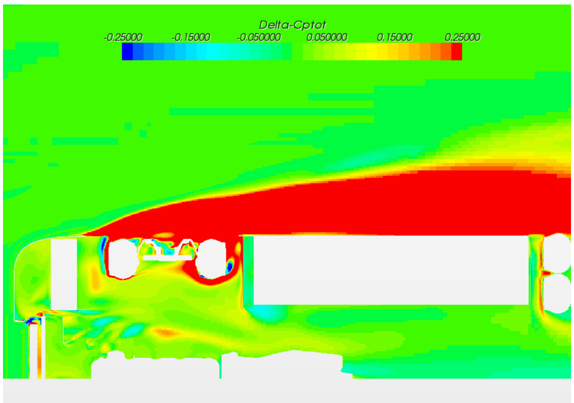

Figure 5.39: $C_{p,t,uhc}$ - $C_{p,t,b}$, Z/D = .5

The elimination of the separation of the bumper has a beneficial effect, as is shown in Figure 5.21. It is shown that along the edge of the bumper, the drag is decreased as a result of eliminating the separation. However, it also shows that the increase of momentum in the underhood has a detrimental effect on the drag of the wheelhouse. Figure 5.21 shows that the drag in the wheelhouse increases dramatically due to the higher total pressure in the wheelhouse. Furthermore, Figure 5.23 shows a significant increase in drag on the wheel due to the higher momentum flow stagnating on the wheel.

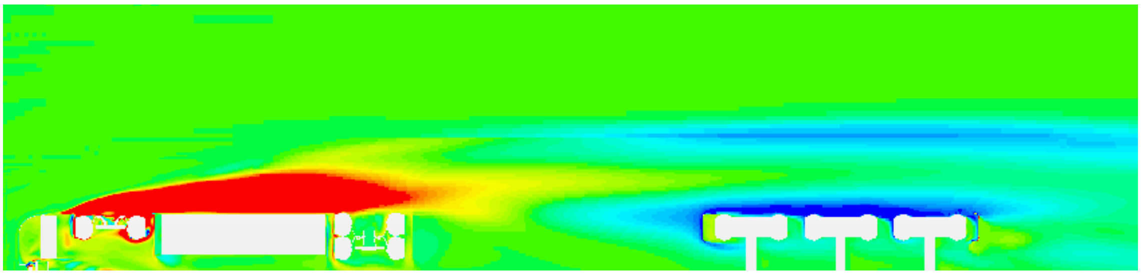

Figure 5.40: $C_{p,t,uhc}$ - $C_{p,t,b}$, Z/D = .5

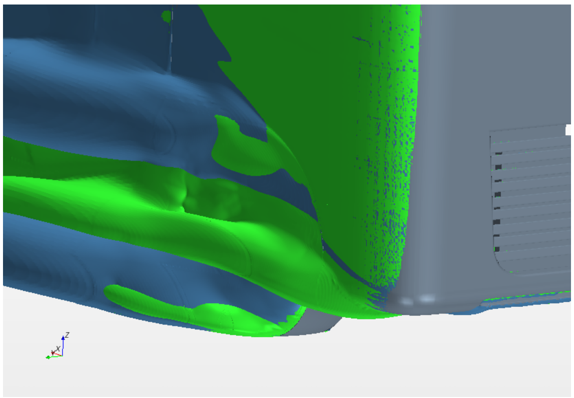

Figure 5.41: Underhood cap: isosurfaces of $p_{tot} = 0$

In the literature it was postulated that as a result of blocking the flow through the gap behind the bumper, the yaw angle of the flow was decreased (Söderblom et al., 2009). Indeed, it was observed that the flow angle in front of the wheel was decreased. Figure 5.41 shows that the width of the wake is decreased in the jetting region, due to the lower yaw angle. It was also seen that the outboard vortex was positioned further inboard and the inboard vortex grew stronger. However, the increased momentum through the underhood resulted in more separation further downstream. Figure 5.41 shows that the width of the wake is decreased in the jetting region and (approximately) $0.25 < Z/D < 0.75$. This is the position of the bumper vortex, which was eliminated completely. Figure 5.41 also shows that the upper wheel wake increases, although Table A.1 shows that there is no larger outflow. It appears that the vortex that comes from the bumper suppresses the formation of the wake for $Z/D > 0.75$. This region of lower energy propagates onto the trailer wheels and results in a significant decrease in drag on the trailer wheels.

5.4.6 Wheel spoiler, 45° angle

In Figures 5.42 and 5.43 present the difference in total pressure coefficient for the 45° spoiler in front of the wheel. It shows that the spoiler deflects the oncoming flow away from the wheel into the underhood and the freestream. The spoiler induced a large separation region, which was the reason for the increase in drag observed in Figure 5.21. Figure 5.45 presents the width of the wake compared to the baseline. It shows that the wheel spoiler results in a large increase of the width of the wake, caused by the air being deflected by the spoiler. It was observed that the wake at the top of the wheel is narrower. A beneficial effect of the wheel spoiler is that it decreases the energy and the massflow from the underhood into the wheelhouse. This results in a lower outflow of mass behind the wheel, as is shown in Table A.1.

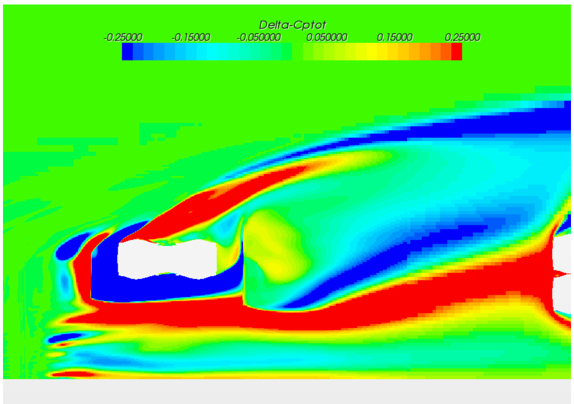

Figure 5.42: $C_{p,t,w45}$ - $C_{p,t,b}$, Z/D = .2

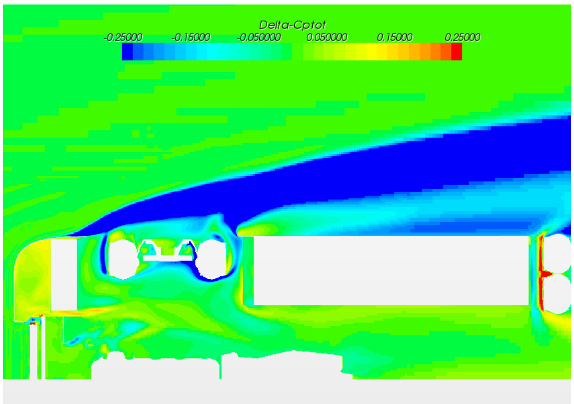

Figure 5.43: $C_{p,t,w45}$ - $C_{p,t,b}$, Z/D = .5

Figure 5.21 also shows that there is a significant decrease in drag on the trailer wheels. Figure 5.44 shows that the width of the wheel wake increases, resulting in a wake region hitting the mudguards.

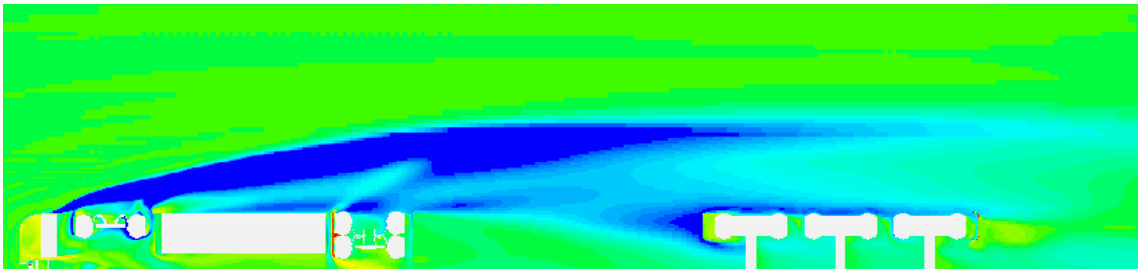

Figure 5.44: $C_{p,t,w45}$ - $C_{p,t,b}$, Z/D = .5

Furthermore, it is observed in Figure 5.42 that the wheel spoiler also deflects flow into the underhood. It shows that a large part of this deflected air flows past the mudguards and ends up impinging on the trailer wheels. In fact, Table 5.3 shows that there is a significant higher amount of energy in the underhood that reaches the rear tractor wheels. This jet of high energy is the cause of the increase of drag in the back tractor wheel region.

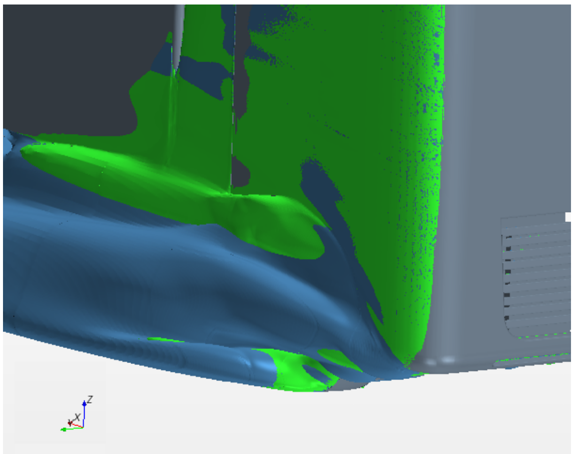

Figure 5.45: 45° spoiler: isosurfaces of $p_{tot} = 0$

5.4.7 Clearance gap

Finally, Figure 5.21 shows that reducing the clearance gap results in a different drag behaviour compared to all other variants. Where most variants resulted in a higher drag on the rear tractor and trailer wheels, this modification showed the opposite behaviour. Although it was seen that the drag coefficient of the simulation is not significantly different from the baseline, the behaviour of the drag difference is a reason for analysing the solution.

Figures 5.46 and 5.47 present the difference in total pressure coefficient. It can be seen that reducing the gap between the tyre and the body slightly increases the energy in the wheelhouse. Figure 5.22 shows a small increase in drag in front of the front wheel, but throughout the wheelhouse the drag was lower than in the baseline.

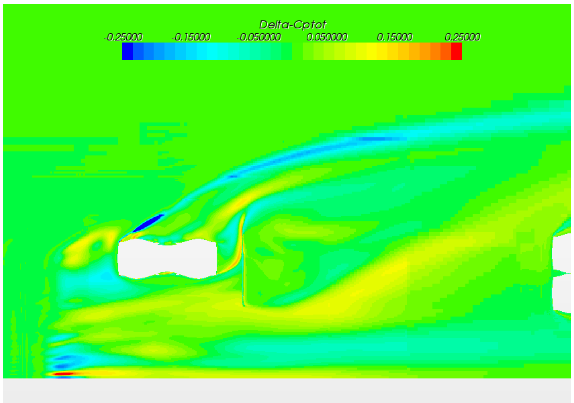

Figure 5.46: $C_{p,t,6cm}$ - $C_{p,t,b}$, Z/D = .2

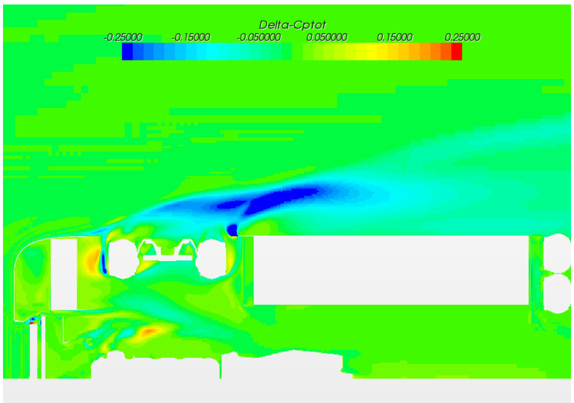

Figure 5.47: $C_{p,t,6cm}$ - $C_{p,t,b}$, Z/D = .5

Figure 5.47 also suggests that reducing the gap results in a lower energy in the lower wake, suggesting that the width is increased. It was observed that the massflow through the wheelhouse was decreased, but since the area was decreased velocities were higher. This resulted in an increase in the width of the lower wheel wake. Figure 5.49 indeed shows that the width of the wheel wake in the lower parts increased. More noticeably, it also shows that the upper wheel wake was decreased, mostly due to the reducing of the gap resulting in a cover for the top part of the wheelhouse. Figure 5.48 shows that the energy next to the wheelhouse propagates onto the trailer wheels. The increase in energy next to the wheelhouse was observed from locations Z/D > 0.7, but from Z/D > 0.85 the increase in energy reached the mudguard. Figure 5.21 shows that there is a slight increase in drag on the trailer wheels. This can be described to the higher energy flow on the side of the truck, and the increased energy past the rear wheels of the tractor.

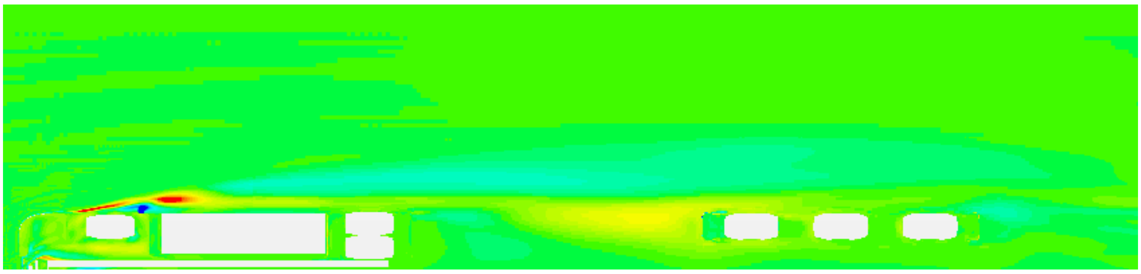

Figure 5.48: $C_{p,t,6cm}$ - $C_{p,t,b}$, Z/D = .85

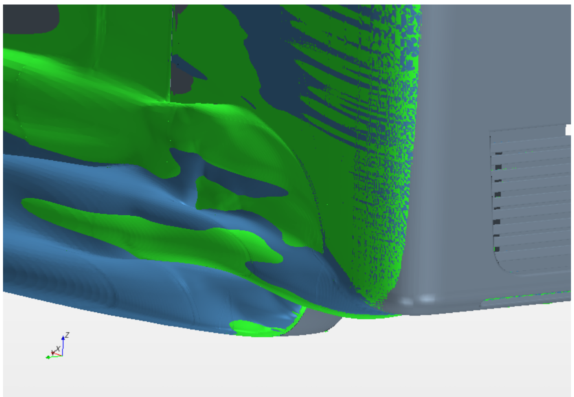

Figure 5.49: Clearance gap: isosurfaces of $p_{tot} = 0$

5.5 Comparison with literature

This section presents a comparison of some of the variants with the literature. Since there was no experimental data to validate the results of the simulations performed in this chapter, confirming with other research generates confidence in the model. This section presents an analysis and comparison of the following three variants:

- Experiments on a spoiler in front of the front wheel showed that the total pressure in the wheelhouse was reduced, reducing drag on the wheel with 35% (Dimitriou and Klussmann, 2006). The results were compared with the 45° wheel spoiler, presented in Section 5.4.6.
- Simulations on an extension of the bumper showed that total drag was increased by 2.4%, as a result of the higher pressure in the wheelhouse (Söderblom et al., 2009). The results were compared with the underhood cap variant, presented in Section 5.4.5.
- Simulations on ventilation of the wheelhouse showed a decrease in drag coefficient of 0.1% (Söderblom et al., 2009). The results were compared with the wheel ventilation variant, not presented in the previous sections.

5.5.1 Wheel spoilers

This section presents a comparison of the results obtained of the 45° wheel spoiler with experimental data (Dimitriou and Klussmann, 2006). The wheel spoiler used in the experiments was inserted in front of the front wheel of a passenger car, see Figure 5.50. It was postulated that adding a wheel spoiler resulted in a decrease of total pressure in the wheelhouse. Due to the lower total pressure, the drag of the wheel was decreased by 35%. In comparison, the simulations demonstrated that the energy in the wheelhouse was indeed decreased. As a result it was shown that the wheel spoiler reduced the drag with 100%, three times more than in the literature. It must be noted, however, that the wheel spoiler in the simulations was larger and created a larger separation region, explaining the higher decrease in drag of the wheel. The agreeing trend in the literature and simulations, does give confidence in the model though.

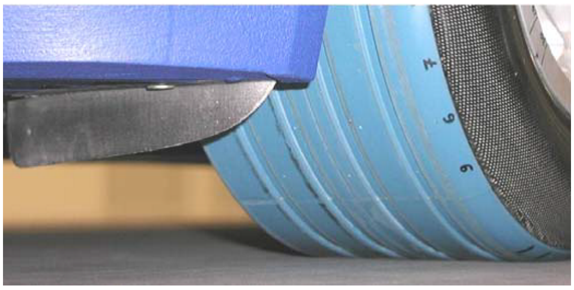

Figure 5.50: Wheel spoiler in front of wheel (Dimitriou and Klussmann, 2006)

The experimental study did not focus on the trend of the total drag of the passenger car (Dimitriou and Klussmann, 2006). It was seen however that the total drag in the simulations increased, mainly as a result of the large separation region created by the wheel spoiler. As a result of the wheel spoiler, flow was either injected into the freestream or underhood. It was concluded that an increase in width of the wake is not necessarily bad, since it can reduce drag on the rear trailer wheels. It was seen however, that the drag increase due to the wheel spoiler could not be overcome by the more favourable conditions. Observing that the wheel spoiler in the experimental study (Figure 5.50) deflected the flow in a more gentle manner demonstrates the wheel spoiler is a viable candidate to be further analysed.

5.5.2 Underhood cap

The principle of the underhood cap was to block the flow from behind the bumper gap to interfere with the flow through the underhood. It was thought that this would cause a more uniform flow through the underhood, resulting in a lower drag coefficient. This section presents a comparison of the underhood cap variant with the variant in the literature (Söderblom et al., 2009).

It was concluded in the literature that the higher momentum flow through the underhood increased the total pressure in the wheelhouse. This resulted in an increase in drag coefficient of 2.4%, which was mainly caused by the increase in total pressure acting on the wheelhouse and front wheels (Söderblom et al., 2009).

The simulations also showed an increase of momentum through the underhood, resulting in a local increase in drag, see Figure 5.21. However, the total drag coefficient showed a small decrease of 0.3 ± 0.15 %. It was seen that the increase in width of the higher wheel wake resulted in less drag on the trailer wheels.

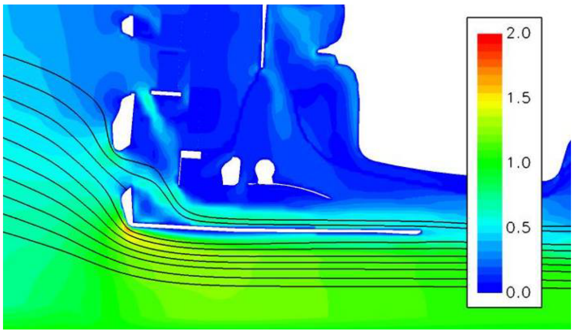

Figure 5.51: Normalised velocity magnitude for the underhood cap variant, from (Söderblom et al., 2009)

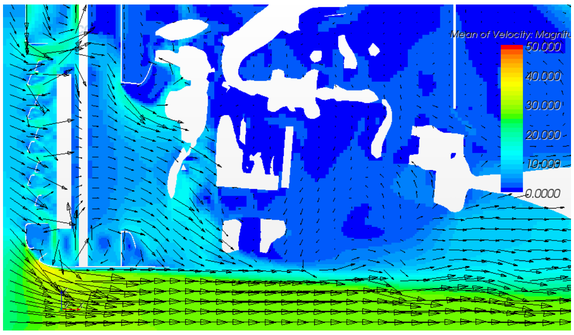

Figure 5.52: Normalised velocity magnitude for the underhood cap variant, simulation result

Figures 5.51 and 5.52 present the normalised velocity field around the underhood cap. There is a good agreement in the flow structure, where both variants show that the outflow through the gap behind the bumper is eliminated, resulting in attached flow in front of the front wheel.

It was postulated in the literature that the higher momentum flow resulted in a higher outflow through the top of the wheelhouse, increasing the width of the upper wheel wake (Söderblom et al., 2009). In the simulations the increase in upper wheel wake was also observed, although another reason was found for this increase. It was concluded that the wheel wake increased due to the absence of the separated vortex of the bumper. It was also demonstrated that the outflow through the top of the wheelhouse is significantly lower than in the baseline, see Table A.2, disagreeing with the observations in the literature.

Furthermore, in the report it was shown that the lower wheel wake decreased as a result of a lower yaw angle (Söderblom et al., 2009). Indeed, in the simulations it was also shown that the yaw angle was decreased in front of the wheel, but it did not result in a smaller wheel wake. Due to the significant increase in momentum through the underhood, it was seen that more separation occurred, increasing the width of the wheel wake. It was seen, though, that the jetting vortex was slightly suppressed by the more uniform flow in front of the front wheel.

5.5.3 Wheelhouse venting

The principle of the wheelhouse vent was to inject a part of the flow in the wheelhouse into the wake under more favourable conditions. In the literature it was concluded that the drag coefficient was decreased due to the relieve of pressure in the wheelhouse (Söderblom et al., 2009). Furthermore, it was shown that the vent allowed the flow to leave the wheelhouse under more favourable conditions, resulting in a decrease of wheel wake width.

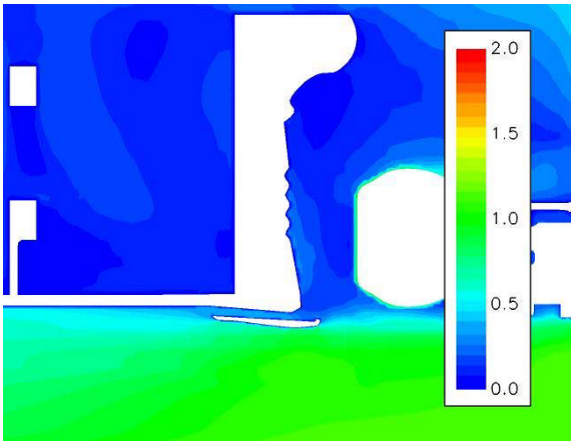

Figure 5.53: Normalised velocity magnitude for the wheelhouse ventilation variant, from (Söderblom et al., 2009)

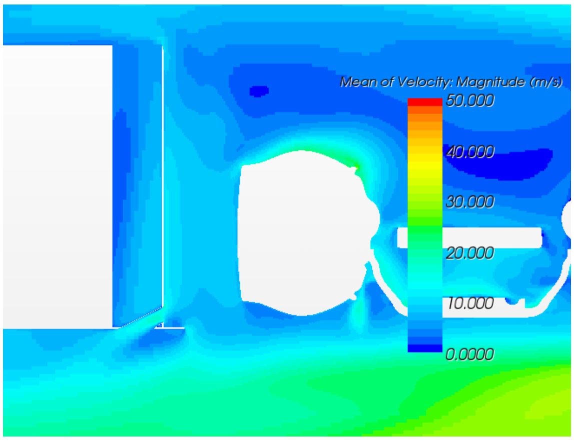

Figure 5.54: Normalised velocity magnitude for the wheelhouse ventilation variant, simulation result

Figures 5.53 and 5.54 present the flow fields of the two variants. It shows that the implementation of the vent is slightly different, but nevertheless differences can be observed. The implementation of the vent in Figure 5.54 is more in alignment with the angle of the flow in the wheelhouse and shows higher velocities in the vent. It can also be seen that the wake next to the wheel is much thicker in Figure 5.54 compared to Figure 5.53.

Nevertheless, in Figure 5.55 it is shown that the venting decreased the width of the wheel wake, which is in agreement with the observations in the literature. Figure 5.22 showed that a gradual decrease in drag can be observed throughout the wheelhouse. However, there was no major contribution from the rear wheel well, as was suggested in the literature (Söderblom et al., 2009).

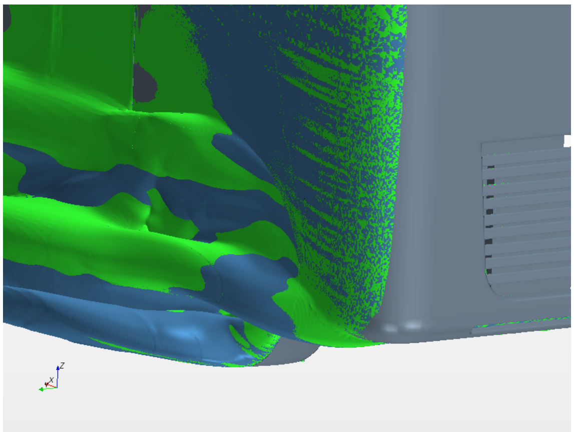

Figure 5.55: Wheelhouse ventilation: isosurfaces of $p_{tot} = 0$

5.6 Summary

This section presents the results of the simulations of the baseline model and the variants. The unsteady nature of the physics resulted in a fluctuation of the drag coefficient, even though a steady state solver was used. The standard error was used to accurately determine the mean of the variant, and thus whether a simulation was significantly different. It was found that it is difficult to focus the attention on the wheelhouse only, since the slightest changes had a (large) effect downstream. Furthermore, it was shown that the simulations that resulted in a decrease in drag coefficient did not show the same changes in velocity field, but displayed a different behaviour. The most important findings in this section were:

- Four simulations were found that had a significantly lower drag coefficient, and one simulation was found that had a significantly higher drag coefficient, than the baseline.
- It was found that only 35-40% of the massflow that enters the underhood reached the rear tyres and 30-35% left through the front wheelhouses. The other locations of massflow were not monitored, but a large massflow was observed between the front and rear tyres.
- The wheel wake was dominated by the separated regions of the front tyre, the bumper and the top of the wheelhouse. Apart from the vortex of the bumper, which was a new discovery, the positions agreed with the positions observed in the literature on a simplified model.
- It was found that the energy in the wheel wake was of great influence to the drag on the trailer wheels. Large increases in energy resulted in a higher drag, whereas the opposite was also observed. There was no relation between distribution of energy in the upper and lower wheel wake and the drag of the trailer wheels.
- Reducing the total pressure in the wheelhouse resulted in a lower drag coefficient, locally. The three simulations that reduced the total pressure inside of the wheelhouse all showed a local decrease in drag. The outflow conditions out of the wheelhouse had a large influence on the overall drag coefficient, however. The reverse is also true, a high momentum flow through the underhood and wheelhouse increased local drag dramatically.
- Three variants were compared with similar data the literature. Although there was some difference in the prediction of drag coefficient, the flow phenomena that were described showed similarities.
- The 45° spoiler and the wheelhouse ventilation did not result in the anticipated reduction in drag coefficient. Problem areas were identified, however, such that further simulations could result in a reduction of drag coefficient.

Chapter 6

Conclusions

CFD simulations on a heavy truck model were performed in order to visualise the flow structures in the front wheelhouses. A validation study was performed on a simplified wheelhouse model, since no experimental data was available for full-scale trucks. After a study on turbulence modelling and grid refinement a close agreement with experiments and reliable model settings were obtained. These model settings were applied to the baseline truck model. After the simulation of different variants, significant reductions in drag coefficient were found. The flow fields of the variants with a significant drag coefficient reduction were analysed in order to obtain an insight in the flow sensitivity to geometry changes. The following conclusions were obtained:

- It was found that unsteady RANS simulations did not result in a better prediction of the drag coefficient. The unsteady simulation computes the mean unsteady phenomena, but still relies on a turbulence model to predict the behaviour of the turbulent eddies. Furthermore, it was postulated that unsteady RANS was best suited when the unsteadiness is deterministic, which was not the case. The significant increase in computation time was therefore not justified.

- The baseline model showed several phenomena that resulted in an increase of the width of the wheel wake. The yawed flow through the underhood increased the separation of the shoulder of the tyre, creating a wider wake. Also the mudguards were found to disturb the formation of the wake and create a large jet of air into the freestream.

- The wheel wake was dominated by the separated regions of the front tyre, the bumper and the top of the wheelhouse.

- The analysis of massflow through the underhood showed that there is no relation between massflow and drag coefficient. It was shown that 30% of the flow entering the underhood left through the front wheelhouses and only 35% reached the rear tyres of the tractor.

- It was found that the conditions in the wheel wake had a large influence on the drag of the trailers and mudguards. Drag reduction on the trailer might therefore either be obtained by reducing the energy in the wheel wake or preventing the wheel wake from impinging on the trailer wheels.
- Reducing the total pressure in the wheelhouse resulted in a lower drag on the wheelhouse and front wheel. Conversely, it was observed that a higher total pressure in the wheelhouse resulted in a local increase in drag. It was seen however that the total drag of the truck was highly dependent on the conditions upstream and in the wake.
- Some of the results showed an increase in drag coefficient, but a promising behaviour of the flow field. Further simulations could result in a reduction of drag coefficient.
- A comparison with the literature was made, which verified that the results of the variants agreed with the (numerical) observations in the literature.

Chapter 7

Recommendations

- There are a lot of limitations to the modelling of the flow. If resources are available, the use of DES/LES simulations would be advised. It was seen that the half model approach is valid with a steady state solver, but this is not valid for a LES solver.
- It was demonstrated that the modelling of the contact patch is essential, but compromises were made in this thesis. It was discussed that it is difficult to obtain a correct representation of the tyre, since its shape changed continuously due to wear and rotational effects. Furthermore, it was seen that there are several effects due to the compression of the tyre (some of which are unexplored, even in the literature) and all of them have an effect on the flow. The impact of simplifying the representation of the contact patch was not quantified.
- There are different approaches to the modelling of the rotation of the wheel and it was observed in the literature that the effect on the flow field is significant. To get a better representation of the actual flow field more advanced methods in wheel rotation need to be explored.
- Features such as wheel axes, cabins steps and mirrors were not modelled, but it was expected that they have an effect on the flow. A second step would be to validate the findings in this study using a more realistic truck model and explore the influence of the omitted features.
- It was seen that the local changes have a large effect downstream, which issues the need for a better representation of the geometry of the trailer and trailer wheels.
- To validate the model and the results of the simulation, experimental data is needed.

Bibliography

N.E. Ahmad, E. Abo-Serie, and A. Gaylard. Mesh optimization for ground vehicle aerodynamics. *CFD Letters*, 2(1), 2009.

J. Axerio, G. Iaccarino, E. Issakhanian, K. Lo, C. Elkins, and J. Eaton. Computational and experimental investigation of the flow structure and vortex dynamics in the wake of a formula 1 tire. *SAE Technical Paper*, 2009.

J. Axerio-Cilies. *Predicting Formula 1 tire aerodynamics: sensitivities, uncertainties & optimization.* PhD thesis, Stanford, University, Mechanical Engineering Department, 2012.

J. Axerio-Cilies, E. Issakhanian, J. Jimenez, and G. Iaccarino. An aerodynamic investigation of an isolated stationary formula 1 wheel assembly. *Journal of Fluids Engineering*, 134(2), 2012.

L. Axon. *The Aerodynamic Characteristics of Automobile Wheels - CFD Prediction and Wind Tunnel Experiment.* PhD thesis, Cranfield University: College of Aeronautics, 1999.

A. Bakker. Applied computational fluid dynamics: Lecture 10 - turbulence models. *Dartmouth College / Fluent*, 2005.

P.W. Bearman, D. de Beer, E. Hamidy, and J.K. Harvey. The effect of a moving floor on wind-tunnel simulation of road vehicles. *SAE Technical Paper*, 1988.

CD-adapco. User guide, STAR-CCM+ v7.06. *Melville, NY, USA.*, 2013.

A. Cogotti. Aerodynamic characteristics of car wheels. In *Technological Advances in Vehicle Design Series, SP3; Impact of Aerodynamics on Vehicle Design*, pages 173–196. International Journal of Vehicle Design, 1983.

F. Damiani, Iaccarino G., G. Kalitzin, and B. Khalighi. Unsteady flow simulations of wheel-wheelhouse configurations. In 34^{th} *AIAA Fluid Dynamics Conference and Exhibit*, 2004.

I. Dimitriou and S. Klussmann. Aerodynamic forces of exposed and enclosed rotating wheels as an example of the synergy in the development of racing and passenger cars. *SAE International*, 2006.

B.D. Duncan, S. Kandasamy, K. Sbeih, T.H. Lounsberry, and M.E. Gleason. Further cfd studies for detailed tires using aerodynamics simulation with rolling road conditions. *SAE International*, 2010.

P. Elofsson and M. Bannister. Drag reduction mechanisms due to moving ground and wheel rotation in passenger cars. 2002.

F. Fabijanic. An experimental investigation of wheel-well flows. *SAE Technical Paper*, 1996.

J. E. Fackrell. *The Aerodynamics of an Isolated Wheel Rotating in Contact with the Ground.* PhD thesis, University of London, 1974.

T. Hobeika. *Investigation of Tyre Geometry Influence on Road Vehicle Aerodynamics.* PhD thesis, Department of Civil and Environmental Engineering, 2012.

A. Iaccarino, A. Ooi, P.A. Durbin, and M. Behnia. Reynolds averaged simulation of unsteady separated flow. *International Journal of Heat and Fluid Flow*, 2003.

J. Jeong and F. Hussain. On the identification of a vortex. *Journal of Fluid Mechanics*, 285, 1995.

R.D. Knowles. *Monoposto racecar wheel aerodynamics: investigation of near-wake structure and support-sting interference.* PhD thesis, Cranfield University, 2005.

S. Krajnović, S. Sarmast, and B. Basara. Numerical investigation of the flow around a simplified wheel in a wheelhouse. *Journal of Fluids Engineering*, 133(11), 2011.

O. Lögdberg. *Turbulent boundary layer separation and control.* PhD thesis, KTH Mechanics Stockholm, 2006.

S.P. Mavuri and S. Watkins. The influence of wheel-housing shape on vehicle aerodynamic performance. *International Journal of Vehicle Design*, 57:275–291, 2011.

J. McManus and X.G Zhang. A computational study of the flow around an isolated wheel in contact with the ground. *Journal of Fluids Engineering*, 128(3):520–530, 2006.

A. P. Mears, R. G. Dominy, and D. B. Sims-Williams. The air flow about an exposed racing wheel. *SAE International*, 2002.

A.P. Mears, S.C. Crossland, and R.G. Dominy. An investigation into the flow-field about an exposed racing wheel. *SAE International*, 2004a.

A.P. Mears, S.C. Crossland, and R.G. Dominy. Racing car wheel aerodynamics - comparisons between experimental and cfd derived flow-field data. *SAE International*, 2004b.

A. Morelli. Aerodynamic effects on an automobile wheel. *Technical Report Trans 47/69, MIRA*, 1969.

L.J. Oswald and A.L. Browne. The airflow field around an operating tire and its effect on tire power loss. *SAE Technical Paper*, 1981.

M. Peric and CD-adapco Ferguson, S. The advantage of polyhedral meshes. *Dynamics v24*, 2005.

T. Régert and T. Lajos. Description of flow field in the wheelhouses of cars. *International Journal of Heat and Fluid Flow*, 28(4):616 – 629, 2007.

K. Saddington, R. Knowles, and K. Knowles. Ground effect aerodynamics of race cars. *Applied Mechanics Review*, 2006.

S. Sebben and C. Landström. Prediction of aerodynamic drag for different rim designs using varied wheel modelling in cfd. In *Proceedings of* 8^{th} *FKFS Conference, Stuttgart*, 2011.

A. F. Skea, P.R. Bullen, and J. Qiao. Cfd simulations and experimental measurements of the flow over a rotating wheel in a wheel arch. *SAE International*, 2000.

D. Söderblom, L. Löfdahl, P. Elofsson, and L. Hjelm. Heavy vehicle wheel housing flows - a parametric study. *SAE International*, 2009.

D. Söderblom, P. Elofsson, L. Hjelm, and L. Löfdahl. Experimental and numerical investigation of wheel housing aerodynamics on heavy trucks. *Journal of Commercial Vehicles*, 5 (4):29–41, 2012.

A. Sprot, D. Minto, J.B. Sims-Williams, and R. Dominy. Aerodynamic investigation on the effect of varying through-hub flow on a formula one front wheel assembly. *SAE International*, pages 1026–1041, 2011.

A. Sprot, D. Sims-Williams, and R. Dominy. The aerodynamic characteristics of a fully deformable formula one wind tunnel tyre. *SAE International*, pages 1026–1041, 2012.

W. R. Stapleford and G. W. Carr. Aerodynamic characteristics of exposed rotating wheels. *Technical Report 1970/2, MIRA*, 1970.

E. Thivolle-Cazat and P. Gilliéron. Flow analysis around a rotating wheel. In 13^{th} *International Symposium on Applications of Laser Techniques to Fluid Mechanics*, pages 61–66, 2006.

A. Wäschle. The influence of rotating wheels on vehicle aerodynamics - numerical and experimental investigations. *SAE International Technical Paper*, 2007.

A. Wäschle, S. Cyr, T. Kuthada, and J. Wiedemann. Flow around an isolated wheel - experimental and numerical comparison of two cfd codes. *SAE International Technical Paper*, 2004.

F. M. White. Viscous fluid flow. *McGraw-Hill Series in Mechanical Engineering*, 2006.

Appendix A

Results of massflow monitors

Table A.1: Massflows (%) through the massflow planes defined in Figures 5.24 and 5.25

	Inlet underhood			Front wheels		End of cabin		Back wheels	Trailer	Wheelhouse				C_D
	x_1	x_8	x_9	x_2	x_6	x_3	x_7	x_4	x_5	y_1	y_2	y_3	y_4	
6CM	7.6506	4.1506	0.2808	5.8284	3.4547	0.4209	7.4155	4.3834	7.7802	0.0711	2.6587	0.9945	0.4635	0.3651
UHC	9.0246	3.9874	-0.0078	6.184	4.431	1.0851	7.9991	5.0153	7.8394	0.3293	2.1333	0.8485	0.4895	0.3636
WCR	7.6619	4.0682	0.2747	5.8864	3.4989	0.6443	7.7116	4.744	8.5461	0.5556	2.8042	0.0806	0.0216	0.3422
S45	7.5023	4.1271	0.266	5.6967	3.2408	0.2814	7.2723	5.0736	6.4313	0.182	2.531	0.8835	0.6461	0.3694
SCW	7.6053	4.0475	0.2285	5.9527	2.8035	0.6003	7.0096	4.4614	7.1001	-0.0001	2.6664	0.744	0.8197	0.3577
B	7.6858	4.1915	0.2714	5.8536	3.3701	0.3256	7.3915	4.6102	8.064	0.0789	2.5905	1.0167	0.5972	0.3647

Table A.2: Massflows (kg/s) through the massflow planes defined in Figures 5.24 and 5.25

	Inlet underhood			Front wheels		End of cabin		Back wheels	Trailer	Wheelhouse				C_D
	x_1	x_8	x_9	x_2	x_6	x_3	x_7	x_4	x_5	y_1	y_2	y_3	y_4	
6CM	99.54	99.02	103.48	99.57	102.51	129.29	100.32	95.08	96.48	90.18	102.63	97.82	77.61	100.10
UHC	117.42	95.13	-2.87	105.64	131.48	333.28	108.22	108.79	97.21	417.51	82.35	83.46	81.96	99.69
WCR	99.69	97.06	101.21	100.56	103.82	197.88	104.33	102.9	105.98	704.6	108.25	7.93	3.62	93.81
S45	97.61	98.46	98.03	97.32	96.16	86.44	98.39	110.05	79.75	230.85	97.7	86.9	108.19	101.27
SCW	98.95	96.56	84.22	101.69	83.19	184.38	94.83	96.77	88.05	-0.07	102.93	73.17	137.26	98.07
B	100	100	100	100	100	100	100	100	100	100	100	100	100	100

Appendix B

Supplemantary figures

Validation: isosurfaces of Q and total pressure

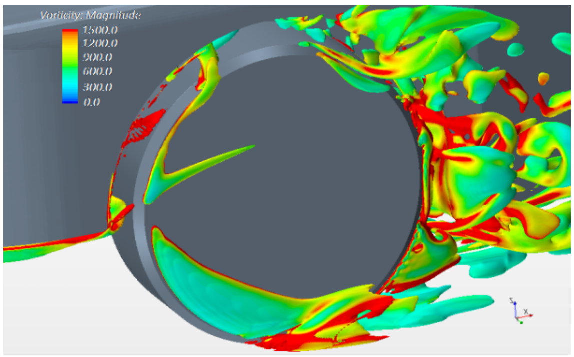
Vorticity: Magnitude
1500.0
1200.0
900.0
600.0
300.0
0.0

Figure B.1: Isosurface of QD/U_∞ = 50000, $k-\omega$ SST_1 turbulence model

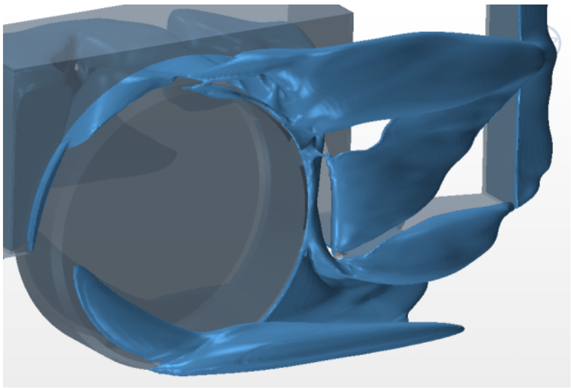

Figure B.2: Isosurface of $p_{tot} = 0$, $k-\omega$ SST_1 turbulence model

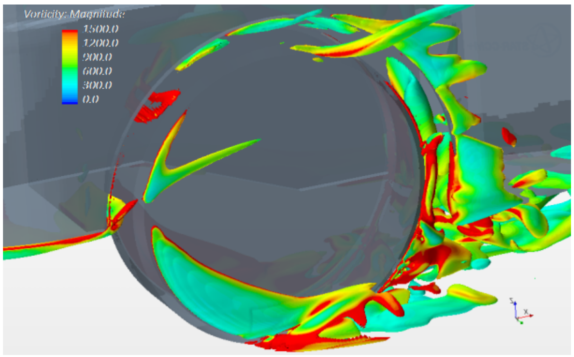
Vorticity: Magnitude
1500.0
1200.0
900.0
600.0
300.0
0.0

Figure B.3: Isosurface of QD/U_∞ = 50000, $k-\omega$ SST_1 turbulence model, restructured

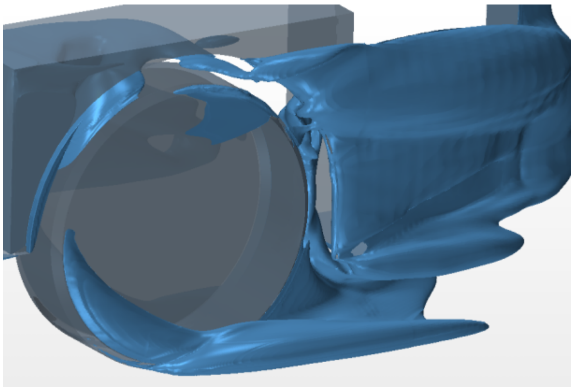

Figure B.4: Isosurface of $p_{tot} = 0$, $k-\omega$ SST_1 turbulence model, restructured

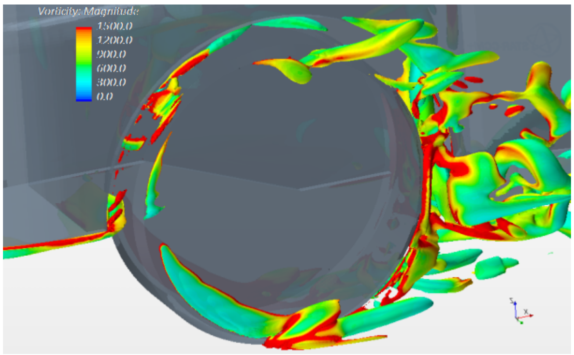
Vorticity: Magnitude
1500.0
1200.0
900.0
600.0
300.0
0.0

Figure B.5: Isosurface of QD/U_∞ = 50000, $k-\omega$ SST_{30} turbulence model

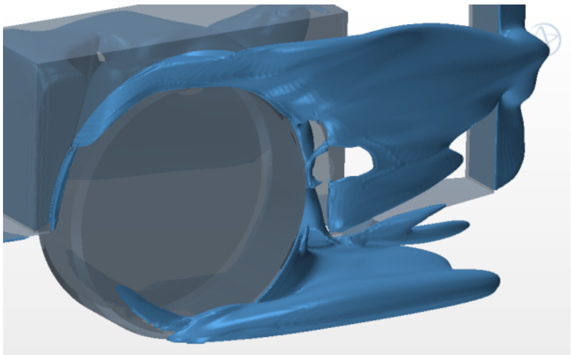

Figure B.6: Isosurface of $p_{tot} = 0$, $k-\omega$ SST_{30} turbulence model

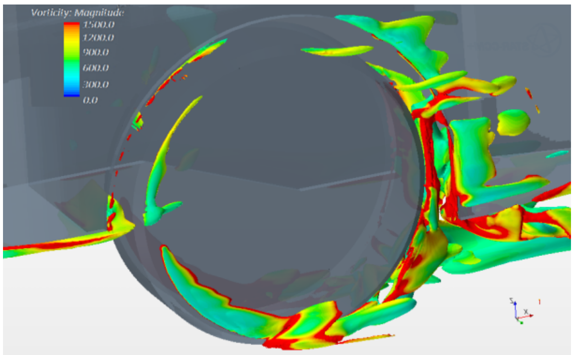
Vorticity: Magnitude
1500.0
1200.0
900.0
600.0
300.0
0.0

Figure B.7: Isosurface of QD/U_∞ = 50000, $k-\omega$ turbulence model

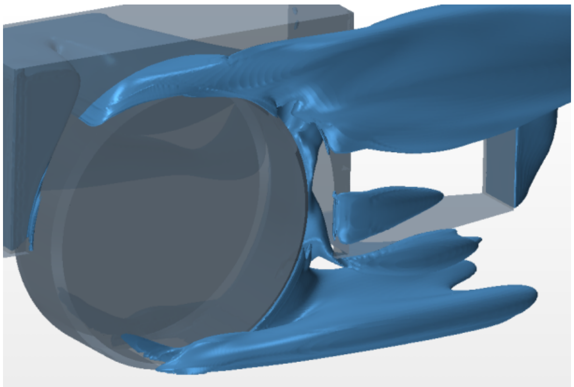

Figure B.8: Isosurface of $p_{tot} = 0$, $k-\omega$ turbulence model

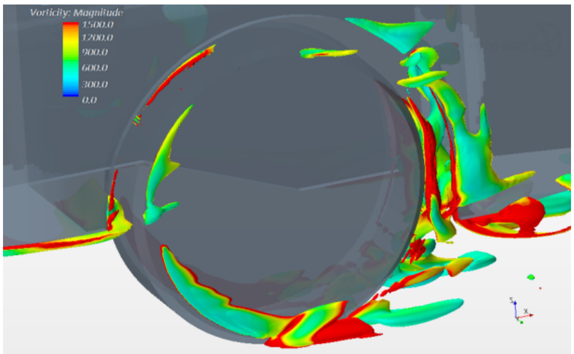
Vorticity: Magnitude
1500.0
1200.0
900.0
600.0
300.0
0.0

Figure B.9: Isosurface of QD/U_∞ = 50000, $k-\omega$ turbulence model, restructured

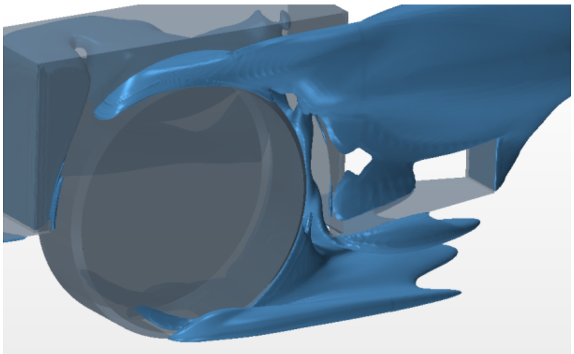

Figure B.10: Isosurface of $p_{tot} = 0$, $k - \omega$ turbulence model, restructured

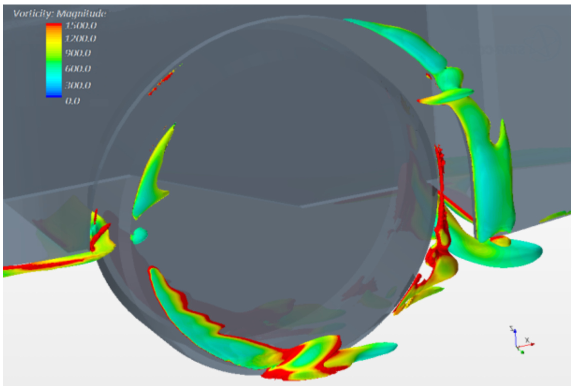
Vorticity: Magnitude
1500.0
1200.0
900.0
600.0
300.0
0.0

Figure B.11: Isosurface of QD/U_∞ = 50000, $k - \epsilon$ turbulence model

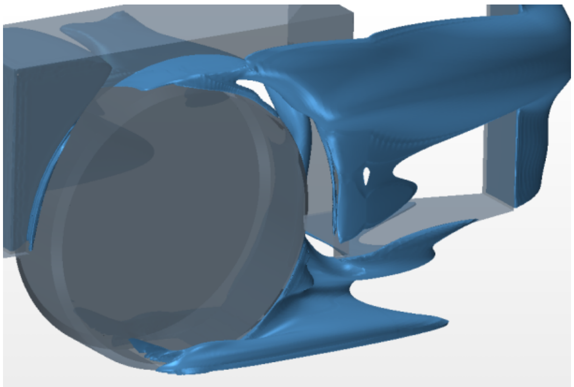

Figure B.12: Isosurface of $p_{tot} = 0$, $k - \epsilon$ turbulence model

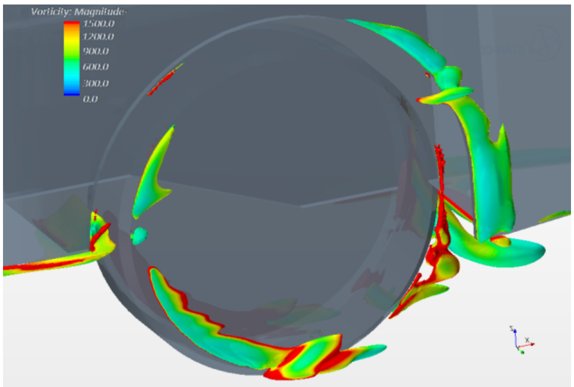
Vorticity: Magnitude
1500.0
1200.0
900.0
600.0
300.0
0.0

Figure B.13: Isosurface of QD/U_∞ = 50000, $k-\epsilon$ turbulence model, restructured

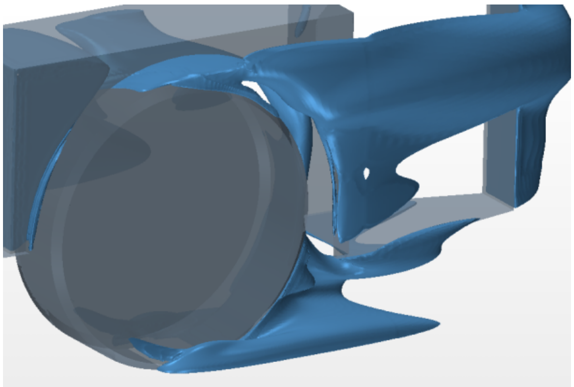

Figure B.14: Isosurface of $p_{tot} = 0$, $k - \epsilon$ turbulence model, restructured

Validation: wheelhouse pressure coefficient

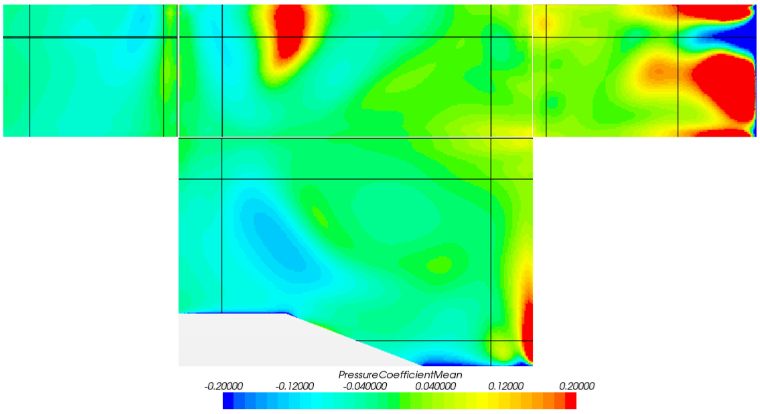

Figure B.15: Pressure coefficient distribution, $k-\omega$, mesh M8

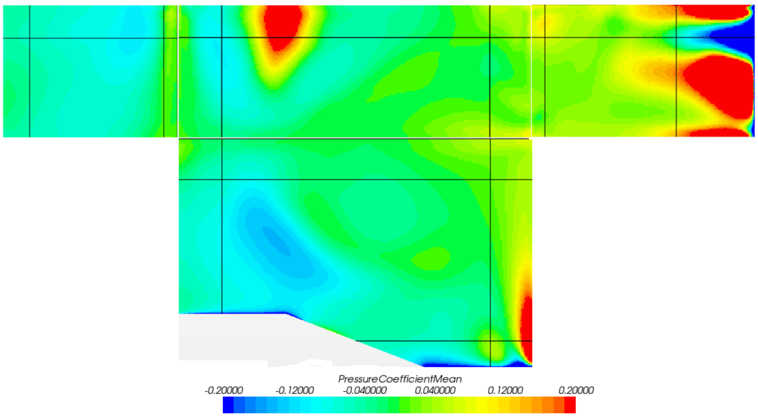

Figure B.16: Pressure coefficient distribution, $k-\omega$, mesh OPT

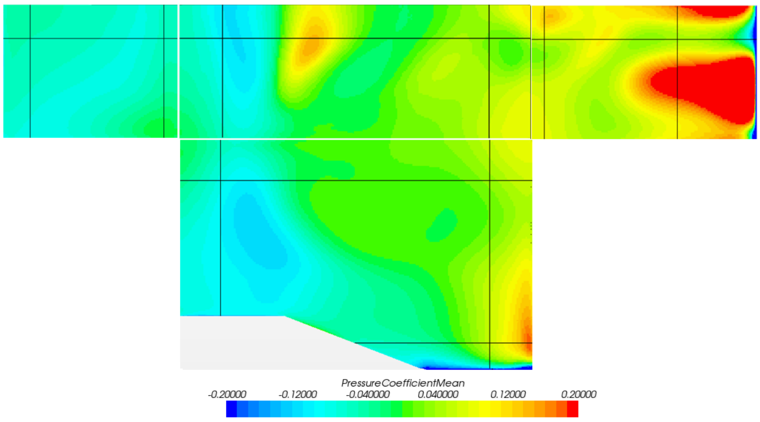

Figure B.17: Pressure coefficient distribution, $k-\omega$, mesh M8

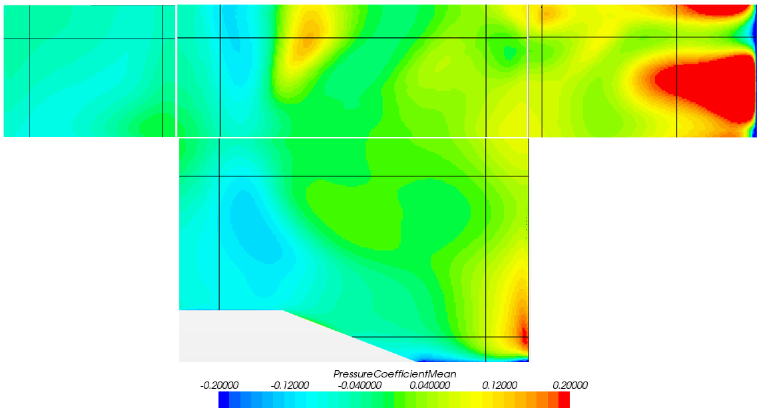

Figure B.18: Pressure coefficient distribution, $k - \epsilon$, mesh OPT

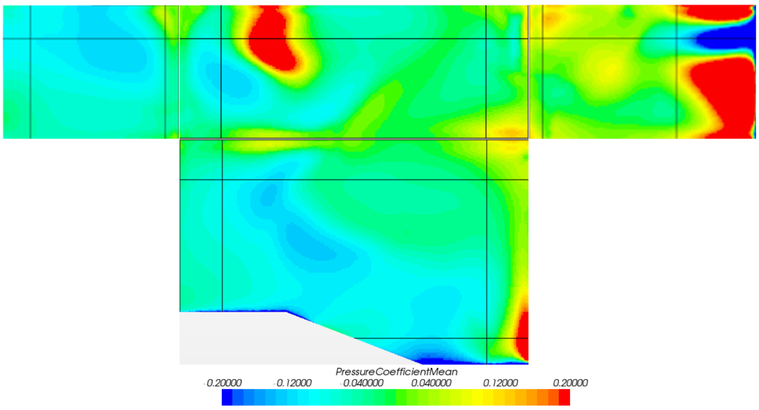

Figure B.19: Pressure coefficient distribution, $k - \omega\ SST_30$, mesh M8

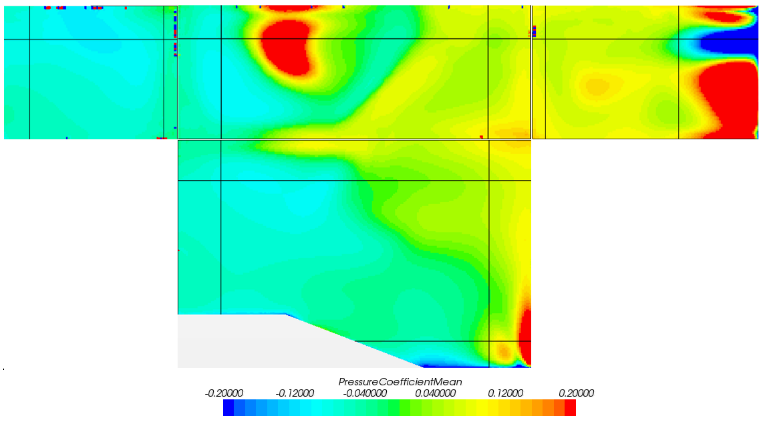

Figure B.20: Pressure coefficient distribution, $k - \omega\ SST_1$, mesh OPT

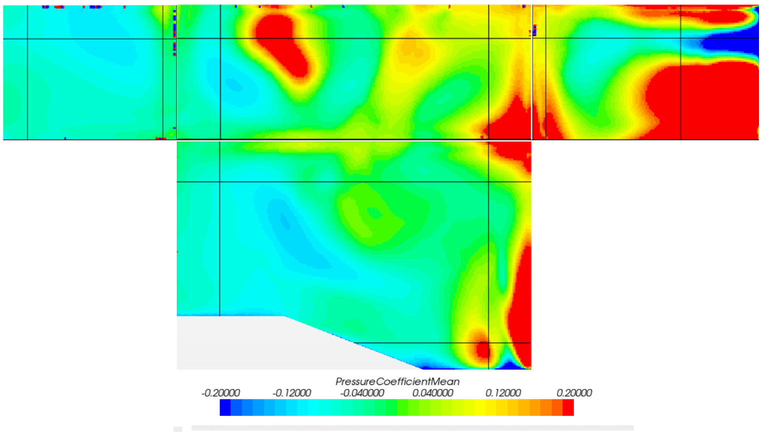

Figure B.21: Pressure coefficient distribution, $k-\omega\ SST_1$, mesh M8

Results: differences in velocity magnitude

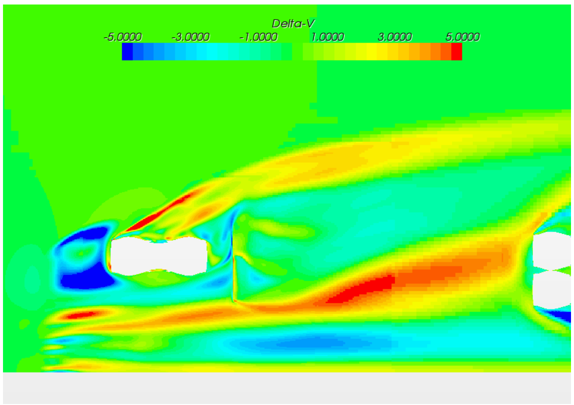

Figure B.22: $V_{mag,scw}$ - $V_{mag,b}$, Z/D = .2

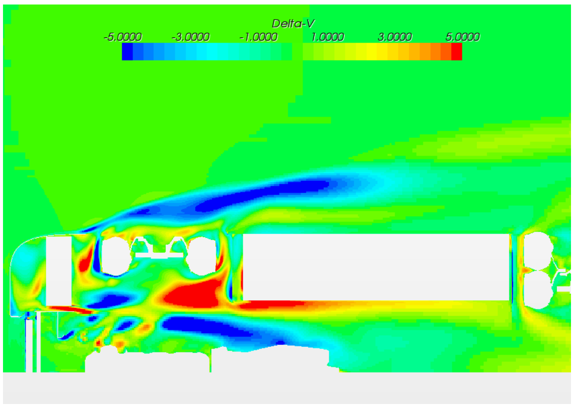

Figure B.23: $V_{mag,scw}$ - $V_{mag,b}$, Z/D = .5

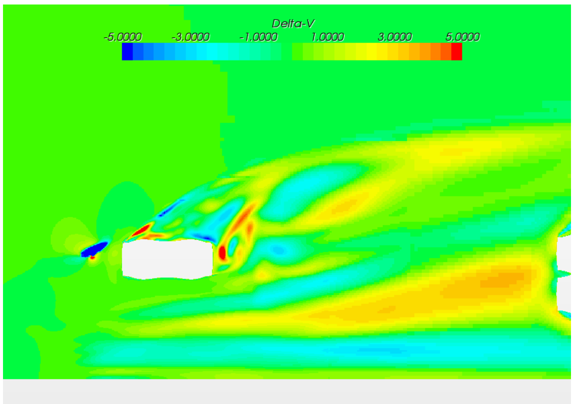

Figure B.24: $V_{mag,ts}$ - $V_{mag,b}$, Z/D = .2

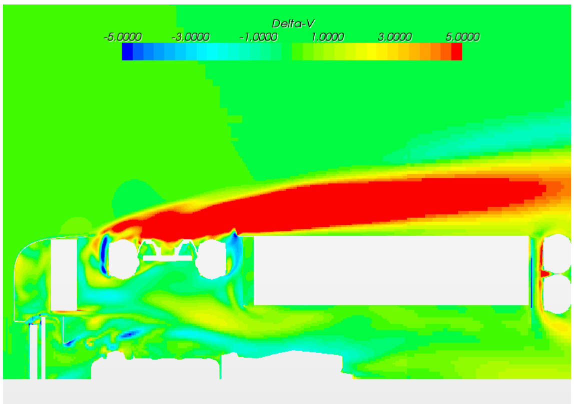

Figure B.25: $V_{mag,ts}$ - $V_{mag,b}$, Z/D = .5

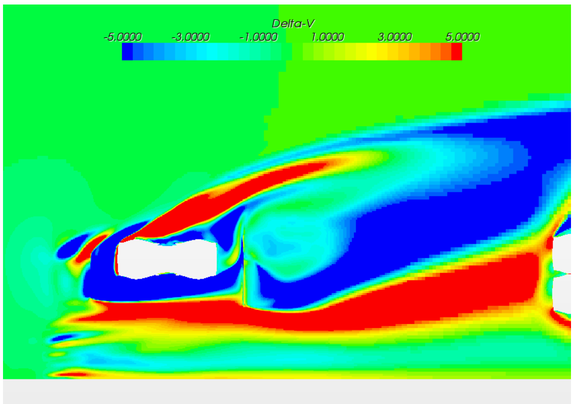

Figure B.26: $V_{mag,w45}$ - $V_{mag,b}$, Z/D = .2

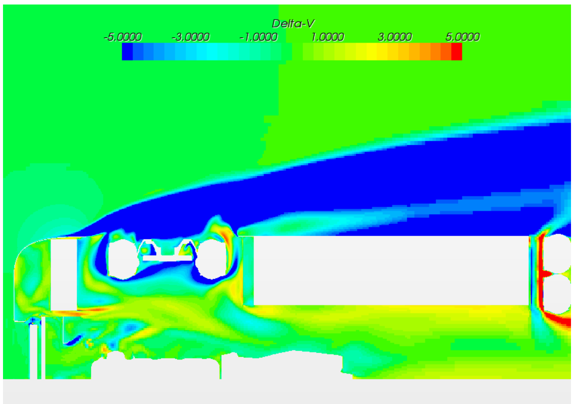

Figure B.27: $V_{mag,w45}$ - $V_{mag,b}$, Z/D = .5

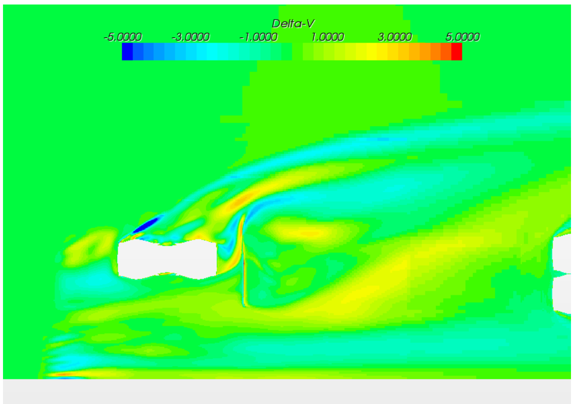

Figure B.28: $V_{mag,6cm}$ - $V_{mag,b}$, Z/D = .2

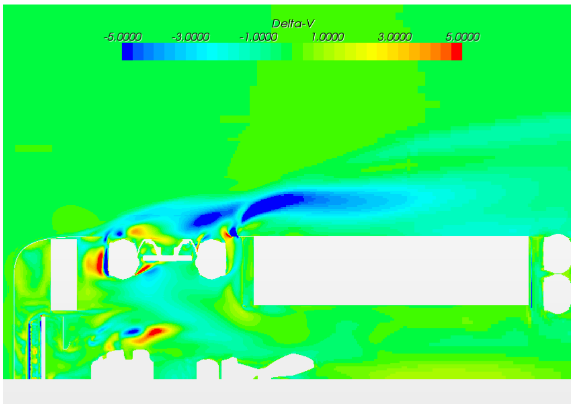

Figure B.29: $V_{mag,6cm}$ - $V_{mag,b}$, Z/D = .5